TRANSPORT OF SOLID PARTICLES IN DETERMINISTIC LATERAL DISPLACEMENT SYSTEMS

by

SIQI DU

A dissertation submitted to the

School of Graduate Studies

Rutgers, The State University of New Jersey

In partial fulfillment of the requirements

For the degree of

Doctor of Philosophy

Graduate Program in Mechanical and Aerospace Engineering

Written under the direction of

German Drazer

And approved by

_____

_____

_____

_____

New Brunswick, New Jersey

OCTOBER 2018

ABSTRACT OF THE DISSERTATION

TRANSPORT OF SOLID PARTICLES IN DETERMINISTIC LATERAL DISPLACEMENT SYSTEMS

by SIQI DU

Dissertation Director:

German Drazer

In this dissertation, we propose various modifications on the well-known separation scheme in microfluidics that is deterministic lateral displacement (DLD), and discuss the potential of using one of our more radically modified DLD systems in the filtration of particulate matter air pollution.

We first introduce the design specifics of the DLD systems that are prevalently used in separation-related microfluidic research, including two different geometries. We also present two popular models that describe DLD systems, referred to as streamline-based model and collision-based model (proposed by our group) to provide a theoretical framework for DLD.

We then use a macromodel of a flow-driven deterministic lateral displacement (DLD) microfluidic system to investigate conditions leading to size-separation of suspended

particles. This model system can be easily reconfigured to establish an arbitrary orientation between the average flow field and the array of obstacles comprising the stationary phase (forcing angle). We also investigate the effect of obstacle size using two arrays with different obstacles but same surface-to-surface distance between them. In all cases, we observe the presence of a locked mode at small forcing angles, in which particles move along a principal direction in the lattice until a locked-to-zigzag transition takes place when the orientation of driving force reaches a critical angle. We show that the transition occurs at increasing angles for larger particles, thus enabling particle separation at specific forcing angles. Moreover, we observe a linear correlation between the critical angle and the size of the particles that could be used in the design of microfluidic systems with a fixed orientation of the flow field. Finally, we show that the collision-based model accurately describes the observed dependence of the migration angle on the orientation of the average flow.

We present a simple modification to enhance the separation ability of deterministic lateral displacement (DLD) systems by expanding the two-dimensional nature of these devices and driving the particles into size-dependent, fully three-dimensional trajectories. Specifically, we drive the particles through an array of long cylindrical posts, such that they not only move parallel to the basal plane of the posts as in traditional two-dimensional DLD systems (*in-plane* motion), but also along the axial direction of the solid posts (*out-of-plane* motion). We show that the (projected) in-plane motion of the particles is completely analogous to that observed in 2D-DLD systems. In fact, the collision-based model, which was originally developed for force-driven, two-dimensional DLD systems accurately describes the experimental results. More importantly, we analyze the particles

out-of-plane motion and observe significant differences in the out-of-plane displacement depending on particle size for certain orientations of the driving force. Therefore, taking advantage of both the in-plane and out-of-plane motion of the particles, it is possible to achieve the simultaneous fractionation of a polydisperse suspension into multiple streams.

In traditional DLD, a periodic array of solid posts induces the separative migration of suspended particles moving through the system. Here, we present a radical departure from traditional systems and use an array of anchored liquid-bridges as the stationary phase in the DLD device. The liquid-bridges are created between two parallel plates and are anchored to the bottom one by cylindrical wells. We show that the non-linear particle dynamics observed in traditional DLD systems is also present in the anchored-liquid case, enabling analogous size-based separation of suspended particles. The use of liquid-bridges as stationary phase presents additional possibilities in separation technologies, potentially eliminating or significantly reducing clogging, enabling renewable and/or reconfigurable stationary phases, allowing a different set of fabrication methods and providing alternative ways to separate particles based on the interaction of the particles with liquid-liquid interfaces.

We then explore the potential to filter particulate matter filtration using an array of water bridges. We conduct preliminary experiments based on the particle capturing ability of a single water bridge. We find that the efficiency of particle capturing for a single water bridge is determined by two important factors, which are incoming offset and Stokes number of the incoming particles. The incoming offset is the distance between the initial particle trajectory and the centerline of the water bridge and the particle Stokes number characterizes its tendency of following the streamline. We find that, in general, the smaller

the incoming offset is, meaning particles entering the collision closer to the centerline of the bridge, the more likely it is for particles to get captured. Also, higher Stokes numbers, meaning that particle trajectory deviates from the streamline to a larger degree, will result in a higher capture efficiency as well. Although more research effort is needed to better comprehend the various aspects of the proposed air filtration system, our preliminary exploration yields very promising results.

Acknowledgement

The last five years without a doubt has seen the most growth from me both as a scientific researcher and as a person in general. When I started college, I could never even imagine that Dr. will one day prefix my name. Yet here I am, nine years later, writing the acknowledgement section for my doctoral dissertation filled with immense joy and pride for having accomplished such a feat.

Looking back, I would first and foremost thank my adviser, Prof. German Drazer, for his never ending patience with me, the valuable lesson he taught me not only on research but on life in general, and his wining sense of humor. I am eternally grateful for his understanding and advice when I was struggling to balance course work and research during my first year abroad as a Ph.D. student. One interesting fact about our lab is that all the Ph.D. students in the group are working on projects that fall in completely different disciplines. Prof. Drazer impressively has always been able to stay on top of our progress and to provide us with insightful advice and helpful guidance along the way. He has inspired me though example to be curious about everything and to believe in my ability to

learn and absorb new knowledge, and I will undoubted cherish and practice it for the rest of my life. I also like to thank Prof. Drazer for always keeping it light and in good fun in our weekly meetings especially during periods when I am under tremendous stress. And most of all, for understanding the hardships of being an international student in a foreign country and for always trying his best to provide us with everything we need to achieve our goals in life.

I wish to thank Dr. Shahab Shojaei-Zadeh for all the advice and discussions during our joint group meetings, and for collaborating with us on the Liquid DLD project. And I also wish to thank Dr. Hao Lin for his guidance and passion for the air filtration project, Dr. Steven D. Tse for allowing us to use the state-of-the-art equipment in his lab.

I also want to express my immense gratitude towards my incredible colleagues, also some of my best friends, that I cannot possibly name all, Ms. Tianya Yin, Ms. Minglu Li, Mr. David Cunningham, Mr. Yanjun Wang and Mr. Robert Weir etc. for their endless support during the past few years. Their friendship has been a valuable anchor for me during the ups and downs in my Ph.D. years. All those late nights analyzing data or writing manuscripts together, all your insights during countless technical discussions, and all your words of encouragement when I most needed them are what helped keep me grounded and happy during a not particularly easy five years of my life.

One person I would also like to mention is my first mentor, alumni of our lab, Dr. Raghavendra Devendra. He warmly welcomed me when I first came to Prof. Drazer's lab as an undergraduate researcher 7 years ago. And it is his remarkable patience, valuable guidance and his wonderful passion for research that have inspired me to become a researcher myself.

Finally I would like to thank Prof. Hao Lin, Prof. Gerardo Callegari, and Prof. Mehdi Javanmard for devoting time to provide valuable comments on my doctoral dissertation and serving as the thesis committee.

I also would like to acknowledge that three chapters in this dissertation have been adapted from my previous publications with Prof. Drazer. Specifically, Chapter 3 is adapted from our publication in *Journal of Micromechanics and Microengineering* published in 2015, titled "Deterministic separation of suspended particles in a reconfigurable obstacle array".[1] Chapter 4 is adapted from our publication in *Scientific Reports* published in 2016, titled "Gravity driven deterministic lateral displacement for suspended particles in a 3D obstacle array".[2] And chapter 5 is adapted from our publication in *Soft Matter* published in 2017, titled "Liquid-based stationary phase for deterministic lateral displacement separation in microfluidics".[3]

Dedication

To the incredible women in my family, who shower me with unconditional love every single day and are also the hardest worker I've ever seen, my mother 魏凤英 (Mrs. Fengying Wei) and my aunt 魏秀英 (Mrs. Xiuying Wei).

Table of Contents

List of Tables

List of illustrations

1 Introduction

1.1 Micro total analysis systems (μ-TAS)

Microfluidics is the science and technology of systems that process or manipulate small amounts of fluids (10^{-9} to 10^{-8} liters), using channels with dimensions between tens and hundreds of micrometers.[4] Micro total analysis systems (μ-TAS) or Lab-on-a-chip (LOC) is a concept in microfluidics that describes the integration of an entire analytical process from sample preparation through reaction and separation to detection onto a single chip. Figure 1.1 presents a miniaturized chemostat that is a perfect demonstration of the concept.[5] Due to the ability to achieve high sensitivity and high resolution analysis of small volume samples, μ-TAS has been serving as the ultimate premise for microfluidic research ever since its introduction. To facilitate the realization of highly integrated micro systems that are capable of performing complete, automated analysis on a given biological or chemical

sample, there has been considerable effort invested in all areas in the field of microfluidics. For microtechnology advances, significant progresses has been made in aspects of design,[6,7] new materials,[8–12] bonding processes,[13–18] surface modifications,[19–30] channel layout/patterning and molding[31–34] and microscale 3D printing.[35–37] There has also been major advancement for functional units used in standard operations such as flow control,[38–52] sample separation,[53–59] and detection.[60–72] In terms of real life applications, μ-TAS has branched out into areas including drug screening and drug discovery,[73,74] disease diagnosis,[51,75,76] nucleic acid analysis,[8,77–85] protein analysis,[86–88] cell analysis[89–98] and environmental health and safety, food, and water analysis,[99–104]

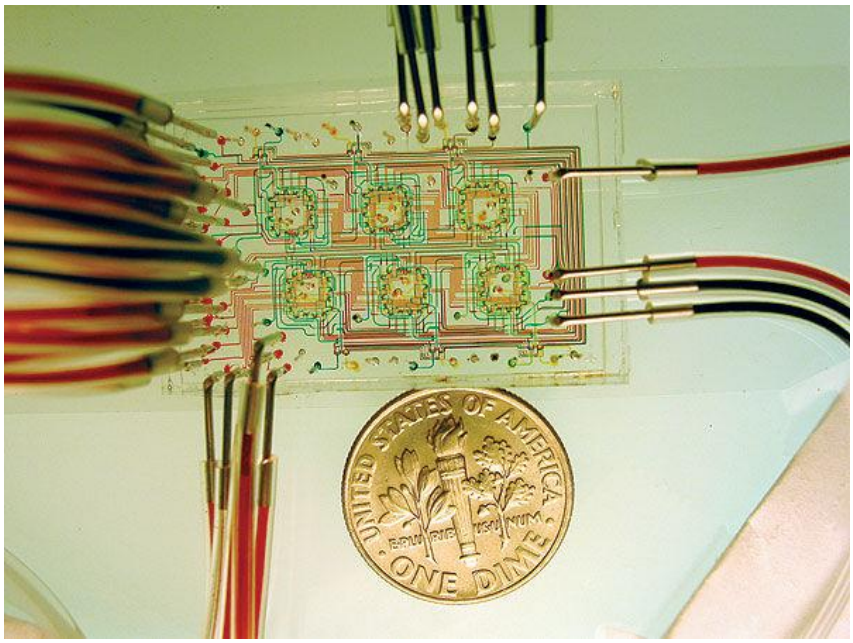

Figure 1.1A microfluidic chemostat that enables long-term culture and monitoring of extremely small populations of bacteria with single-cell resolution. Different fruit colors have been applied to differentiate different flow channels. To serve as a reference, the coin is 18 mm in diameter. Reproduced from Balagadd é *et al.*, 2005.[5]

Throughout the years, however, most of the work has focused on proposing novel individual components for those systems in a “divide and conquer” fashion. Only until recently, the devices with integrated functional units that can actually perform partially automated or fully automated chemical analyses have dominated the field of microfluidic research. Within the scope of highly integrated microfluidic systems, new concepts such as digital microfluidics (DMF),[88,105–109] which involves discretely manipulating picoliter- to microliter- sized droplets in integrated microfluidic systems, and point of care (POC) devices,[110–116] have emerged and rapidly grown, continuing the pursuit for highly integrated microfluidic systems.

1.2 Separation Units

Separation is one the most important procedures in biological/chemical sample analysis, and as a result, microfluidic separation units that fractionate mixtures into individual chemical or biological components constitute an integral part of μ-TAS. These methods can be broadly classified as *active* or *passive* depending on the use or not of an external field to drive the separation. Active methods include dielectrophoresis,[117] magnetophoresis,[118] acoustophoresis,[119] various optical methods[120,121] and a family of flow field fractionation methods with different fields driving the separative displacement.[122–125] Passive methods are generally based on hydrodynamics and particle-solid interactions between the species and the stationary phase in the fluidic system.[126,127] They include hydrodynamic filtration,[128] pinched flow fractionation[129–132] and several separation techniques based on inertial effects.[133]

1.3 Deterministic Lateral Displacement (DLD) systems

In this dissertation, we focus on one of such separation units in microfluidics, referred to as deterministic lateral displacement (DLD) system. DLD exploits the experimental observation that particles of different sizes flowing through a periodic array of cylindrical posts may migrate in different directions, thus leading to separation. We present a schematic picture explaining the separation mechanism of DLD systems in Figure 1.2. In this specific configuration, the array of obstacles is oriented at an angle α, defined as the forcing angle, with respect to the flow direction. Large particles migrate in the column direction represented by arrow C, which is defined as moving in *locked* mode. On the other hand, small particles zig zag inside the array following the direction of the flow closely, and are described as moving in *zigzag* mode. We then define the migration angle β to be the angle between the particle migration direction (on average) and the orientation of the posts (C direction in Figure 1.2). By definition, particles migrating in locked mode will have a zero migration angle, and in comparison, particles migration in zigzag mode will have a nonzero migration angle. When DLD was first introduced, particles are believed to only move in either one of the modes, however, a third mode called *mixed motion* has been proposed by Kulrattanarak *et al.* indicating potentially more complicated dynamics in particle motion.[134,135] The mixed motion was proposed to be the direct result of anisotropy induced by the geometry that was used. However, our results indicate that even with a geometry that will not induce any anisotropy, particle motion pattern inside the obstacle array still is not be a binary one.[136–138]

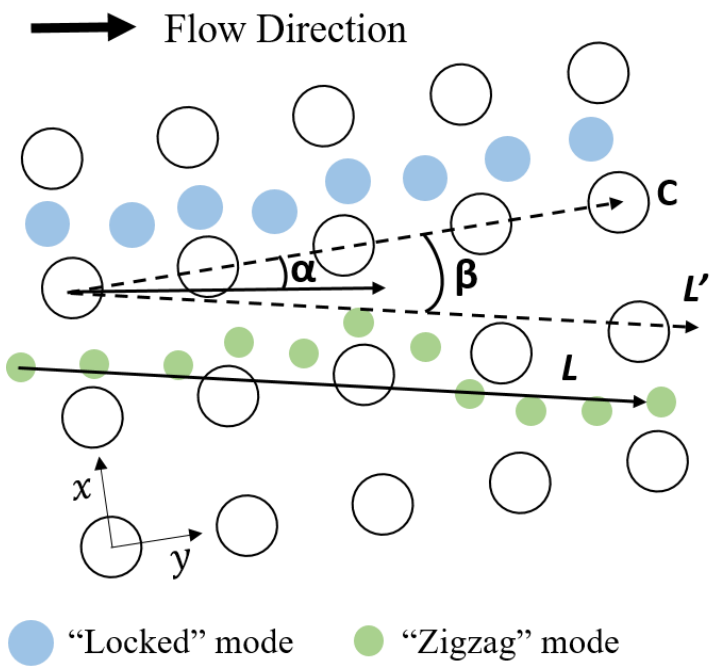

Figure 1.2 Schematic view of a DLD separation system. The large (small) solid circles represent the position of a large (small) particle at increasing times. The open circles represent the cylindrical obstacles. The solid line L denotes the direction of particle migration, and the solid line C connects centers of obstacles aligned in a lattice column (y direction). The dashed line L' that is parallel to L is drawn to better illustrate the migration.

One of the major advantages of deterministic lateral displacement (DLD) is that it can be implemented in both active and passive modes. Although DLD was initially introduced as a flow-driven, passive microfluidic method for size separation,[139] we have shown in previous work that driving the particles by external forces also results in separation depending on the orientation of the force with respect to the array of obstacles. Specifically, we have successfully used gravity, electric fields and centrifugal force to drive the separation of suspended particles in force-driven DLD (f-DLD).[140–144,2,3]

Due to the ability to achieve high-resolution fractionation of biological samples in a label-free manner both in active and passive modes, DLD has been used in numerous

applications in the field of bioengineering. Examples involving the fractionation of cells include the separation of red blood cells, white blood cells, platelets and even parasites from blood samples,[145–153] as well as the isolation of various cancer cells[154–156] and cardiomyocytes[157]. At the molecular level, periodic micro structures have long been utilized in DNA sorting.[158–161] In this area, DLD resulted in faster, continuous flow schemes that could increase througput.[139,162,163] Another important feature of DLD systems is that, in addition to size-based separation, differences in shape[164] and deformability[147,165–169] could also result in separation.

As capable and widely applicable as DLD is, various modifications to the stationary phase have been explored to further improve separation quality, both in general and for specific applications. Loutherback *et al.* proposed using triangular posts to reduced clogging and increase throughput.[170] Zeming *et al.* and Ranjan *et al.* considered more complex pillar shapes and observed effective separation of non-spherical particles, including red blood cells and rod-shaped bacteria.[146,148] Simulation have also been performed to investigate the utility of various post shapes.[171–173]

In spite of all the modifications and improvements, there are still limitations on current DLD systems. First, limited by the current microfabrication technology for microfluidic systems, the parameters of the obstacle array have to be predetermined and stay fixed in a single device, making them not reconfigurable. Additionally, in all the DLD systems that have been reported throughout the years, the height of the post remains comparable to the sizes of particles that are to be separated, which limits the particle motion to be strictly 2D. Note that in all the modifications made on the stationary phase of DLD systems, the

obstacles are exclusively solid, which bears the question that if changing the properties of the obstacles will further broaden the scope of applications for DLD systems.

1.4 A bird's-eye-view

In this dissertation, we first introduce the specifics of the DLD system design in terms of different geometries, theoretical models, and the complexity of particle motion inside the obstacle array to provide the necessary context for further discussions.

To address the reusability issue of the DLD systems, we propose a reconfigurable array design and test the idea in a Stokes flow environment. Previously, in order to achieve fractionation of a polydisperse sample in one single device, an obstacle array with a variety of row shift and gap sizes arranged in series is the go-to design.[139,162,174] We will discuss the design parameters in more details in Chapter 2. One of the obvious shortcomings associated with this specific design is that, in order to accomplish efficient and precise separation, the length of the obstacle array scales with the polydispersity of the sample. In our work, we proposed an array design with a rotating circle in the middle of an otherwise traditional obstacle array. With the rotating circle, our design is highly reusable and is capable of separating polydisperse chemical or biological sample in a continuous fashion. We observe that a sharp transition from locked mode to zigzag mode remains present for all particles and the critical angle varies with particle size, thus enabling size separation. And due to the reusable nature of the proposed array design, we are able to conveniently collect data on numerous different configurations using one single device.

We then present a simple concept to enhance separation in DLD systems, based on extending the traditionally 2D method into the third dimension by using an array of long cylindrical posts. First, we demonstrate that when projected onto the basal plane of the array, the particles in-plane migration patterns are analogous to those present in the force-driven 2D-DLD case. More importantly, we observed that the particle out-of-plane displacement (displacement along the obstacle) depends on the in-plane motion, with the largest displacements for each type of particle observed when the forcing angle is close to the corresponding critical value. Therefore, the differences in critical angle with particle size not only enable in-plane separation but also lead to different out-of-plane displacements that can be harnessed to enhance the separation ability of DLD systems. Based on such observation, we then demonstrate that a polydisperse suspension containing three different sizes of particles can be fractionated into its individual components using the proposed 3D-DLD system, with excellent efficiency and purity.

Taking DLD research in a completely new direction, we demonstrate a novel DLD system in which the traditional array of solid pillars is replaced by an array of anchored liquid-bridges. We show that at low Stokes and Capillary numbers the proposed system works similarly to the solid case, enabling excellent separation. In addition, we observe that at larger Stokes numbers particles could be separated based on density. This is a probably a combination of inertia and capillary effects, as we observed significant deformation of the liquid-bridges in this case. This suggests that working at similar capillary numbers at the microscale could enable alternative ways to separate particles beyond differences in size.

Inspired by the liquid-DLD idea, and moving on from particle separation, we further extend DLD systems to a completely new area of application, that is, air filtration. In this chapter,

we discuss the preliminary exploration of capturing airborne solid particles using water bridges. Experimental results have demonstrated that a single water bridge exhibits excellent capture efficiency that depends on the particle incoming position and Stokes number. We believe that with an optimal array design, the proposed system is capable of achieving excellent gas cleaning performance in a cost effective fashion.

2 Principles of Deterministic Lateral Displacement system design

2.1 Fluid motion at zero Reynolds number

As a technology that is proposed and developed mostly in microscale, DLD takes advantage of many fluid phenomenon that are unique to microfluidics. Here, let us first consider the Navier-Stokes (N-S) equation for Newtonian fluid:

$$\rho\left(\frac{\partial v}{\partial t} + v \cdot \nabla v\right) = -\nabla p + \eta \nabla^2 v \tag{2.1}$$

where ρ, v, p, η denotes fluid density, velocity, pressure and viscosity respectively. We then nondimensionalize the N-S equation with characteristic length *L*, flow velocity *U*, and

pressure $p_0 = \mu U/L$ and obtain non-dimensional length $l^* = l/L$, velocity $v^* = v/U$, time $t^* = \frac{t}{L/U}$, and pressure $p^* = \frac{pL}{\mu U}$ respectively.

Note that we use the hydraulic diameter of a rectangular channel D_{H} as the characteristic length of our system, and it can be calculated with equation

$$L = D_{\mathrm{H}} \equiv \frac{2wh}{w+h} \tag{2.2}$$

w and *h* here are the width and height of the channel. In most DLD systems, since the width of the channel is much larger than the height of the channel, that is $w \gg h$, we can reduce equation 2.2 to $D_{\mathrm{H}} \approx 2h$. The nondimensional N-S equation can then be written as:

$$\mathrm{Re}\left(\frac{\partial v^*}{\partial t} + (v^* \cdot \nabla^*)v^*\right) = -\nabla p^* + \nabla^{*2} v^* \tag{2.3}$$

Reynolds number can be obtained from equation 2.4 and it measures the ratio of inertial forces to viscous forces in the flow filed.

$$\mathrm{Re} \equiv \frac{\rho v D_{\mathrm{H}}}{\eta} \tag{2.4}$$

In the context of microfluidics, where $D_{\mathrm{H}} \sim 10^{-5}$m and $v \sim 10^{-3}$m/s if the working fluid is water, Re is estimated to be around 0.01 which is much smaller than 1 ($\mathrm{Re} \ll 1$). With a vanishing Re, we can further simplify equation 2.4 to Stokes equation written as

$$\nabla p^* = \nabla^2 v^* \;\Rightarrow\; \nabla p = \eta \nabla^2 v \tag{2.5}$$

An important characteristic for Stokes equation is that the velocity and pressure fields are not explicitly dependent on time, meaning that the equation is invariant under time-reversal. Furthermore, the velocity field that satisfies the Stokes equation is described as "kinematically reversible".

2.2 Particle diffusion effect

To characterize the particle diffusion, we introduce the Peclet number (Pe) that is the ratio between rates of convection and diffusion of the particles. The equation for Pe can thus be written as

$$\mathrm{Pe} \equiv \frac{vw}{D_{diff}} \tag{2.6}$$

Where v and w represent the fluid verlocity and channel width respectively. D_{diff} is the diffusion coefficient, and can be calculated using Stokes-Einstein relation as

$$D_{diff} = \frac{kT}{6\pi\eta a} \tag{2.6}$$

Here k is the Boltzmann constant, T represents the absolute temperature, η represents the fluid viscosity and a is the hydrodynamic radius of the particle. Note that the projects included in this thesis are all conducted in macroscale, and according to the definition of Pe, the particle diffusion can be ignored. The typical particle size in DLD research is usually large enough that the diffusion effect is also negligible. Consequently, the diminishing diffusion effect in macro models will not affect the similarity between our results and those obtained in micro scale.

2.3 Different geometries in DLD

In terms of the array layout, there are two widely adopted geometries across all published work in DLD research, which are referred to as row-shifted parallelogram (Figure 2.1a)

and rotated-square layout (Figure 2.1b). In row-shifted layout, the obstacles within one row (a line of posts along the y/lateral direction) in a DLD system are separated by a fixed center to center distance λ_b. Each successive row is then shifted laterally with a constant distance $\Delta\lambda$ to create rhombic array. The axial distance between two successive rows as shown in Figure 2.1 is the same as the lateral center to center distance between two neighboring posts in a row, λ_b. In this layout, the rows are always perpendicular to the fluid flow. For rotated-square layout, however, rows and columns are always perpendicular to each other at an angle α with respect to the flow or external force. The center to center distance between the rows and columns usually are kept the same, that is $\lambda_a = \lambda_b$.

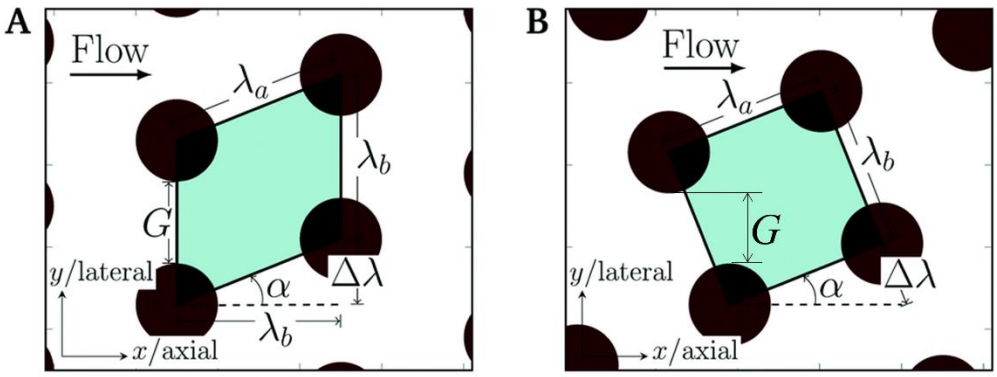

Figure 2.1 a) Row-shifted parallelogram layout and b) Rotated-square layout used in DLD system. Reproduced from Rohan *et al.*, 2017. [173]

Due to the characteristics of both geometries, there are two prevalent ways to study the particle motion in DLD systems. In most studies, especially with the row-shifted layout, the dimension of the system is predetermined and fixed, where different size of particles are forced through the periodic array of obstacles. As a result, particles with diameters

larger than a critical value, D_c, predetermined by the system can be separated from particles with diameters smaller than D_c. Another way to investigate the particle motion in DLD systems, adopted almost exclusively with rotated-square layout, is to observe the particle mode transition with varying displacement angle α (equivalent to forcing angle). A critical angle α_c can thus be determined indicating the transitional point between locked mode and zigzag mode for a given type of particle. Note that, all the work presented in this thesis are exclusively carried out with a rotated-square layout, and we continuously alter the displacement angle, defined as the forcing angle in our experiments, to investigate the mode transition for all the particles.

2.4 Theoretical Models

2.4.1 Streamline-based Model

For underlying theories of DLD systems, there are also two competing models. Inglis *et al.* first proposed a model that is purely based on hydrodynamics in the DLD system[174]. As presented in Figure 2.2, they define the term row shift $\varepsilon = \Delta\lambda/\lambda_b$, and thus each gap can be segregated into $N = 1/\varepsilon$ regions. Note that, for row-shifted geometry where the axial distance between two rows is not equal to λ_b, that is $\lambda_b \neq \lambda_a \cos\alpha$, the row shift will be then calculated by $\varepsilon = \frac{\Delta\lambda}{\lambda_b} = \frac{\lambda_a \sin\alpha}{\lambda_b}$. Assume the width of the first streamline is w, and according to the geometry, parcicle critical size can be written as

$$D_c = 2w. \tag{2.2}$$

Taking advantage of the stokes flow properties and assuming a conventional parabolic profile between two neighboring posts in a row, the total flux in each gap is also segmented into $N = 1/\varepsilon$ parts, and can be represented by the following equation:

$$\int_0^w u(x)\mathrm{d}x = \varepsilon \int_0^G u(x)\mathrm{d}x \tag{2.2}$$

where the flow profile $u(x)$ can be written as

$$u(x) = \frac{G^2}{4} - (x - \frac{G}{2})^2 \tag{2.3}$$

By substituting equation (2.3) into (2.2), the flux equation can be written as

$$\left[\frac{w}{G}\right]^3 - \frac{3}{2}\left[\frac{w}{G}\right]^2 + \frac{\varepsilon}{2} = 0 \tag{2.4}$$

We can then replace w with $D_c/2$ and obtain

$$D_c = G(1 + 2w + \frac{1}{2w}) \tag{2.5}$$

where the width of the first streamline can be solved as

$$w = \left[\frac{1}{8} - \frac{\varepsilon}{4} + \sqrt{\frac{\varepsilon}{16}(\varepsilon - 1)}\right]^{\frac{1}{3}} (-\frac{1}{2} - \frac{i\sqrt{3}}{2}) \tag{2.6}$$

Consequently, the motion of particle of a certain size traveling in a given array can be accurately predicted before experiments, which makes this relatively simplistic model extremely attractive to researchers in the field of DLD research.

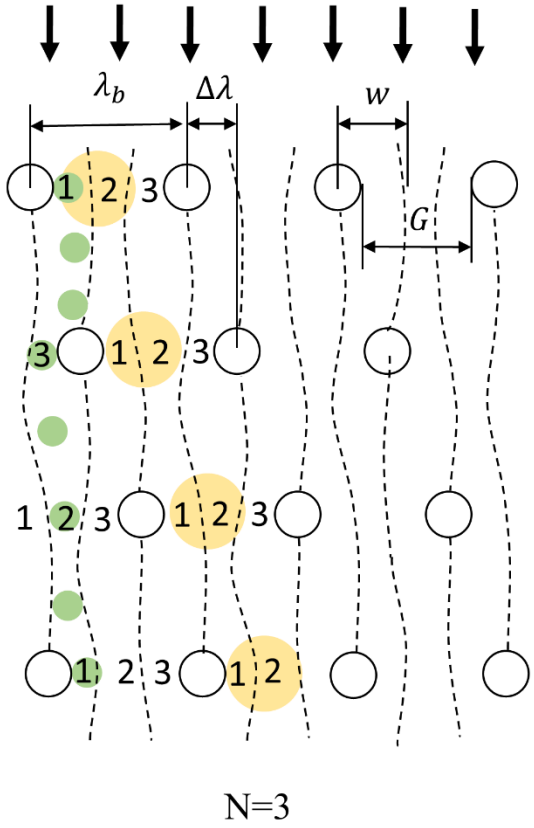

Figure 2.2 Schematic view of streamline-based model with N=3. Each gap between neighboring posts is partitioned into three sections, and the relation between particle size and the width of the first section determines which mode particle moves in.

However, as shown in Inglis's work[174], there are some observable discrepancies between the model prediction and the experimental results. Consequently, Davis proposed an empirical formula for approximation of D_c using over 20 devices with vary gap size and spherical particle size.

$$D_c = 1.4G\varepsilon^{0.48} \tag{2.7}$$

Although the streamline-based model is developed with the row-shifted layout in mind, it has been pointed out that all the theories are still applicable, if the row shift in the rotated-square layout is taken as

$$\Delta\lambda = \lambda_a \tan\alpha \tag{2.8}$$

and as a result, the row shift in rotated-square layout can be expressed by

$$\varepsilon_{rotated} = \frac{\Delta\lambda}{\lambda_b} = \frac{\lambda_a \tan\alpha}{\lambda_b} \tag{2.9}$$

Considering the experimental method where the rotation angle (forcing angle) α is continuously changed and the particle size stays constant, equation (2.4) can be rewritten as the following equation

$$\varepsilon_{rotated} = -\frac{1}{4}\left[\frac{D_c}{G}\right]^3 + \frac{3}{4}\left[\frac{D_c}{G}\right]^2 \tag{2.10}$$

For a rotated layout with aspect ratio equal to 1, that is, $\lambda_a = \lambda_b$, we obtain the equation that associate the critical forcing angle with the size of the particle

$$\tan\alpha = -2\left[\frac{w}{G}\right]^3 + 3\left[\frac{w}{G}\right]^2 \tag{2.11}$$

2.4.2 Collision-based Model

Let us then consider a model originally developed from a completely different perspective that is based on the assumption that a suspended particle only interacts with a single obstacle at a time (*dilute limit*). The trajectory of the particles is therefore determined by a sequence of individual particle-obstacle collisions[136,175,176]. For each individual particle-obstacle collision, the effect of all the short-range non-hydrodynamic repulsive forces between the particle and the obstacle is approximated by a hard-core potential. The hard-core repulsion prevents particles from coming closer to the obstacles than a given minimum separation but does not affect the particle trajectory otherwise. It is also important to note

that, in the absence of inertia effects (at low Reynolds numbers) the minimum separation between the particle surface and the obstacle during a particle-obstacle collision is uniquely determined by the initial offset b_{in} (see Figure 2.3). Therefore, for each particle size, we can define a critical initial offset b_c as the initial offset leading to the minimum separation set by the hard-core repulsion. Then, collisions can be divided into two groups subject to the relation between b_{in} and b_c. Collisions for which $b_{in} > b_c$, are *reversible*, particle trajectories are fore-and-aft symmetric and hence there is no lateral displacement after the suspended particle moves past the obstacle. On the other hand, collisions for which $b_{in} \leq b_c$ (shaded region in Figure 2.3) are *irreversible* and their outgoing offset is always b_c. That is, irreversible collisions result in a net lateral displacement of magnitude $|b_c - b_{in}|$. The fact that particles colliding with an obstacle with $b_{in} \leq b_c$, i.e. inside the shaded region in Figure 2.3, come out of the collision with the same offset b_c results in directional locking which will be discussed in the next section.

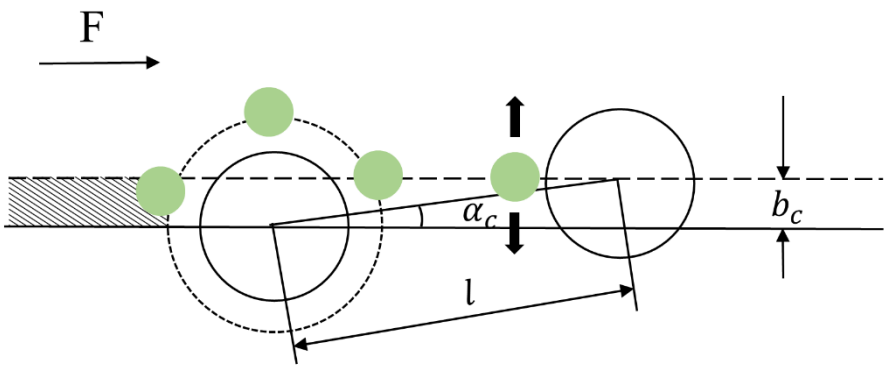

Figure 2.3 Schematic view of single particle obstacle collision. Critical offset b_c and forcing angle α determine which mode particle migrates in the DLD array.

Figure 2.4 shows three trajectories representative of the *locked-to-zigzag* transition according to the collision model just introduced. And since we are only considering a square array with $\lambda_a = \lambda_b$, we will use a single parameter l to represent the distance between neighboring obstacles. First, when the lateral displacement between two neighboring obstacles, $l \sin \alpha$, is less than b_c , as shown in Figure 2.4a, particles will be continuously displaced by successive obstacles due to irreversible collisions. That is, in this case particles will migrate in *locked mode*. In the figure, this corresponds to particles being displaced vertically up after each particle-obstacle collision and staying within a column of obstacles as indicated. On the other hand, when $l \sin \alpha > b_c$ (Figure 2.4c), particles coming out of an irreversible collision will cross through their original obstacle column, i.e they move in *zigzag mode*. The mode transition takes place when the driving force angle increases past its critical value, which depends on the particle-obstacle pair. A situation in which particles are driven exactly at the critical forcing angle is shown in Figure 2.4b. This corresponds to a particle coming out of an irreversible collision and heading into the next collision with $b_{in} = 0$, as shown in the figure, which explains the sharp nature of the transition. Given b_c, and assuming that successive collisions are independent, the model is able to predict the migration angle at any forcing angle.

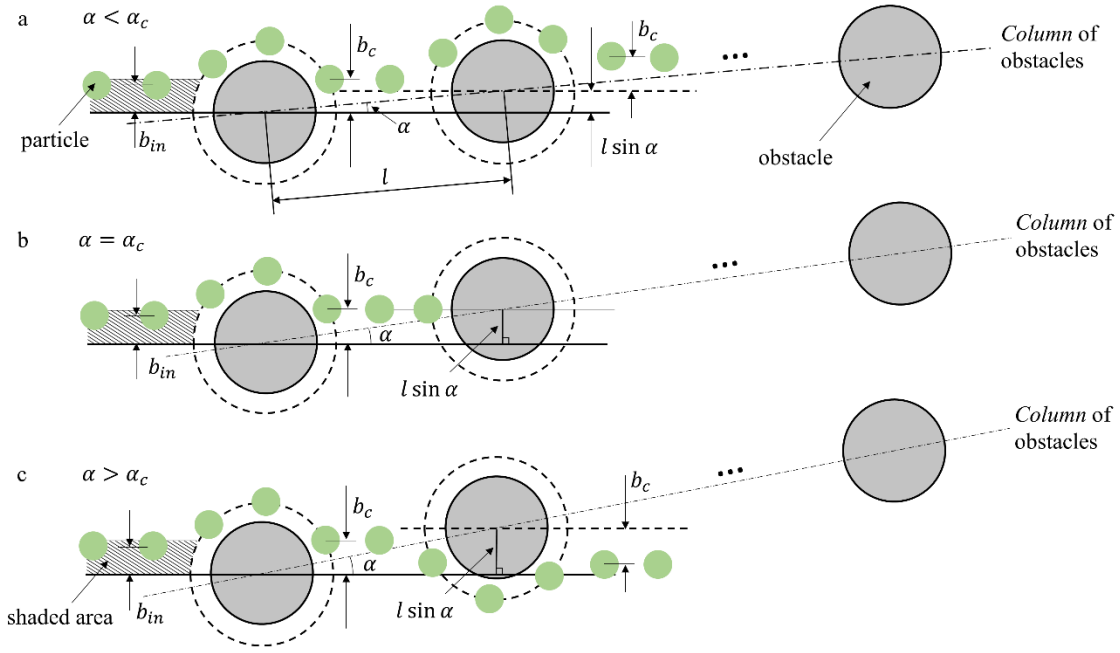

Figure 2.4 Schematic view of possible outcomes of a particle-obstacle irreversible collision depending on the magnitude of the lateral shift between obstacles $l \sin \alpha$ compared to the critical impact parameter b_c. Note that collisions are irreversible, $b_{in} < b_c$ (shaded area), and particles come out of the interaction with the outgoing offset equal to the critical impact parameter b_c. a) A forcing angle such that $l \sin \alpha < b_c$, resulting in particles migrating in *locked mode*. b) A forcing angle corresponding to $l \sin \alpha > b_c$, which leads to particles migrating in *zigzag mode*. c) Forcing at the critical angle, i.e. $l \sin \alpha = b_c$.

2.5 Mixed motion and directional locking

2.5.1 Mixed motion

Since the introduction of the concept of DLD, particles are assumed to move in one of two different modes, both for the row-shifted layout and for the rotated-square layout. To be more specific, as shown in Figure 1.2 and Figure 2.2, large particles that are restricted by the direction of the column, by definition, are moving in the locked mode. In comparison, the smaller particles that are moving in zigzag mode are able to cross columns and follow the direction of the flow or the external force more closely. However, as the research in the

field progresses, it has been repeatedly pointed out that the motion of the particles inside the stationary array of obstacles is more complicated than such binary assumption.

Kualrattanarak *et al.* found out that for a large class of array designs with row-shifted geometry, the distribution of flow lane width between two neighboring particle are in fact asymmetric, contradictory to the conventional parabolic flow profile assumption that is proposed by Inglis *et al.*[134,135] And because of the asymmetry in the flow profile, particles of certain sizes will move in a way that they neither follow the flow/external forces exactly nor are locked by a column of posts. Kualrattanarak *et al.* defined this third type of motion as mixed motion. Specifically, as shown in Figure 2.5, besides the original critical size obtained by assuming a parabolic profile between neighboring posts D_c, there exist a second critical particle size D_m that determines the transition from mixed motion to zigzag mode. To be more specific, if particle diameter D_p is smaller than the first critical size, that is, $D_p < D_c$, the particle is observed to move in the zigzag mode. If the particle diameter is in between the first critical size and the second critical size, $D_c < D_p < D_m$, the particle moves in mixed motion. And if particle size is larger than the second critical size, $D_p > D_m$, it moves in locked mode.

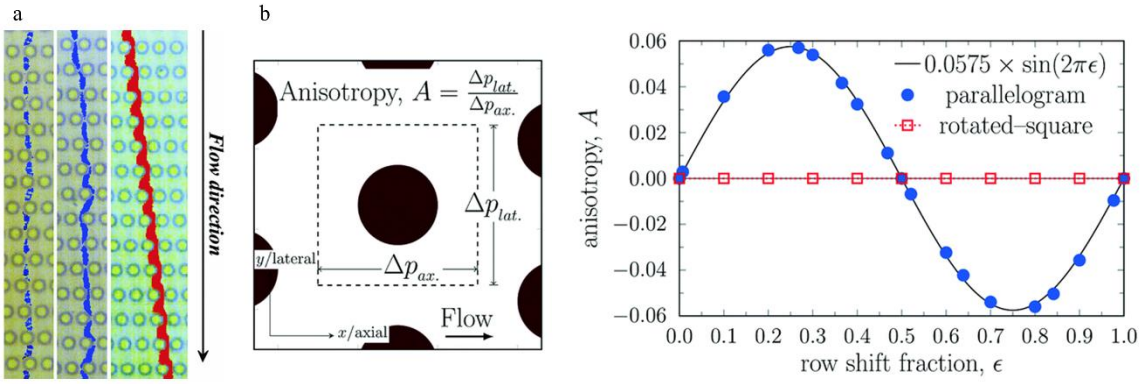

Figure 2.5 a) From left to right particles are moving in zigzag mode, mixed motion and locked mode. Reproduced from Kulrattanarak *et al.*, 2011.[134] b) The anisotropy induced by both layouts as a function of row shift faction ε. Reproduced from Vernekar *et al.* 2017.[173]

As Vernekar *et al.* detailed through extensive Lattice-Boltzmann simulations,[173] in consistence with the work of Kualrattanarak *et al.*, mixed motion in row-shifted design can be explained by the geometry induced anisotropy, which describes the tendency of an array to induce a pressure drop perpendicular to the main flow direction in a device. The induced anisotropic pressure will create a secondary background re-circulatory flow that might cause the primary flow to no longer move parallel to the side walls everywhere in a device, which results in certain particles moving in the so called mixed motion. As shown in Figure 2.5b, for row-shifted design with aspect ratio of 1, meaning $\lambda_a = \lambda_b$ (see Figure 2.1a), the induced anisotropy vary with the row shift fraction ε as a sine function, and only at $\varepsilon = 0.5$, the induced anisotropy will be reduced to 0 due to symmetry of the geometry. In comparison, the rotated-square layout with aspect ratio of 1 will never induce anisotropy into the flow field. Vernekar *et al.* also point out that changing the aspect ratio to any value other than 1 in both arrays will result in excess anisotropy except for row-shifted layout with row shift ration $\varepsilon = 0.5$ and that arrays of unconventional shapes of obstacles will result in excess anisotropy in both layout as well.

2.5.2 Directional Locking

Using the collision-based model, our group discovered that in a rotated-square layout with aspect ratio of 1, where no anisotropy is induced, the direction that particles migrate inside the obstacle array is not strictly binary either. In fact, for any given b_c, if we plot the migration angle for a given particle predicted by collision-based model with respect to the forcing angle, exemplified by the solid curve in Figure 2.6b, we observe a devil's stair case like relation between the two angles. And the phenomenon that for finite intervals of the forcing angle, the corresponding particle migration angle stays constant is defined as *directional locking*. Specifically, we find both in experiments and theoretical exploration that, particle motion inside the obstacle array is always periodic, and the periodicity of a trajectory can be described by its average direction [*p*,*q*], where p, q are Miller indices as shown in Figure 2.6a. With this notion, particles that move in locked mode can be described as moving with periodicity [1,0]. The particle migration angle by definition can thus be calculated using $\tan\beta = q/p$. As detailed in the work of Risbud *et al.*,[176] the relation between the particle migration angle β and forcing angle α can be described by the inequality

$$|\sin(\alpha - \beta)| \leq \frac{b_c}{sl}, \tag{2.8}$$

where $s([\mathrm{p},\mathrm{q}]) = \sqrt{p^2 + q^2}$.

Note that the inequality above serves only as the necessary conditions for the periodicity of the particle trajectory, meaning that if a particle is observed to be moving inside the obstacle array with periodicity [*p*,*q*], then the relative magnitude of forcing angle and migration angle must satisfy the inequality (2.8). Conversely, in an array with dimension

l, for a given forcing angle α and critical offset b_c, there might exist multiple [p,q] pairs that satisfy the inequality (2.8). Physically, however the particle will take the periodicity that's closest to [0,0] out of all the possible [p,q] pairs that satisfy the inequality (2.8). As a result, given the array dimension l, forcing angle α, and particle critical offset b_c, the particle periodicity can be solved as a mixed-integer minimization problem, that is, to minimize $s([\mathrm{p},\mathrm{q}]) = \sqrt{p^2+q^2}$ for integers pair [p,q] that satisfys $p > 0$, $q \geq 0$ and the inequality (2.8).

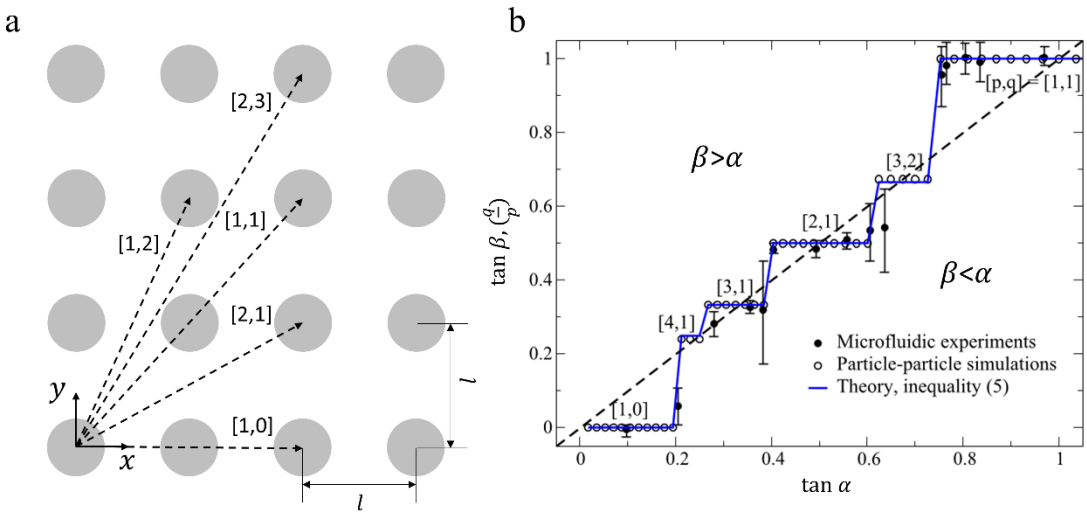

Figure 2.6 a) Potential periodicities for particle trajectories inside the DLD array b) An example of the collision-based model fitting result. The solid Devil's staircase like line represent the relation predicated by collision-based model between migration angle and forcing angle in DLD systems. The dashed line represent situation where particle migrate in the exact direction of the flow or external force. Both figures are reproduced from Risbud and Drazer, 2014.[176]

As shown in Figure 2.6b, the collision-based model describes the microfluidic data,[140] the particle-particle simulation result obtained by Frechette *et al.*[177] excellently well. In this dissertation, we primary use collision-based model to fit our experimental data, and we

find that it works quite well in describing results obtained both from flow driven and from force driven DLD systems.

2.6 Summary

In this thesis, we exclusively utilized a rotated-square layout with $\lambda_a = \lambda_b$ to avoid induced anisotropy. Another advantage of using a rotated-square layout is that we have an alternative way of studying the critical behavior of particles inside the obstacle array. Specifically, instead of identifying the critical particle size for a given array, we are able to continuously alter the rotation angle of the array, which results in continuously changing forcing angles, and then determine the critical (forcing) angle for particles of any given size.

To characterize particle motion inside the obstacle array, we focus first on establishing the existence of a sharp transition from locked mode to zigzag mode for particles of a certain size. We then are able to find the critical angle based on the transition point in the range of forcing angles studied. For the flow driven experiments, we compare the experimental critical angles with the values predicted by the streamline-based model to evaluate the accuracy of the model. By continuously varying the forcing angle in our experiments, we also are able to obtain a corresponding range of migration angles. We evaluate the applicability of the collision-based model by comparing the experimental migration angle vs. forcing angle curve with the same curve predicted by the model. For all projects included in this thesis, we closely follow the described steps to analyze the data.

3 Deterministic Lateral System with a reconfigurable obstacle array

3.1 Introduction

As mentioned in the previous chapter, since its introduction, particles in DLD arrays are considered move only in two modes, that is, locked mode and zigzag mode, depending whether or not the particles follow the direction of the flow/force direction closely. Attributed to the existence of induced anisotropy, however, the existence of a mixed motion discovered in the row-shifted parallelogram layout will in fact compromise the separation ability of the DLD device rather than enhance it. The phenomenon of directional locking will in theory provide us with more opportunities to separate particle with different sizes. Explicitly, for certain forcing angles, particles of different sizes might take different

periodicity resulting in their separation, the first critical angle (which in this thesis is referred to simply as critical angle) is still considered to be the deciding parameter for particle size separation. As a result, the DLD method using arrays with a fixed row shift fraction ε or forcing angle α is still widely acknowledged to be a binary separation scheme by nature.

To improve the separation ability of the DLD systems and to achieve separation of a polydisperse sample in a single separation system, the prevalent solution is to use several DLD arrays, with varying ε, arranged in sequence.[145] Although effective, the array-in-series design will often result in a relatively long device design if the sample contains a considerable number of particle sizes, which will render it to be extremely difficult to incorporate the separation functional unit into a micro total analysis system.

Here, we propose an alternative array design with a rotating circular disk at the center of the array, which allows the forcing angle to be continuously changed in real time. To demonstrate the idea without the limitation of microfabrication techniques, we use macromodels of flow-driven DLD devices to investigate conditions leading to size-separation of suspended particles, depending on the geometry of the obstacle array and the average orientation of the pressure-driven flow. Specifically, we consider two arrays with different size of cylindrical posts, and continuously vary the direction of the average flow to cover a wide range of forcing angles ($0 < \alpha < 30°$). The present set of experiments shows that the motion of suspended particles is analogous to that observed in the f-DLD case. Specifically, we experimentally show: (i) the existence of a *locked mode* for all particle sizes, in which the average migration angle is $\beta=0°$ (particles move along a column of obstacles) for a range of forcing angles $\alpha_c > \alpha > 0$; (ii) a sharp transition from *locked*

mode to *zigzag mode* in which particles move periodically at certain lattice directions; (iii) a monotonic increase in the critical angle at which the *locked-to-zigzag* transition occurs with particle size. Finally, we observe that the migration angle predicted by the collision-based model over the entire range of forcing angles describes the particle motion accurately.

3.2 Experimental set-up

Our experimental setup is a scaled-up version of a microfluidic DLD system, consisting of a closed channel of width $L = 280\text{mm}$ fabricated using acrylic plates (see Figure 3.1a). A square array of obstacles ($l = 200\text{mm}$) is centered in the channel and a circular disk is cut at the center of the array as shown in Figure 3.1b. The rotating central part allows us to vary the forcing angle continuously. Additionally, to study the effect of obstacle size on particle trajectory, two different arrays are used. We show a schematic of the geometry of the arrays in Figure 3.1c. The difference between the two arrays is the diameter of the obstacles, either $\text{d} = 1\text{mm}$ or 2mm. The height of the channel (and obstacles) is h=5mm and the open gap between obstacles is 4mm, in both arrays. They were fabricated using a 3D printer (Objet350 Connex, Stratasys). The reason for the rectangular shape of the complete array is to ensure a uniform flow over the width of the channel (except close to the walls). A circular array alone, in contrast, would not provide a uniform flow resistance over the width of the channel and could lead to significant flow variations. In addition, the Hele-Shaw type of configuration used in the experiment, in which the length of the channel is much larger than its height, $\text{l} \gg \text{h}$, makes entrance effect negligible for low Reynolds

number flows. The flow is driven by a constant pressure drop generated by a Mariotte's bottle and distributed over the channel width using a manifold at the inlet.

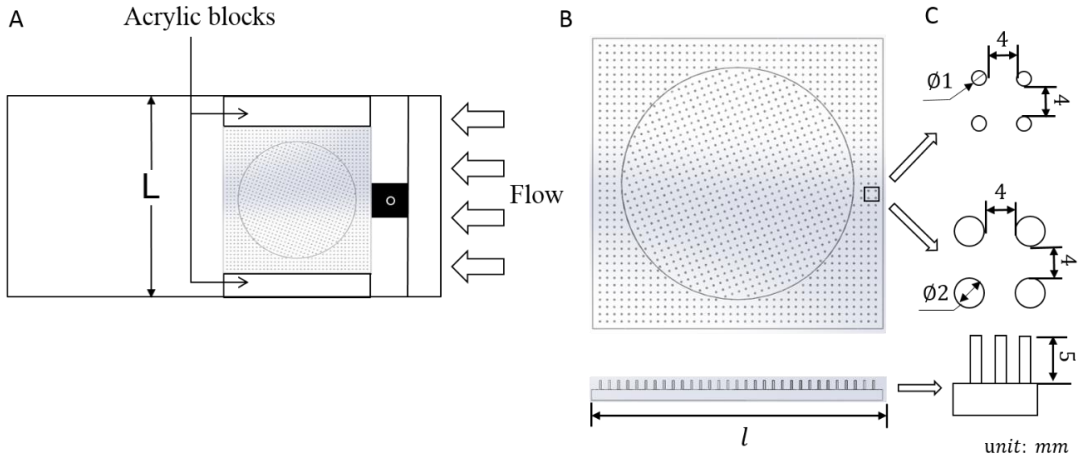

Figure 3.1 a) Schematic view of the experimental setup. b) Top and side view of the array of obstacles. c) Representation of the geometry of the array.

3.3 Materials and methods

In order to compare our results with microfluidic systems we have to satisfy both geometric and dynamic similarity. To this end, we maintain the shape of the posts (cylindrical), the spacing between the obstacles relative to their size, and the particle/obstacle aspect ratios comparable to those used in microfluidic systems, thus satisfying geometric similarity. In order to establish dynamic similarity, we need to maintain relatively low Reynolds numbers. Therefore, we use a mixture of glycerin (99% Glycerin, McMaster-Carr) and water with a volume ratio 3:2. The dynamic and kinematic viscosity of the liquid mixture is approximately $\mu = 0.016\, Ns/m$ and $\nu = 1.38 \times 10^{-5}$ m2/s, respectively [178]. The flow rate in the experiments is approximately $Q = 8$ cm^3/s, and the corresponding Reynolds

number can be estimated as $Re = Qh/Av \approx 3$, where $A = l \times h = 10cm^2$ is the cross section area of the channel. We note however, that our goal is not to reach the Stokes limit of vanishingly small Reynolds numbers but to ensure dynamic similarity between our macromodel and microfluidic systems. In fact, previous work in microfluidics has shown that DLD remains an effective separation method at moderate Reynolds numbers, e. g. Re $\lesssim 40$ [155,179]. In terms of Brownian motion, microfluidic DLD devices work in the deterministic regime, Pe $\gg 1$, a condition clearly satisfied in macroscale models. Finally, we make sure that the Stokes numbers (St) in the macromodel experiments are also small. We used nylon particles (density $\rho = 1.13 \mathrm{g}/cm^3$) of six different sizes, with diameters D =1/16" (1.59 mm), 3/32" (2.38 mm), 1/8" (3.18 mm) (McMaster-Carr), 0.072" (1.83 mm), 7/64" (2.78 mm) and 9/64" (3.57 mm) (Precision Plastic Ball Co.). We estimate a particles Reynolds number $\mathrm{Re_p} = \frac{u_\mathrm{p} D}{\nu}$, where u_p is the velocity of the particles, between 0.3 and 1.85, depending on particle size. Therefore, the corresponding Stokes numbers, $\mathrm{St} = \frac{1}{9}\left(\frac{\rho_p}{\rho_f}\right) Re_p$, are in fact small, between 0.03 and 0.2. Independent experiments are performed for each particle size, obstacle array and forcing angle. In each experiment, we analyze the trajectory of ~20-30 particles and determine the average migration angle.

3.4 Results and discussions

First, we investigate the existence of a *locked mode*, in which particles move along a column of obstacles (β=0°) for forcing angles lower than a certain critical angle. Then, we characterize the transition into the *zigzag mode* as the forcing angle increases beyond the

critical value. To this end, we introduce the probability of crossing P_c, defined as the fraction of particles that move in *zigzag mode* over the total number of particles analyzed. Alternatively, $(1 - P_c)$ is the fraction of particles locked to move in the [1, 0] lattice direction without crossing columns of obstacles (β=0°). The results are presented in Figure 3.2. Clearly, in all cases, we observe a sharp transition from no crossing (i.e. *locked mode* at β=0°) to complete crossing with $P_c = 1$. Therefore, we define the critical angle for each particle as the forcing angle at which the crossing probability is $P_c = 1/2$ (calculated by linear interpolation using the closest data points with probabilities higher and lower than 1/2). It is also clear in Figure 3.2 that the *locked-to-zigzag* transition occurs at increasing forcing angles for particles of increasing size, which demonstrates that particles can be separated by size. In addition, the fact that we observe sharp transitions without overlap between different curves indicates that these particles could be separated with high resolution.

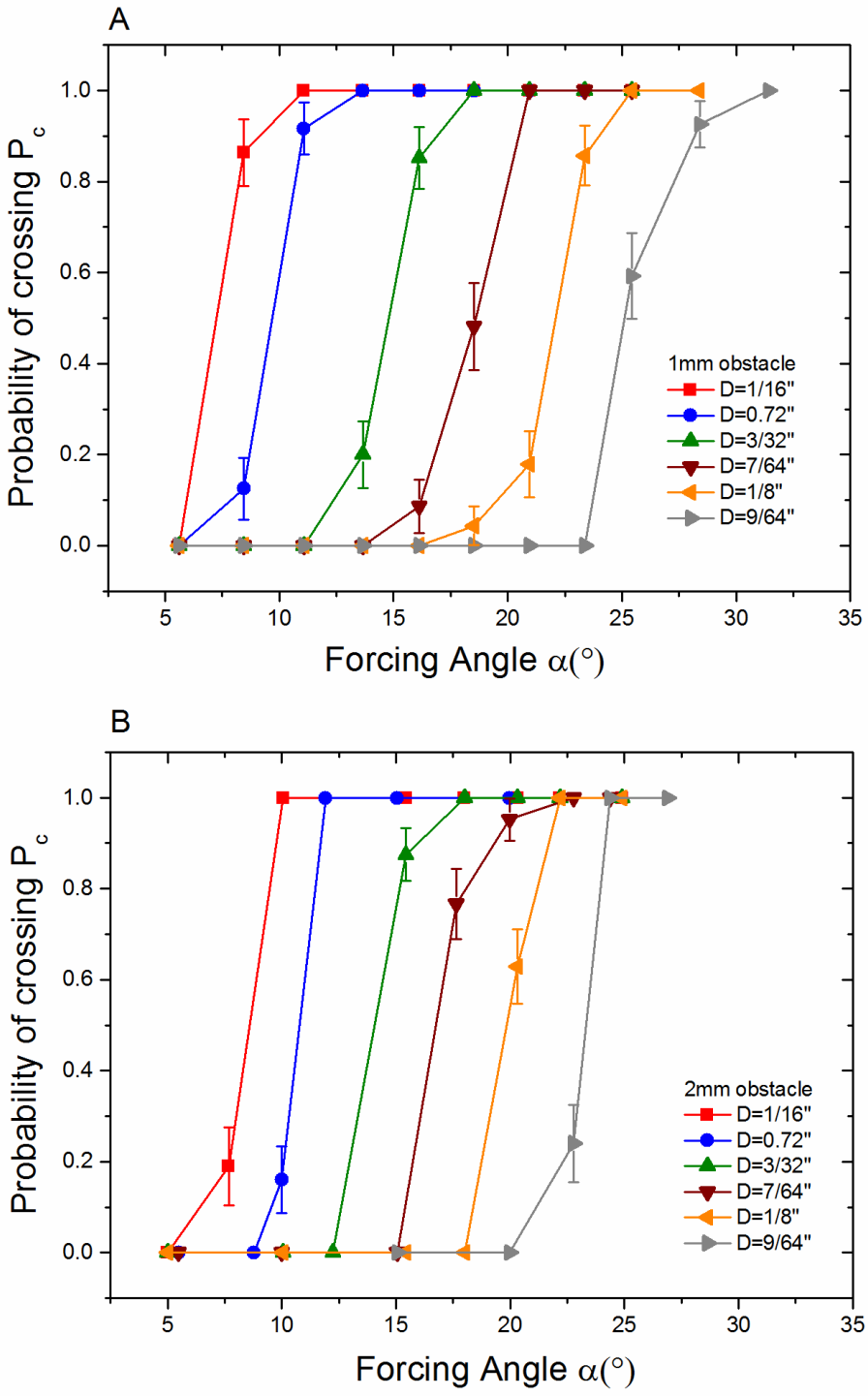

Figure 3.2 a) Probability of crossing for different size of particles for the array with smaller obstacles (1 mm obstacle diameter). b) Probability of crossing for different size of particles for the array with larger obstacles (2 mm obstacle diameter).

In Figure 3.3, we present the critical angle as a function of particle size for the two different arrays of obstacles. Interestingly, we observe a linear relationship for both arrays. In contrast, the model proposed by Inglis and coworkers, based on the streamlines in the absence of particles (*streamlines-based model*), predicts a cubic relation (solid line in Figure 3.3). We note that, in the case of large particles (e. g. D > 3 mm), inertia effects might contribute to the discrepancy between the experimental results and the streamlines-based model. On the other hand, we also observe deviations from the streamlines-based model with small particles (e. g. D < 3 mm), in which case inertia effects are probably negligible, as indicated by the small Reynolds (and Stokes) numbers.

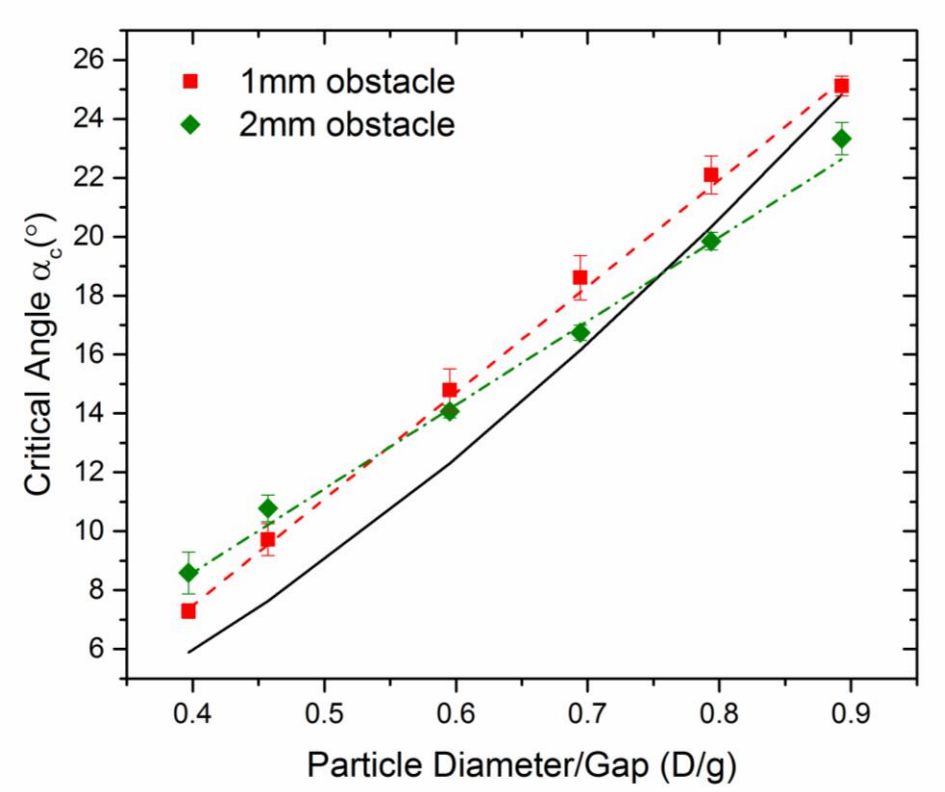

Figure 3.3 Critical angles as a function of particle size in both arrays. Particle diameter is nondimensionalized by the gap size. Straight lines correspond to a linear fit of the results. The solid curve is calculated using the model proposed by Inglis *et al.* [180]. In the array with smaller obstacles, the linear fit is $\alpha_c = 36.2861(D/g) - 6.90216, R^2 = 0.9986$. In the array with bigger obstacles, the linear fit is $\alpha_c = 28.7769(D/g) - 2.81352, R^2 = 0.9956$.

The linear dependence of the critical angle on the size of the particles allows us to estimate the size resolution that is possible with the corresponding separation system. Specifically, we first estimate the largest uncertainty in the determination of the critical angle by the largest variance (error bar) reported in Figure 3.3, $\sigma_P \sim 2°$. Then, we estimate the corresponding uncertainty in the radius of the particles using the linear correlation, and obtain $\Delta a \sim 150$ μm. Therefore, we expect excellent separation for particles that have a difference in size $\Delta a \gtrsim 300$ μm. For example, let's consider a binary mixture of particles with radius $a_1 = 0.9$ mm ($D_1 = 1.83$ mm) and radius $a_2 = 1.2$ mm ($D_2 = 2.38$ mm), that is approximately 300 μm difference in radius. Then, using the lattice with obstacles of 2 mm diameter and a forcing angle $\alpha \cong 12°$ would result in zero crossing for the large particles and complete crossing for the small ones, corresponding to ideal purity in the separation.

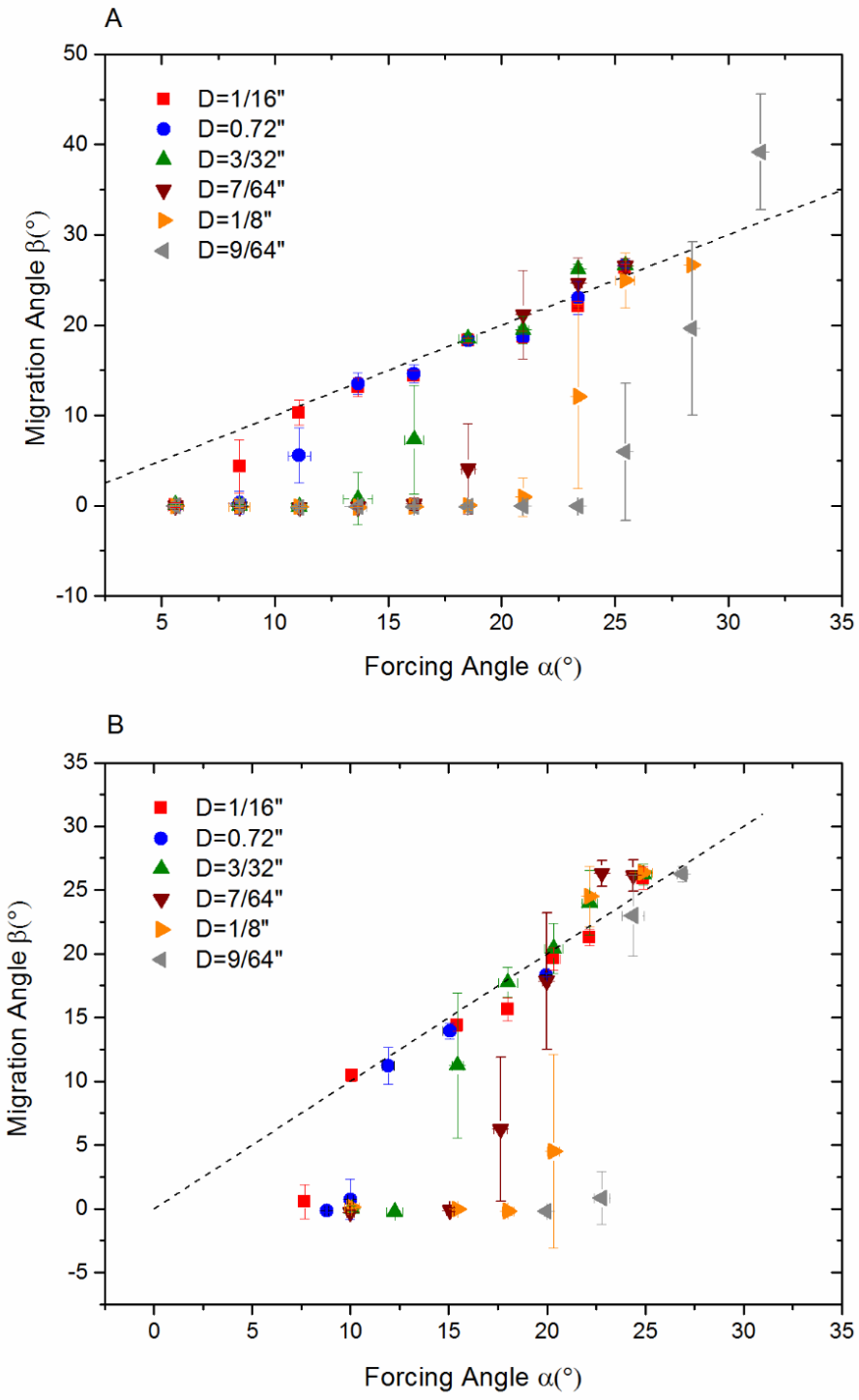

Figure 3.4 a) Migration angle as a function of forcing angle (1 mm diameter obstacle). b) Migration angle as a function of forcing angle (2 mm diameter obstacle). The dashed line represents $\beta = \alpha$ (in both plots).

Second, we investigate the migration angle in the *zigzag mode*. As we discussed in the introduction, the original DLD work by Inglis and coworkers assumed that in zigzag mode particles move, on average, parallel to the forcing angle. However, further analysis showed that this is not the case.[181,182] Similarly, previous f-DLD experiments clearly indicated that particles move periodically at specific lattice directions that, in general, are not aligned with the external force [136,140]. In Figure 3.4, we present the migration angle as a function of the forcing angle. Although in most cases the migration angles are similar to the forcing angle, there are some cases in which it is clear that $\beta \neq \alpha$.

Given particle size and geometry of the obstacle array, the critical offset is the only unknown parameter in the collision-based model. It can be calculated from the critical angle using the relation $b_c = l\ sin(\alpha_c)$ as shown in Figure 2.3.[183] After the critical offset is determined, it is straightforward to calculate the migration angle as a function of the forcing angle from geometric considerations, given that the result of every particle-obstacle collision can be predicted. In fact, only those collisions that are irreversible need to be accounted for and they simply result in a net lateral displacement perpendicular to the forcing direction.[183,184] In Figure 3.5, we show the comparison between the proposed model and the experimental results. Note that, the critical offset is determined from the crossing probability. Therefore, the comparison between the model and the migration angles at forcing angles larger than the critical one has no fitting parameters. In general, we observe good agreement between the model and the experimental results, which suggests that in the *zigzag mode* the migration angle is not necessarily the same as the forcing angle but rather results from directional locking into certain lattice directions.

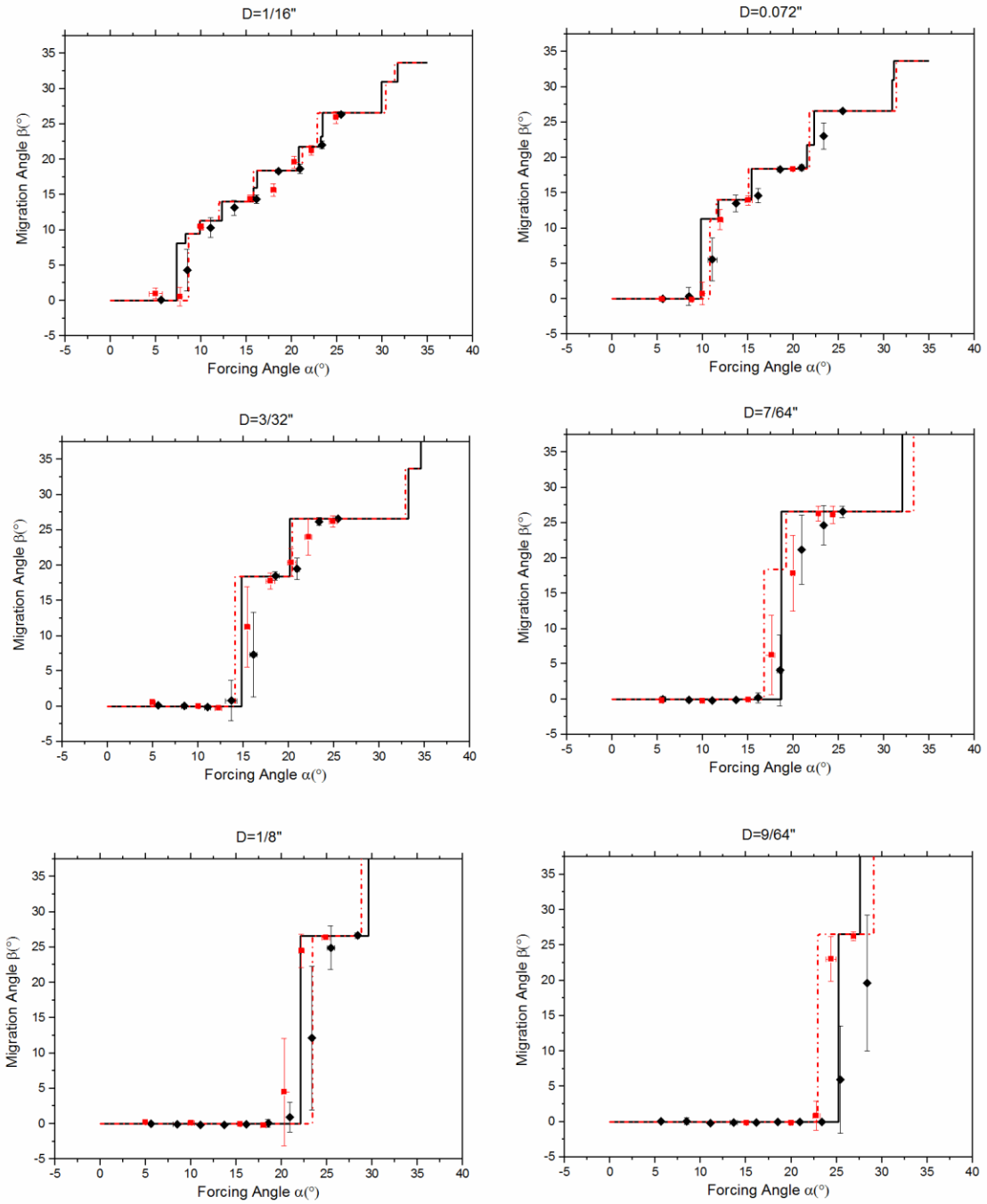

Figure 3.5 Comparison of experimental results with the proposed collision model for particles of all sizes and in both arrays. In each graph, the solid (dot dashed) line corresponds to the results predicted by our model corresponding to the critical offset calculated from crossing probability in the lattice with small (large) obstacles. Solid diamonds (squares) correspond to the experimental results obtained in the lattice with small (large) cylinders.

Finally, we obtain a second estimate of the critical angle for each combination of particle and obstacle size, by directly fitting the measured migration angles. Specifically, we vary b_c in a range of values, and by evaluating the error between stair-case graph predicted by our model corresponding to each b_c and the experimental data, we are able to find a (range of) b_c that fits the experimental result the best. The results are nondimensionalized by the obstacle radius and presented in Figure 3.6. We compare both sets of critical angles for each array of obstacles, one set of values calculated from the critical angles obtained experimentally and one set of values obtained from the direct fitting of migration angles. Note that, in most cases, due to the stair-case type of curve predicted by the model, the fit using the migration angles results in a range of critical offsets instead of a single value. Therefore, in Figure 3.6, we report the average value and the error bars correspond to the uncertainty interval. Interestingly, we observed that both the two sets of nondimensional critical offsets seem to follow a universal linear trend with respect to the nondimensional particle size. The results need to be further validated at the micro scale, but this simple correlation could provide the necessary information to tailor the design of DLD systems to specific applications.

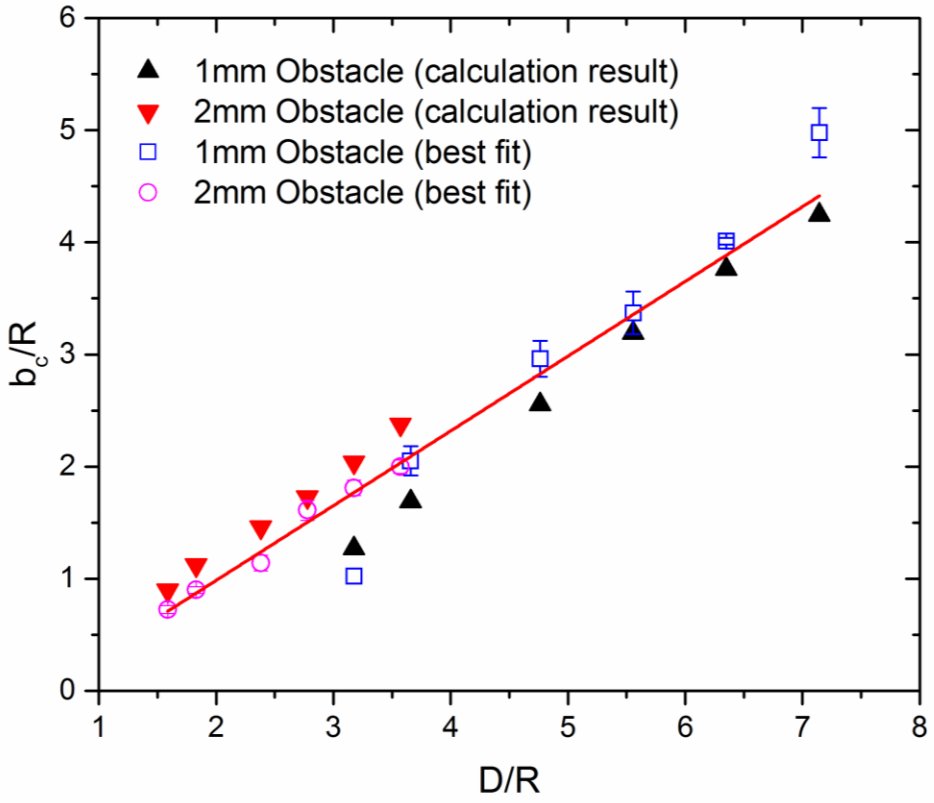

Figure 3.6 Nondimensional critical offset as a function of nondimensional particle size. The circle (square) symbols correspond to the array with large (small) obstacles. The two sets of b_c values correspond to the calculation based on the crossing probability (solid symbol) or the best fit of the migration angle with the collision model (open symbol). The solid line is a linear fit of both sets of critical offsets ($b_c/R = 0.66674\, D/R - 0.34982, R^2 = 0.94196$).

3.5 Conclusions

We used a macromodel to investigate flow-driven DLD microfluidic systems over a wide range of forcing angles (direction of the average flow with respect to a column in the array of obstacles). We demonstrated the existence of a *locked mode* for all the different particles considered here and in two arrays with different obstacle sizes. In this *locked mode*, corresponding to small forcing angles, the migration angle of the particles remains β=0° until a sudden transition into *zigzag mode* occurs when the forcing angle reaches a critical

transition angle. The fact that the transition occurs at increasing forcing angles for larger particles enables particle separation. In fact, we observed a linear trend for the critical angle as a function of particle size. In addition, we showed that a simple collision model, based on irreversible particle-obstacle interactions, not only captures the sharp *locked-to-zigzag mode* transitions, but also predicts the migration angles at larger forcing angles. Unfortunately, the prevalent DLD experiments in microfluidics have been focused on small and fixed orientations of the driving flow field and no general results are available for the behavior of particles of different size as the forcing angle increases. Therefore, further microfluidic experiments are needed to validate the linear trend in the critical angle as a function of particle size observed in the macromodels used here.

4 Gravity driven deterministic lateral displacement for suspended particles in a 3D obstacle array

4.1 Introduction

To continue our effort in improving the separation ability of DLD devices, we notice that in previous DLD research, the height of the obstacle array has always been limited to be comparable to the size of the particles that are being studied. As result, the particle separation has been exclusively based on the motion of the suspended particles in the plane of the array, that is, the plane perpendicular to the cylindrical posts, contributing to the binary fractionation limitation of DLD devices. Here, we propose a three-dimensional (3D)

extension of DLD systems that overcomes the limitation by taking advantage of the out-of-plane motion of the suspended particles. Specifically, we investigate an obstacle array with long cylindrical posts in which particles not only move *in-plane*, that is, perpendicular to the obstacles, but also *out-of-plane*, i.e. in the direction along the cylindrical obstacles. We designed a macroscopic setup that can be altered to achieve arbitrary orientation with respect to the driving force (gravity). In this way, we are able to control the relative magnitude of the in-plane and out-of-plane components of the driving force. We perform experiments with particles of different sizes and for a wide range of force orientations with respect to the obstacle array. In all cases, we observe that the *in-plane motion* of the particles, that is the motion projected onto the plane of the array, is analogous to that found in two-dimensional (2D) DLD systems. In particular, there exists a transition from *locked mode* in which particles move in a principal direction of the array to *zigzag mode* in which they follow the external force more closely. Analogous to the 2D-DLD case, the fact that particles of different size transition from *locked mode* to *zigzag mode* at different orientations of the driving force is the basis for their in-plane separation. More importantly, we show that the out-of-plane motion of the particles is also size dependent. Therefore, 3D-DLD enables the simultaneous separation both in-plane and out-of-plane, thus increasing resolution and making it possible to fractionate a polydisperse suspension into multiple streams. In fact, based on our characterization experiments we demonstrate the simultaneous separation of particles of three different sizes coming out of our 3D-DLD system with excellent results.

4.2 Experimental set-up and materials

A schematic view of the experimental setup is presented in Figure 4.1. The 3D array of obstacles is created using steel rods (diameter $D = 2$ mm, McMater-Carr Inc.) arranged in a square array between two parallel acrylic plates (see Figure 4.1a). The separation between rods in the array is $l = 6$ mm, and the separation between the acrylic plates is $L = 14$ cm. The two acrylic plates are fixed on a square acrylic base so that the obstacle array can be rotated as one solid object. The obstacle array is then placed on a supporting rectangular acrylic plate that can be rotated to an arbitrary angle θ with respect to a level surface (see Figure 4.1b). In addition, the base can be arbitrarily rotated an angle φ with respect to the supporting plate, as shown in Figure 4.1c. The tilt angle, θ, and the rotation angle, φ, let us control the orientation of the obstacle array with respect to gravity.

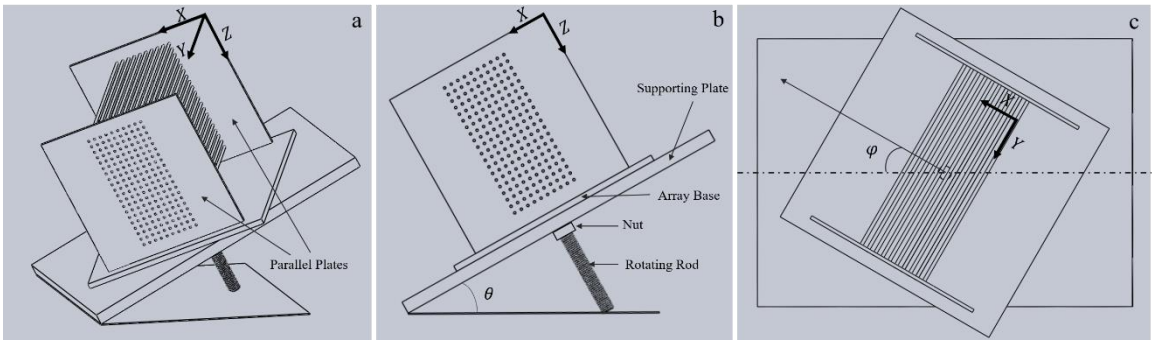

Figure 4.1: Schematic view of the experimental setup. a) Perspective view. b) Side view for a rotation angle $\varphi = 0°$. c) Top view of the rotating obstacle array on the supporting plate.

We then place our 3D-DLD system into a container filled with corn oil (viscosity $\mu = 52.3$ mPa · s, density $\rho_f = 0.926$ g/cm^3). We performed experiments covering tilt angles

from 15.8° to 32.0°, and the rotation angle is varied (approximately) between 5° and 85°, depending on particle size. In each experiment, we fix the slope and rotation angles and release particles individually into the system, to eliminate particle-particle interactions. We use nylon particles with diameters $d = 1.59, 2.38$ and 3.16 mm (McMater-Carr Inc.), and a total of 20-30 particles are tracked in each experiment. The density of the particles is $\rho_s = 1.135\ \mathrm{g/cm^3}$. The particle Reynolds number in our system is given by $\mathrm{Re_p} = \frac{\rho_f U d}{\mu}$, where U is the characteristic velocity of the particles. The largest value, estimated using the average sedimenting speed of the largest particles (U=3.6 $\mathrm{mm/s}$), is $\mathrm{Re_p} \sim 0.2$. The Stokes number is given by $\mathrm{St} = \frac{1}{9}\left(\frac{\rho_s}{\rho_f}\right)\mathrm{Re_p}$, and the corresponding maximum value is thus estimated to be $\mathrm{St} \sim 0.03$. We note that these values are consistent with those typically found in microfluidic systems.

4.3 Problem geometry and coordinate system

As shown in Figure 4.1a, the X and Z axes define the basal plane of the obstacles, and the Y axis is taken as the direction parallel to the cylindrical posts (parallel to their axes). Figure 4.2a is a schematic representation of two typical trajectories followed by particles inside the 3D obstacle array, one corresponding to *zigzag mode* (small circles) and the other one corresponding to *locked mode* (large circles). Figure 4.2b shows the projection of the trajectories onto the XZ plane.

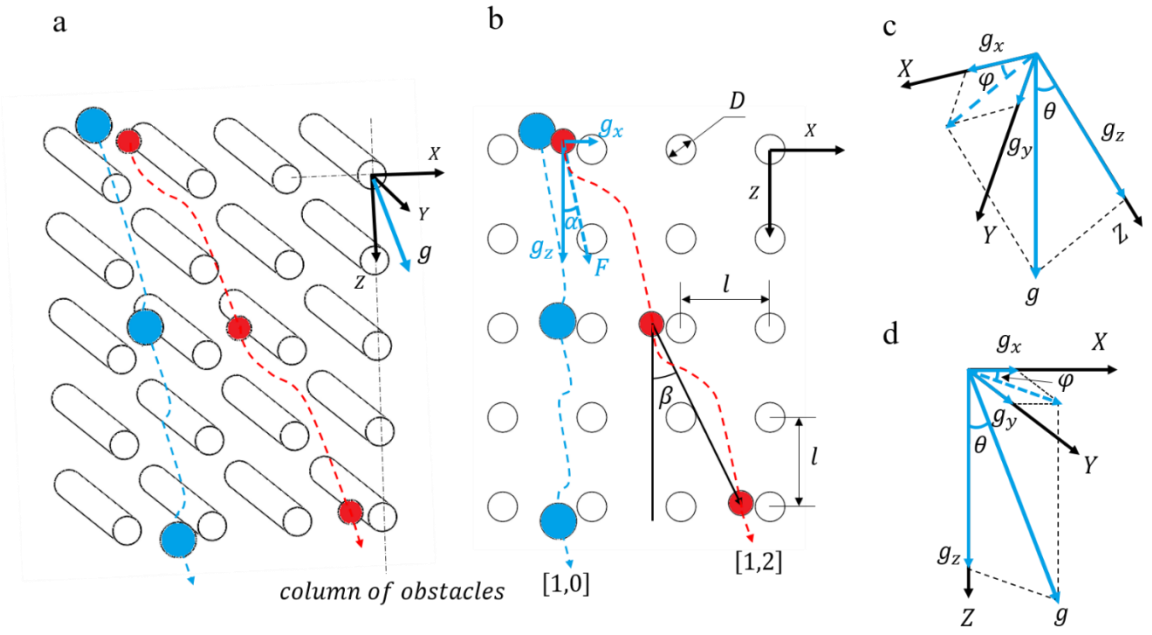

Figure 4.2: a) Typical particle trajectories. The smaller circles represent the trajectory of a particle moving inside the obstacle array in *zigzag mode* with a [1,2] periodicity, and the larger circles represent the trajectory of a particle moving in *locked mode*, i.e. [1,0] periodicity. b) Projection of the trajectories shown in a) onto the XZ plane, indicating the forcing angle α and the migration angle β. c) Coordinate system of the setup viewed from the laboratory reference frame (gravity is pointing vertically downwards). d) Gravity force in the coordinate system of the setup.

When projected onto the XZ plane, particle trajectories can be compared to the 2D case. To this end, we determine the forcing angle in the XZ plane, α, i.e. the angle between the in-plane projection of the force acting on the particles and the Z axis, and the migration angle in the XZ plane, β, i.e. the angle between the projected trajectory (onto the XZ plane) and the Z axis (see Figure 4.2b). The different components of the driving force (gravity) can be written in the terms of the slope angle θ and the rotation angle φ as follows (see Figure 4.2b, 2c and 2d):

$$g_z = g\cos(\theta), \tag{1a}$$

$$g_x = g\sin(\theta)\cos(\varphi), \tag{1b}$$

$$g_y = g\sin(\theta)\sin(\varphi). \tag{1c}$$

The forcing angle in the XZ plane is therefore given by

$$\tan(\alpha) = {}^{g_x}/_{g_z} = \tan(\theta)\cos(\varphi). \tag{2}$$

Note that for a fixed tilt angle θ, the possible forcing angles that can be obtained by varying the rotation angle φ are limited to $0 < \alpha < \theta$.

4.4 Results and discussion

4.4.1 Particle in-plane motion and comparison with 2D-DLD

In previous work, we have shown that particles moving in *zigzag mode* have periodic trajectories. The periodicity of a trajectory is described by its average direction [p,q], where p, q are Miller indices. For example, in Figure 4.2b, the small circles represent a particle moving inside the obstacle array with periodicity [1,2]. Particles moving in *locked mode*, represented by the large circles in Figure 4.2b, move along a *column* obstacles in the array with periodicity [1,0]. (A column of obstacles is a series of obstacles aligned in the Z-direction, thus constituting a column in the array). In 2D-DLD, particles of all sizes were observed to transition from *locked mode* (periodicity [1,0]) to *zigzag mode* (with a different periodicity), as the forcing angle increases from $\alpha = 0°$.[140,183] The angle at which the transition occurs is defined as the critical angle α_c and, in principle, it is different for each type of particle.[183]

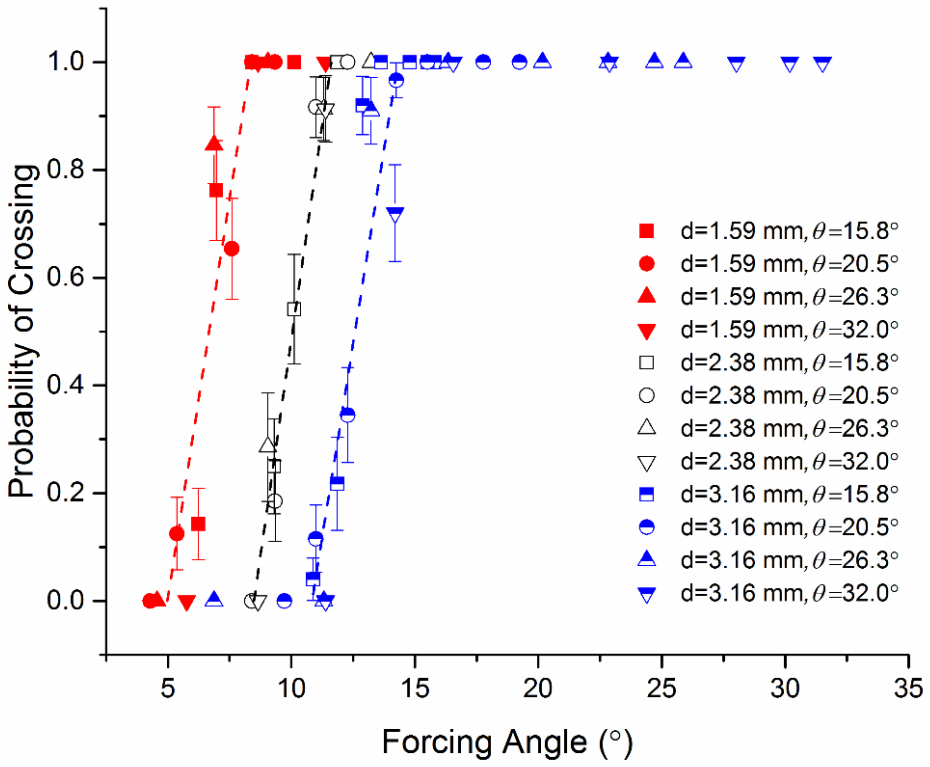

Figure 4.3: Probability of crossing as a function of the forcing angle. Different symbols correspond to different particle sizes and slope angles as indicated. Error bars represent standard deviation of the experimental data.

To investigate the presence of similar *locked-to-zigzag* transitions in the 3D-DLD system, we study the probability of crossing, P_c, defined as the fraction of a given size of particles that move in *zigzag mode* out of the total number of those particles in a given experiment. In Figure 4.3, we plot P_c as a function of the forcing angle for the different particles considered here. Consistent with 2D-DLD results, we observe sharp transitions in the crossing probability for all particle sizes. Another manifestation of these critical transitions is the presence of large variations in the migration angle when the forcing angle is close to

α_c, due to the discontinuous nature of the change in the migration angle, as indicated by the large error bars in the experimental data close to the transition. We estimate the critical angle α_c for each particle size as the forcing angle where its probability of crossing is equal to $1/2$, calculated using a linear fit of the intermediate P_c values (see Figure 4.3). For 1.59, 2.38, and 3.16 mm particles the estimated values of the critical angle are $6.7° \pm 1.7°$, $10.0° \pm 1.5°$ and $12.6° \pm 1.7°$, respectively. Also analogous to the 2D case, the critical angle increases with particle size, which enables size-based separation. In addition, we observe that for the same size of particles, the experimental results obtained with different tilt angles collapse into a single curve, which is consistent with the in-plane motion of the particles being independent of the out-of-plane motion. This is expected for the motion of a suspended particle past an array of posts at low Reynolds numbers, as long as particle-obstacle non-hydrodynamic interactions can be approximated by hard-core repulsion forces[176,177,185].

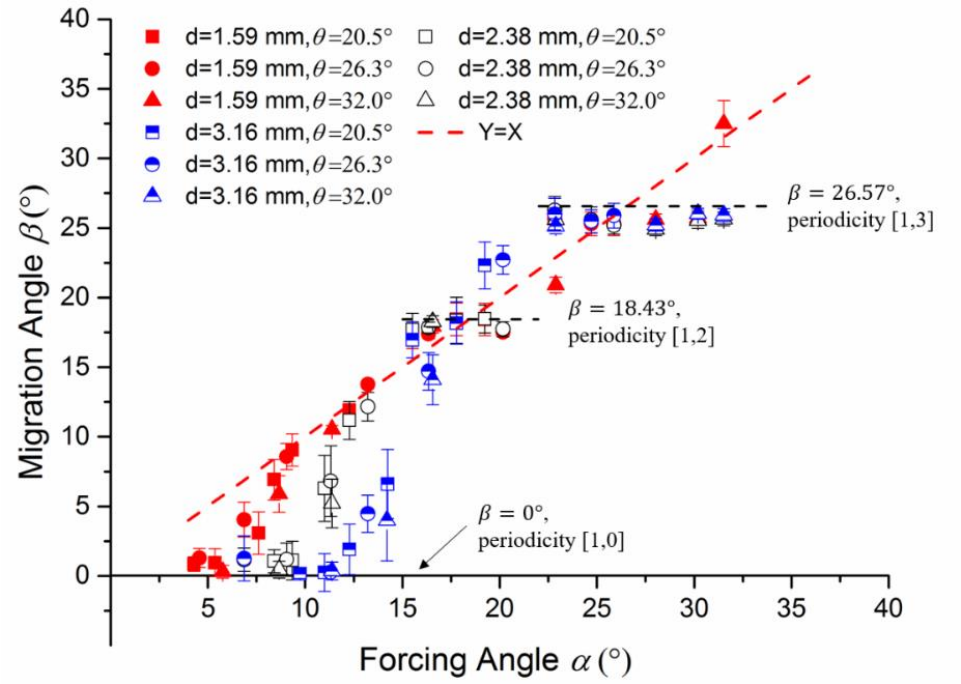

Figure 4.4: Migration angles as a function of forcing angle. Different symbols correspond to different particle sizes and slope angles as indicated. The dashed line represents $\beta = \alpha$. The migration angles corresponding to directions [1, 0], [1, 2] and [1, 3] are indicated. Error bars represent the standard deviation of the experimental data.

In Figure 4.4, we show the migration angle as a function of forcing angle for all the particles. As expected, for forcing angles smaller than the critical angle, the migration angle remains locked at $\beta = 0°$, i.e. particles are moving in *locked mode*. For forcing angles larger than the critical angle, particles migrate in *zigzag mode* with $\beta > 0°$. Again, we observe that the migration angle is independent of the tilt angle, which suggests that the in-plane motion of the particles is in fact independent from the out-of-plane dynamics. Figure 4.4 also shows that, when particles are moving in *zigzag mode*, their migration is not necessarily aligned with the driving force. In fact, Figure 4.4 shows clear 'plateaus' in the migration angle vs. forcing angle curves, indicating a constant migration angle for finite intervals of the forcing angle. This phenomenon, known as *directional locking*, is also present in the 2D case[186].

4.4.2 Migration model

As detailed in Chapter 2, Given b_c, and assuming that successive collisions are independent, the collision-based model predicts the migration angle at any forcing angle. Therefore, and in addition to the set of critical angles calculated from the crossing probability, we obtain a second estimate of the critical angle for each particle size by fitting the average migration angles with the proposed model (where b_c is the only fitting parameter). The results are plotted in Figure 4.5 where we observe good agreement between experiments and the proposed model, and the two sets of b_c values are reported in Table 4.1. We note that, due to the discontinuous and staircase-like nature of the curves, the fit of the experimental migration angles results in a range of critical offsets. We represent these ranges by the dashed lines in Figure 4.5b and Figure 4.5c. For 1.59 mm particles, however, the resulting range is smaller than our resolution and we do not include it in the plot. The corresponding uncertainty in the b_c values is also indicated in Table 4.1.

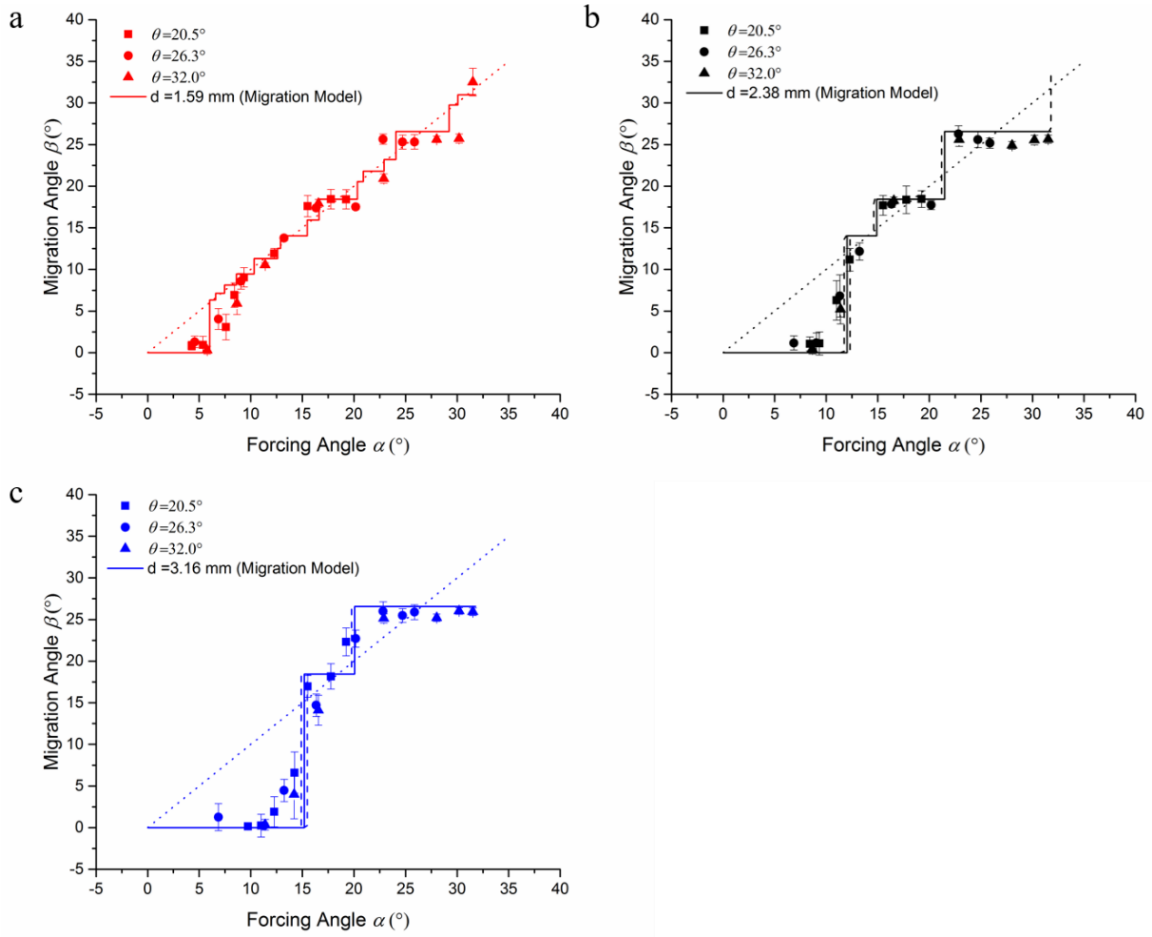

Figure 4.5 Migration angle as a function of forcing angle for (a) 1.59 mm particles, (b) 2.38 mm particles and (c) 3.16 mm particles. The solid line represents the best fit of the experimental results with the proposed model. The critical offset values obtained from the fit are reported in Table 4.1. The dashed lines indicate the uncertainty of the fitting parameter b_c in each plot. The error bars represent the standard deviation of the experimental data. The dotted straight line indicates $\beta = \alpha$ for reference.

Table 4.1 Critical offset obtained from the probability of crossing curves and from fitting the model to the experimental data

Particle Size d [mm]	b_c from P_c [mm]	b_c from model [mm]
1.59	0.70 ± 0.18	0.61
2.38	1.04 ± 0.15	1.24 ± 0.04
3.16	1.31 ± 0.17	1.57 ± 0.03

4.4.3 Three-dimensional deterministic lateral displacement (3D-DLD)

We consider the possible separative nature of the out-of-plane motion of the particles. In order to compare the motion of different particles, as well as its dependence on the forcing direction, we consider the out-of-plane displacement normalized by the in-plane displacement along the Z axis to obtain $\Delta y/\Delta z$. In Figure 4.6, we show the normalized out-of-plane displacement as a function of the in-plane forcing angle for all sizes of particles and for tilt angles θ= 20.5, 26.3 and 32.0°. As indicated in the plots, for all particle sizes, the normalized out-of-plane displacement peaks around their individual critical angles. This suggests that the particle in-plane motion significantly affects the out-of-plane displacement. When the in-plane forcing angle is close to its critical angle, particles tend to stay close to the obstacle longer, slowing down its in-plane-motion and resulting in a large out-of-plane displacement. As a result, we observe that for forcing angles $< 20°$, particles of different size can be separated by taking advantage of the differences in their out-of-plane displacement.

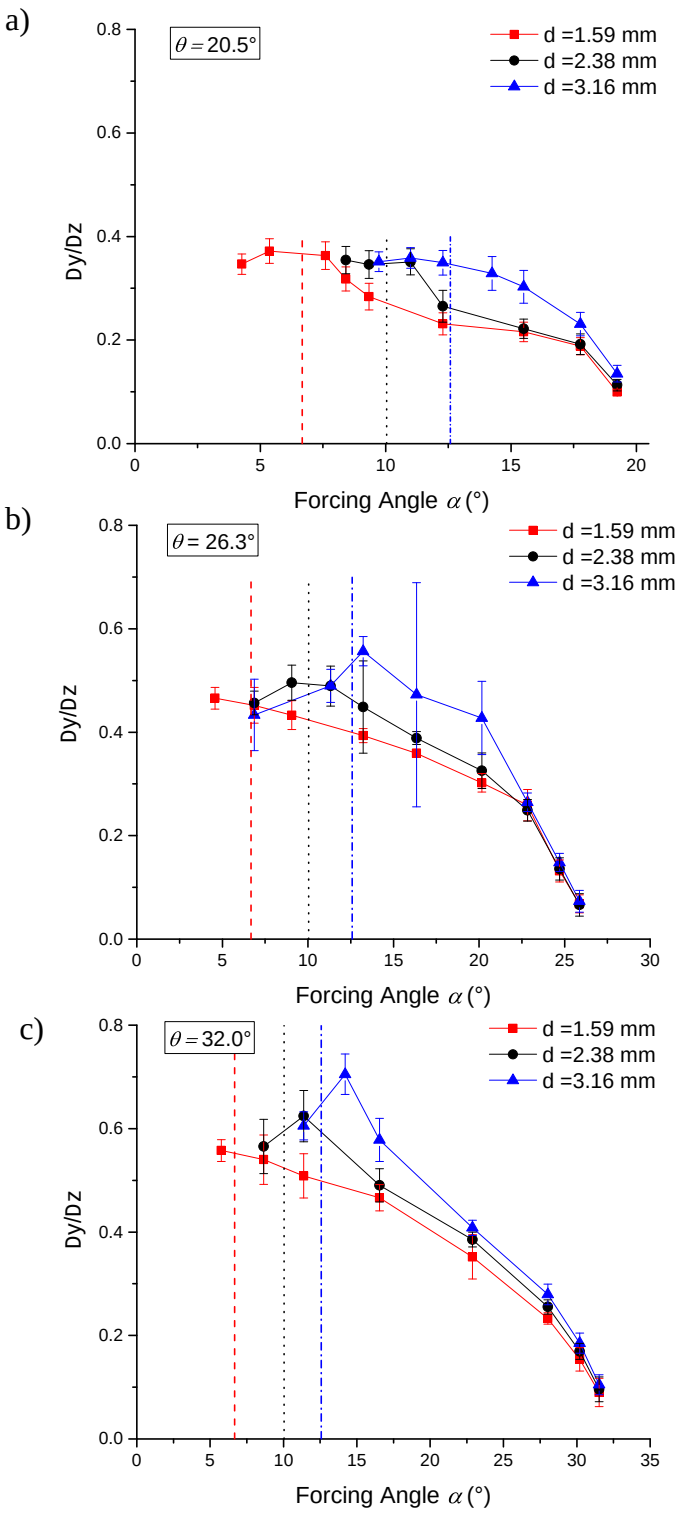

Figure 4.6 Normalized out-of-plane displacement as a funtion of the in-plane forcing angle for tilt angles (a) 20.5°, (b) 26.3° and (c) 32.0°. The dashed, dotted and dot dashed vertical lines in each plot represent the critical angles (obtained from the probability of crossing) for 1.59, 2.38 and 3.16 mm particles, respectively. The error bars represent the standard deviation of the experimental data.

Finally, we demonstrate the simultaneous fractionation of all three sizes of particles by harnessing the out-of-plane separative displacement discussed above. To this end, we consider a forcing angle $\alpha \cong 12°$. According to Figure 4.3, with this forcing angle, the 3.16 mm particles migrate in *locked mode*, while the 2.38 and 1.59 mm particles migrate in *zigzag* mode. This results in the in-plane separation of the largest particles from the rest. On the other hand, the 2.38 and 1.59 mm particles could not be separated based on the in-plane motion alone. This is, in fact, a typical situation in 2D-DLD systems, and usually limits the separation that can be performed to the binary fractionation of a complex suspension into two streams. On the other hand, Figure 4.6b, for example, shows that 1.59 and 2.38 mm particles would have a significant difference in their out-of-plane displacement, which enables their fractionation. In order to demonstrate the advantages of 3D-DLD we have also quantified the quality of this test separation. To this end, we added a collector at the bottom of our experimental setup (see Figure 4.7). The collector is partitioned into three sections, based on our previous experiments, with an in-plane separation board, perpendicular to X, which would separate the 3.16 mm particles from the rest, and an out-of-plane separation board, perpendicular to Y, that separated between the 1.59 and 2.38 mm particles. The location of the out-of-plane board is determined with respect to the entrance point of the particles and indicated by l_1 in Figure 4.7. The results are provided in terms of $n_{\alpha\beta}$ the number of particles of type α in the collection bin designed to capture particles of type β. We can then define the *efficiency* of the separation of particles of a given type as the fraction of such particles in the corresponding collection bin, $e_\alpha = n_{\alpha\alpha} / \sum_\beta n_{\alpha\beta}$, and the *purity* of the separation of particles of a given type as the

fraction of particles of this type out of the total number of particles in the corresponding bin, $p_\alpha = n_{\alpha\alpha} / \sum_\beta n_{\beta\alpha}$.

We first perform experiments by releasing one particle at a time into the device, in order to avoid particle-particle interactions and the results are presented in Table 4.2. We obtain excellent separation results, with efficiencies ≥ 95% and purities ≥ 89%. Then, in order to increase the throughput of the separation, we performed exploratory experiments introducing a mixture of 3-6 particles of different sizes at the same time and the results are presented in Table 3. Although both efficiency and purity values are still reasonably good, a clear reduction is observed, which suggests that further experiments are needed to investigate throughput limitations of the proposed system.

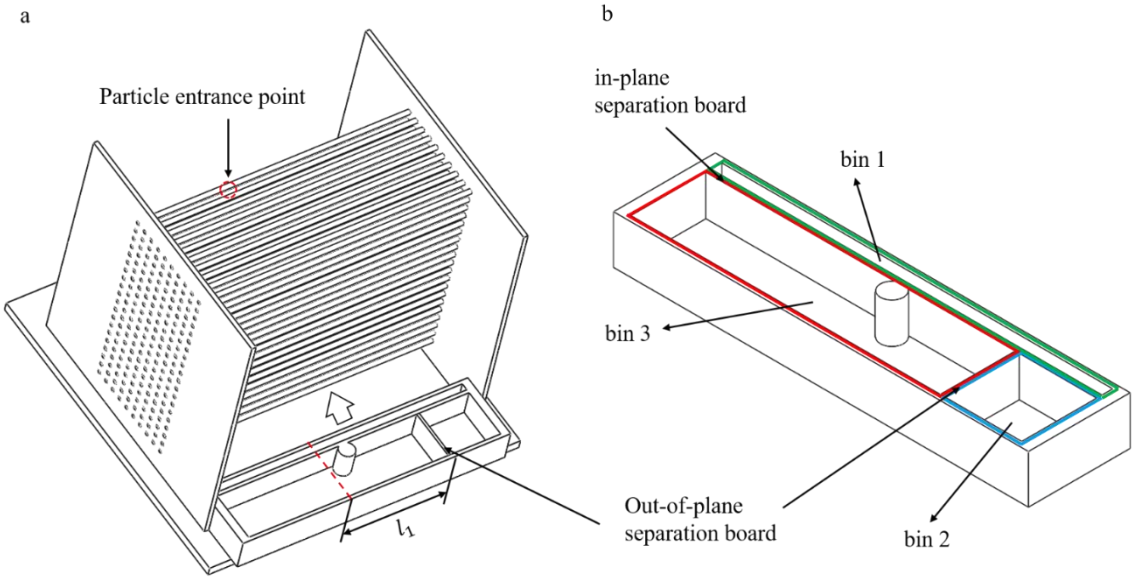

Figure 4.7 Schematic view for the placement of the particle collector. Bin 1,2 and 3 are designed to collect 3.16, 2.38 and 1.59 mm particles, respectively.

Table 4.2 Separation results in the absence of particle-particle interactions.

Particle Size / Bin Number	1.59 mm	2.38 mm	3.16 mm	Purity
1	1	1	17	89%
2	0	21	0	100%
3	24	0	0	100%
Efficiency	96%	95%	100%	

Table 4.3 Separation results in the presence particle-particle interactions.

Particle size / Bin number	1.59 mm	2.38 mm	3.16 mm	Purity
1	0	1	17	94%
2	5	22	0	82%
3	18	2	0	90%
Efficiency	78%	88%	100%	

4.5 Conclusions

We present a simple concept to enhance separation in DLD systems, based on extending the traditionally 2D method into the third dimension by using an array of long cylindrical posts. First, we demonstrated that when projected onto the basal plane of the array, the particles in-plane migration patterns are analogous to those present in the force-driven 2D-DLD case. We observed the existence of a *locked mode* when the forcing angle is relatively small, and a sharp transition into *zigzag mode* when the forcing angle is increased past a critical value (critical angle). The fact that the critical angle depends on particle size enables the in-plane fractionation. We also observed that the particles in-plane trajectories are independent of the out-of-plane motion. More important for separation, we observed that

the particle out-of-plane displacement does depend on the in-plane motion, with the largest displacements for each type of particle observed when the forcing angle is close to the corresponding critical value. Therefore, the differences in critical angle with particle size not only enable in-plane separation but also lead to different out-of-plane displacements that can be harnessed to enhance the separation ability of DLD systems. Based on such observation, we then demonstrated that a polydisperse suspension containing three different sizes of particles can be fractionated into its individual components using the proposed 3D-DLD system, with excellent efficiency and purity. Finally, we note that increasing separation throughput lead to a reduction in separation quality and further experiments are needed to explore the effect of particle-particle interactions in the proposed 3D-DLD system.

5 Liquid-based stationary phase for deterministic lateral displacement separation

5.1 Introduction

Despite the various modifications investigated in the DLD systems, the type of stationary phases investigated so far have consisted exclusively of arrays of solid pillars. In contrast, here we demonstrate the use of liquid-bridges, arranged in a periodic array, as an alternative stationary phase to create a new type of DLD systems (see Figure 5.1a-c). The proposed type of DLD systems opens a number of possibilities for future developments, with potential advantages including alternative fabrication methods, clogging reduction and/or remediation, and on-line control of the obstacle size. We shall also discuss the possible use

of analogous liquid-based DLD systems in closely related applications, such as filtration and detection system.

5.2 Experimental setup and materials

In the experiments, we used two immiscible liquids, one serves as a continuum phase through which particles sediment, and the other liquid is used to create the array of anchored liquid-bridges, that is, the stationary phase through which particles move as they sediment. Figure 5.1a-c shows the fabrication of the stationary phase (water drops first and water liquid-bridges after contact with the top plate) and Figure 5.1d shows the array of liquid-bridges submerged in the continuum phase liquid (vegetable oil). We performed the experiments using a scaled-up version of typical DLD microdevices. In order to obtain relatively low Reynolds and Stokes numbers, comparable to those usually found in microfluidic applications, we choose oil as the continuum phase in the system, with viscosity $\mu = 52.3$ mPa $\cdot$ s and density $\rho_f = 0.926$ g/cm^3. The sizes of the particles used in the experiments are $a = 0.79$ and 1 mm, obtained from Mcmaster-Carr and Precision Plastic Ball Co., respectively. The materials and corresponding densities of the particles used are listed in Table 5.1. In Table 5.1 we also list the particle Reynolds and Stokes numbers estimated from the predicted sedimentation velocity of the particles in bulk oil. We note that for the larger particles with higher density, the Reynolds numbers are $\mathcal{O}(1)$, and inertia effects would be present. This also leads to potential differences in the deformation experienced by the anchored liquid-bridges creating the array depending on the size and density of particle. Water drops are used to create the array of liquid-bridges.

Then, in order to evaluate the potential deformation of the bridges, we estimate the corresponding capillary number (see Table 5.1; the water-oil interfacial tension is approximately 23 mN/m). Note that, when scaled back to microenvironments, it is expected that not all the non-dimensional numbers can be matched exactly. Particularly in our case, the typical Ca in microdevices would be smaller than the largest values observed in the scaled-up system. As a result, some of the observations made in the current system for relatively large values of the capillary number may not be present in a microdevice, depending on the strength of the field (which affects the particle velocity), viscosity of the continuum phase and the interfacial tension between the stationary phase and the continuum phase. On the other hand, the main observations demonstrating size-based separation using arrays of anchored liquid-bridges take place over the entire range of Ca and should therefore be also present at the microscale.

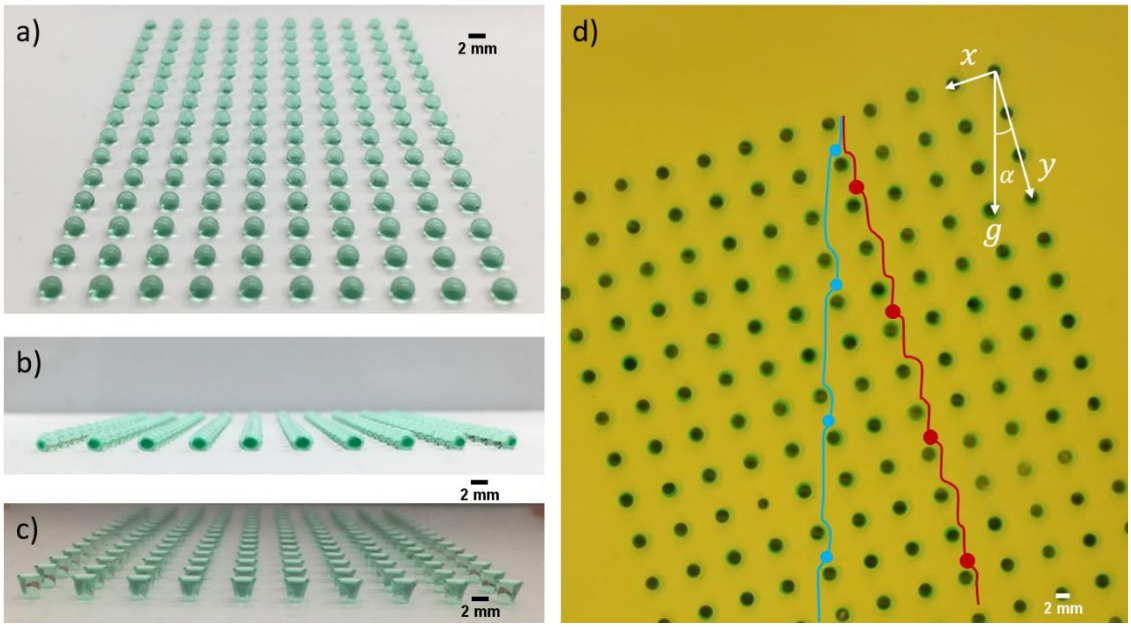

Figure 5.1 Isometric views of the anchored liquid array without (a,b) and with (c) the top plate. d) A view of the set-up showing the trajectory of 0.79 mm and 1 mm particles when forcing angle $\alpha = 17°$. The large and small solid circles drawn in the picture represent intermediate positions of the particles as they move

To form the lattice of anchored liquid-bridges, we first create an array of wells on a coated polypropylene plate. The spacing between two neighboring wells is l = 6 mm and the radius of the anchoring wells is $D/2 = 0.89$ mm. Then, we deposit water droplets of uniform volume $V = 20$ µl into each well using a syringe pump. Figure 5.1a-b shows the deposited droplet array from two different views. Before depositing the water droplets, the plate is painted to make its surface hydrophobic (Rust-Oleum NeverWet). Using a hydrophobic coating is key to confine the water droplets to the anchoring wells. To create the liquid-bridges, an acrylic plate is then placed on top of the array of droplets maintaining a gap distance $h = 2.3$ mm (see Figure 5.1c). Clearly, this method is only practical for the scaled-up version used in the experiments reported here and not at the actual scale of microdevices. On the other hand, successful methods to generate two dimensional arrays

of droplets in microfluidics have been reported in the literature for other purposes,[187–190] and would serve as a promising starting point to fabricate the proposed anchored arrays of liquid-bridges in future work.

Table 5.1 Particle properties along with corresponding particle Reynolds number, Stokes number and Capillary number

Particle radius a (mm)	**Material**	**Particle density ρ_p (g/cm^3)**	**Particle settling velocity (cm/s)**	**Reynolds number Re**	**Stokes number St**	**Capillary number Ca**
0.79	Nylon	1.140	0.556	0.156	0.021	0.013
0.79	Acrylic	1.185	0.673	0.188	0.027	0.015
0.79	Delrin	1.410	1.258	0.352	0.060	0.029
0.79	PTFE	2.200	3.311	0.927	0.245	0.075
1	Nylon	1.140	0.891	0.316	0.043	0.020
1	Acrylic	1.185	1.078	0.382	0.054	0.025
1	Delrin	1.410	2.015	0.714	0.121	0.046
1	PTFE	2.200	5.305	1.880	0.496	0.121
1	Glass	2.500	6.554	2.323	0.697	0.149

As shown in Figure 5.1d, we define the angle between the driving force (gravity), and one of the main directions of the array (y axis) as the forcing angle α (see Figure 5.1d). The migration angle β is defined as the angle between the particle migration direction (on average) and the *y*-axis (see Figure 5.1d). Both definitions are completely analogous to those used in previous work in traditional DLD systems. For each particle size and material, we vary the forcing angle continuously, within the range between 9°-23°, and track the trajectories followed by the particles using image analysis. For each case (forcing angle;

particle size; particle material), we use 20-25 particles and the migration angle is taken as the average migration angle of all the particles used.

5.3 Results and discussion

We observe the same migration behavior as a function of forcing angle for all the different particles considered here, independent of size and material. First, at small forcing angles, particles move along a *lane* in the array, in the lattice direction [1,0] (along the *y-axis*). Particles are *locked* to move in this direction, which we refer to as the *principal locked mode*, for all forcing angle smaller than a critical value (see the trajectory of large particles in Figure 5.1d). Then, for forcing angles larger than the critical angle, particles are able to move across *lanes* in the array and migrate in *zigzag mode* (see the trajectory of small particles in Figure 5.1d). In both migration modes, the motion of the particles is periodic and the migration angle therefore corresponds to a lattice direction. In Figure 5.1d, we present the zigzag motion of a small particle migrating in the [1,3] lattice direction. The fact that the transition from locked to zigzag mode happens at an angle that depends on particle size is what enables size-based separation. For example, the forcing angle in Figure 5.1d, $\alpha = 17°$, is smaller than the critical angle for the large particles ($a = 1\text{mm}$), but larger than the critical angle for the small particles ($a = 0.79\text{mm}$). As a result, particles migrate in different directions (*vector chromatography*) and can be continuously fractionated. Interestingly, the migration phenomena described above is completely analogous to that observed in previous work using arrays of solid pillars.

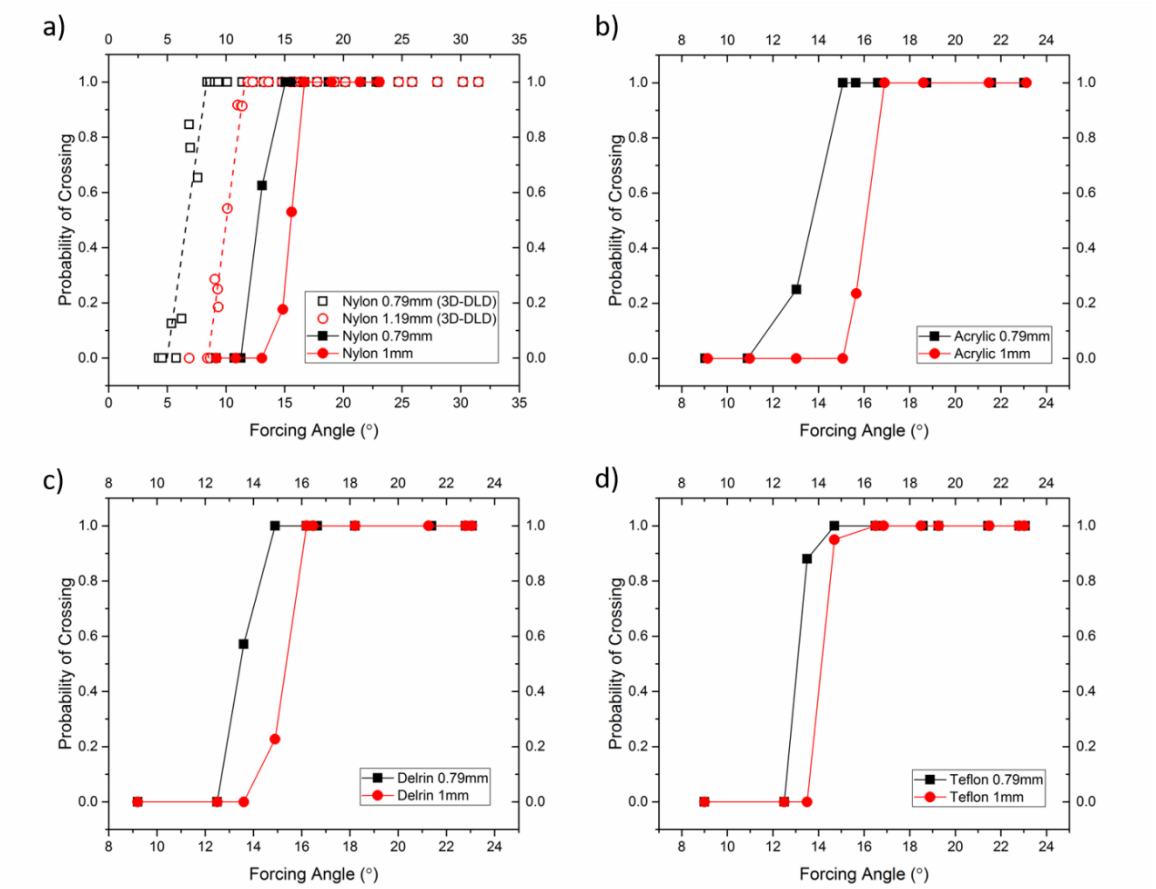

Figure 5.2 Probability of crossing as a function of forcing angle for Nylon, Acrylic, Delrin and PTFE particles with density $\rho_p = 1.14, 1.185, 1.410$ and 2.2 g/cm^3 respectively.

In order to quantitatively characterize the transition from locked to zigzag mode for different particles, for each forcing angle we measure the probability that a given particle would cross lanes in the device, P_c. For each particle size and material, and a given forcing angle, the crossing probability P_c is calculated as the fraction of the particles tracked that move in zigzag mode inside the lattice. By definition, $P_c = 0$ represents a situation in which all the particles of a given type move in the *principal locked mode*, while $P_c = 1$ for a given forcing angle corresponds to all the particles under consideration moving in *zigzag mode* for that forcing angle. Intermediate values of the probability of crossing occur when

some of the particles are locked and some move in zigzag. We also define the critical angle, α_c, for the transition between the two migration modes, as the forcing angle when $P_c = 1/2$.

In Figure 5.2, we plot the probability of crossing lanes as a function of forcing angle. We observe that, for particles of the same material, the critical angle increases with particle size, which enables size-based separation. An example of this observation was presented in Figure 5.1d and discussed above. Analogous behavior was observed in previous studies using solid arrays of posts. Therefore, it is clear that the anchored-liquid DLD system enables size-based separation of particles. Moreover, the relatively sharp transition observed between the two migration modes, indicates that good separation resolution and purity are possible in anchored-liquid DLD.

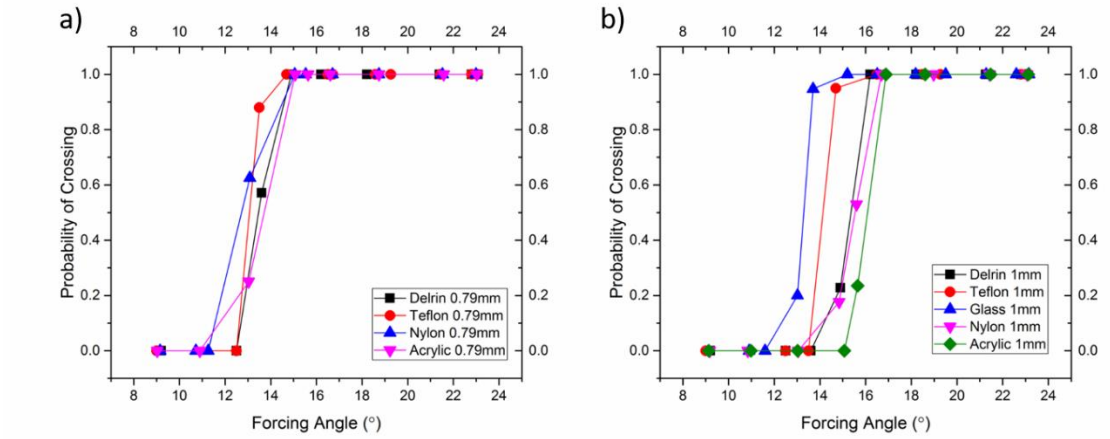

Figure 5.3 Probability of crossing as a function of forcing angle. 0.79 mm (a) and 1 mm (b) Nylon, Acrylic, Delrin and PTFE particles with density $\rho_p = 1.14, 1.185, 1.410$ and 2.2 g/cm^3 respectively. For 1 mm size we also present results for glass particles, $\rho_p = 2.5$ g/cm^3.

In Figure 5.3, we combine the probability of crossing obtained for different materials but for a given size of particles. Clearly, there is no measurable difference in the critical angle obtained for different materials in the case of small particles, and all curves practically collapse into a single universal behavior. The same is true for the larger particles and materials with relatively low densities. However, for particles with larger densities (PTFE and Glass particles), we observe a significant decrease in the critical angle. This could enable density-based separation of particles. For example, setting a forcing angle $\alpha \approx 14°$ would fractionate a mixture of all large particles into two groups, separating PTFE and glass particles, which would zigzag through the array, from the less dense ones, that would be locked in the [1,0] direction. In previous work, we have presented analogous results in traditional DLD devices using solid obstacles.[191] However, in the case of solid obstacles the range of Stokes numbers where inertia effects were observed in the critical angle was significantly larger. An important difference is that, in the present study of liquid-based DLD, both the Stokes and capillary numbers increase at the same time, indicating that liquid-bridge deformation could play an important role. In fact, we do observe significant deformation of the liquid-bridges when glass particles move past them. In Figure 5.4, we present a series of snapshots of a large glass particle, moving past a liquid-bridge. As a result of the deformation of the liquid-bridges, the particles experience a smaller irreversible lateral displacement leading to a smaller critical angle, as shown in Figure 5.3. Further studies, however, would be required to assess the effect of deformation on particle trajectories depending on capillary and Stokes numbers.

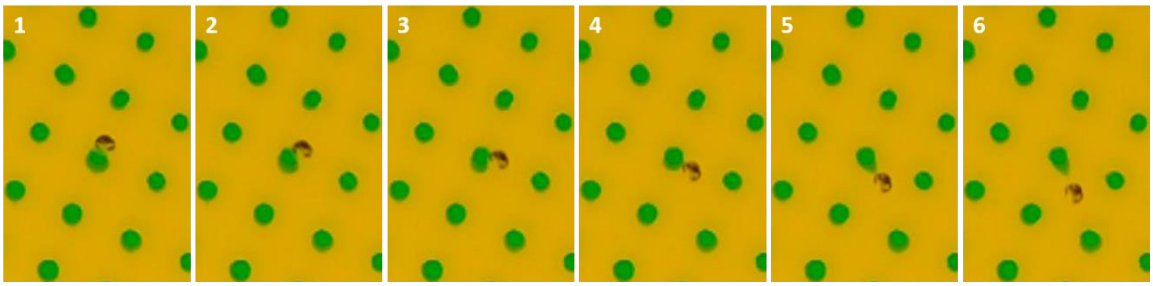

Figure 5.4 Deformation of a liquid post as 2mm glass particles moves past it (the particle was colored to improve the contrast). The pictures are taken with a time interval of 0.08 s.

As we mentioned, differences in the critical angle between species enable separation. However, the quality of the separation also depends on the differences in the migration angle underlying *vector chromatography*. In previous studies using traditional solid arrays, the particles are observed to transition from the [1,0] direction (*principal locking mode;* $\beta = 0°$), to a larger migration angle, typically in the [1,3] ($\beta = 18.4°$) or [1,2] ($\beta = 26.6°$) directions in the array, leading to a significant difference in the migration angles and excellent separation quality. In Figure 5.5, we plot the average migration angle of each type of particle as a function of the forcing angle. As discussed before, all particles migrate in the principal locking mode at small forcing angle and transition into zigzag mode when they reach the critical angle. These first critical transitions are relatively sharp, indicating the possibility of good separation resolution. It is clear from Figure 5.5a-c, that excellent size separation between small and large particles is possible for Nylon, Acrylic and Delrin particles, due to a significant difference in the migration angle. Specifically, if we set a forcing angle just below the critical angle of the large particles (e. g. $\alpha \approx 15°$ for all three particle types), we observe that the difference in migration angle between large and small particles would be $\Delta\beta \geq 10°$ in all cases. On the other hand, due to the inertia and capillary

effects discussed before, the large and small PTFE particles migrate at similar angles, as shown in Figure 5.5d. This would make it difficult to fractionate them by size. On the other hand, if this effect is preserved at microscales, it would enable inertia-based separation.

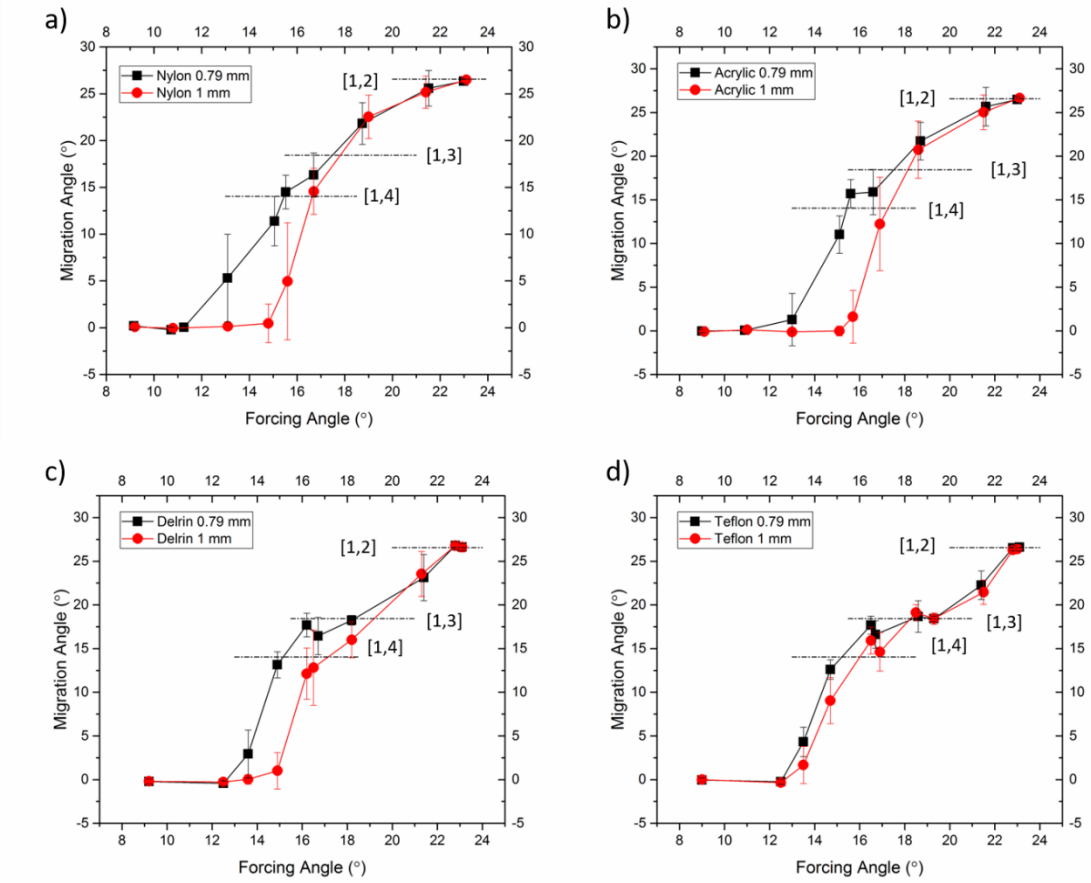

Figure 5.5 Average migration angle as a function of forcing angle for Nylon, Acrylic, Delrin and PTFE particles with density $\rho_p = 1.14, 1.185, 1.410$ and 2.2 g/cm^3 respectively.

Another common feature in traditional DLD using solid obstacles is the presence of *directional locking* at all forcing angles.[136–138] Directional locking means that particles move at fixed lattice directions over a finite range of forcing angles, which is thus

characterized by *plateaus* in the migration angle when plotted as a function of the forcing angle (see dot-dashed lines in Figure 5.5). It also means that only a few set migration angles are observed, and all different particle types are locked to move in those lattice directions, with lattice directions [1,4], [1,3] and [1,2] among the most common. Unfortunately, this phenomenon limits the separation of a mixture, typically to a fractionation into two distinct groups, each migrating into one of the possible lattice directions. In the case of liquid-based DLD studied here, however, we do not observe strong directional locking except for the *principal locking mode* in the [1,0] direction. This is consistent with numerical results obtained in the case of suspended particles moving through an array of *soft obstacles* (parabolic repulsive centers).[192] Specifically, the principal locking mode ends in a tangent bifurcation at the critical forcing and a large number of migration angles is possible at larger forcing angles.[192] This, therefore, presents a clear opportunity for a higher *peak capacity* in the proposed liquid-based DLD method compared to traditional DLD, in that more intermediate migration angles could be observed simultaneously. Specifically, particles of different density could be separated by selecting a forcing angle in the transition region, as shown in Figure 5.6. For a forcing angle $\alpha \approx 15°$ we observe that particles transition from the principal locked mode, [1,0], at low Stokes numbers (small densities) to a migration angle $\beta \approx 14°$, corresponding to the [1,4] direction, at large Stokes numbers (large densities). On the other hand, smaller and larger forcing angles exhibit a significantly smaller change with the density of the particles.

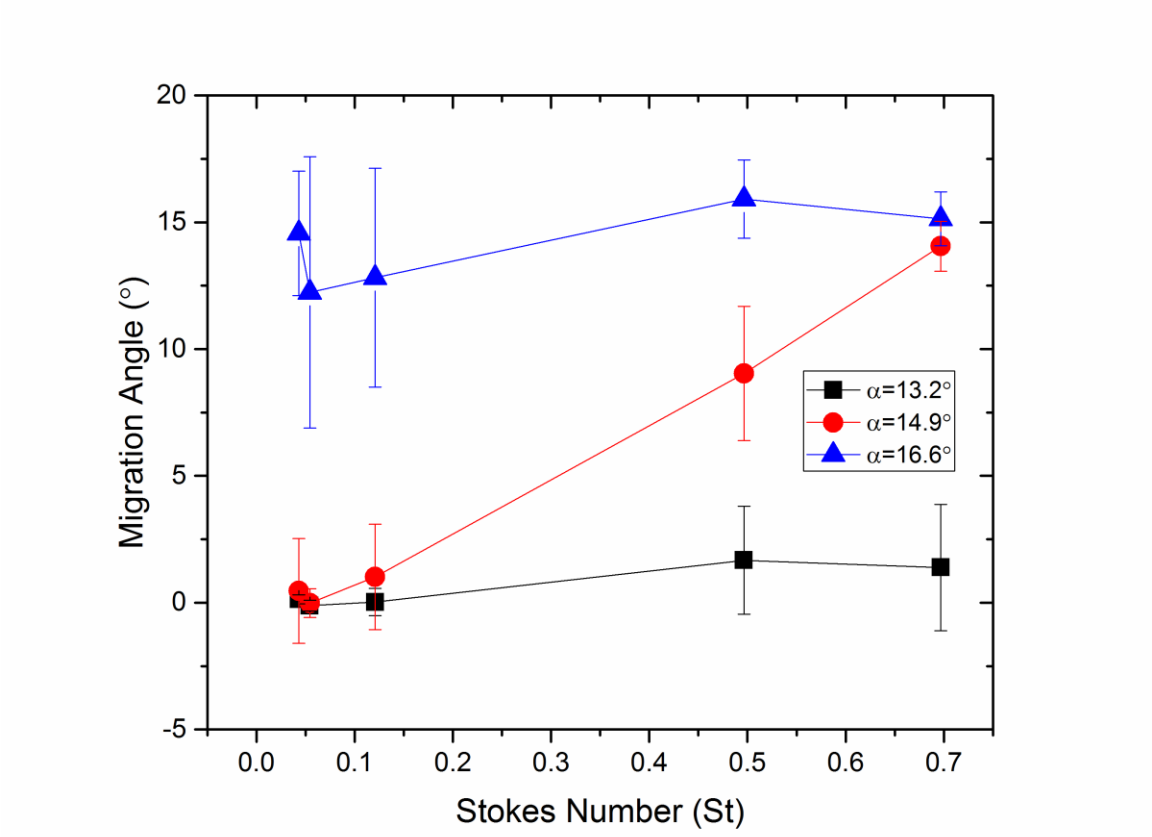

Figure 5.6 Migration angle for particles of the same size (a = 1mm) but different density (Nylon, Acrylic, Delrin, PTFE and glass) as a function of the nominal Stokes Number. The three curves correspond to different forcing angles as indicated.

5.4 Conclusion

We have demonstrated a novel DLD system in which the traditional array of solid pillars is replaced by an array of anchored liquid-bridges. We showed that at low Stokes and Capillary numbers the proposed system works similarly to the solid case, enabling excellent separation. In fact, particles with a size difference of 20% could be easily separated. In addition, we observed that at larger Stokes numbers particles could be separated based on density. This is a probably a combination of inertia and capillary effects,

as we observed significant deformation of the liquid-bridges in this case. This suggests that working at similar capillary numbers at the microscale could enable alternative ways to separate particles beyond differences in size.

The proposed used of liquid-based stationary phases in DLD could lead to a new family of DLD devices with distinct features. In some cases, arrays of anchored liquid bridges might be simpler to fabricate than their solid counterpart, as an array of wells can be easily created compared to an array of extruded obstacles, possibly reducing the number of fabrication steps. The liquid-based systems could also alleviate clogging issues that exist in traditional DLD systems. Moreover, the systems could possibly be renewable, by flushing and regenerating the liquid-bridges. One could even envision creating an array of holes in the bottom plate that connect to a reservoir of the stationary-phase liquid, which could provide not only rapid renovation of the array of liquid-bridges, but also provide additional features, such as a dynamic control of the obstacle size by changing the pressure in the reservoir. We also note that using a liquid-base stationary-phase could be a valuable innovation not only in DLD systems but in a number of microfluidic separation methods that currently use a solid stationary phase.

6 Summary and conclusions on deterministic lateral displacement systems

6.1 Comparison with previous work

Deterministic lateral displacement, as an attractive separation scheme within the scope of microfluidics, has generated a great scientific interest from researchers all over the world. Over the last decade, numerous modifications including different post shapes, and various driving fields have been proposed in order to improve the separation ability of DLD systems. In this thesis, we further modify the system by: i) implementing a rotating circular disk in the flow driven DLD device; ii) extending the traditionally 2D problem into the third dimension; iii) and innovatively changing the material of the stationary phase from

solid to liquid. Considering the amount of experimental data gathered in the projects presented in this thesis and our previous work, here, we provide a summary on the critical behavior of particles inside DLD arrays. The purpose of the summary is not only to put our experimental results into the general context of DLD research, but to identify the correlation between the particle critical angle and its nondimensionalized radius, a/G. There are several objectives associated with determining the correlations between the particle critical angle and its nondimensionalized radius. Given that there exists a cubic relation between $\tan\alpha_c$ and the nondimensionalized particle size, we will be able to evaluate the applicability of streamline-based model under different experimental settings, force driven DLD systems in particular. As mentioned in the introduction section, one of the drawbacks of the collision-based model lies in its inability to predict the particle critical angle before experiments. Specifically, the critical offset b_c that allows you to calculate the migration angle of a particle given its size at any forcing angle, has to be determined through preliminary experiments. As a result, by studying the relation between particle critical offset and the nondimensionalized radius of the particle, we hope to obtain some insight on how we can predict the behavior of particles of certain size inside the obstacle array. In our summary, we are unfortunately not able to carry out an exhaustive research on all the DLD experiments due to the sheer amount of data that exists. Instead, we will focus mainly on the data obtained by our group in various experimental settings.

We provide a detailed list of the research papers considered in this summary in Table 6.1. In the "Type" column, g-DLD represents gravity driven DLD systems, flow-DLD represents flow driven systems and e-DLD represents electrical force driven DLD systems. The "Design" column specifies the design details of the individual DLD system.

Specifically, SL and FA is short for single line and full array. Two letters following SL or FA represents the stationary phase and particle property with S short for solid state and L short for liquid state. All the dimension parameters share the same scale as specified in the "Scale" column. More experimental details can be found in the reference paper listed in the "Ref" column.

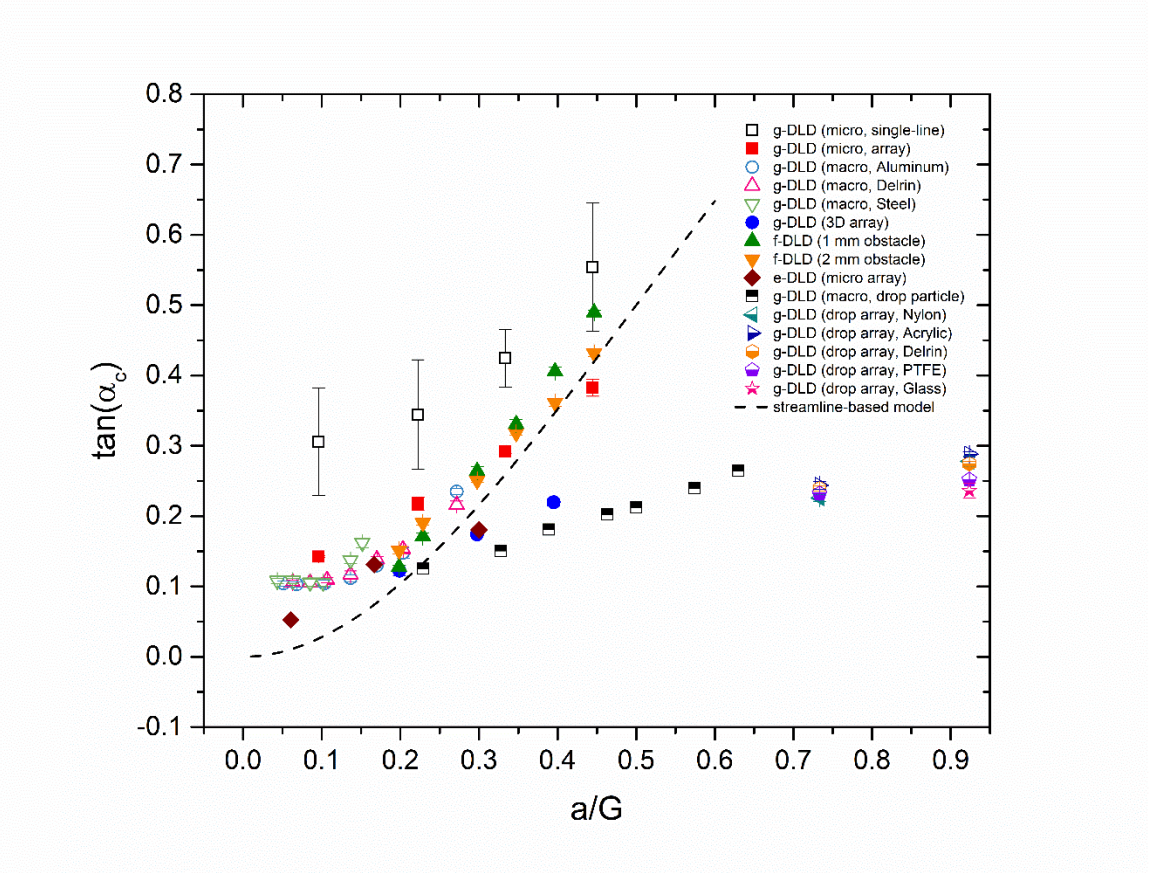

Figure 6.1 Comparison of selected DLD results. The open symbols represent the results collected from single line experiments. Specifically, in those experiments, instead of a full array, only a single line of obstacle is used (full paper see ref 141 and ref 143). Half open symbols represent experimental results obtained with deformable component (see ref 2 and ref 3). Solid symbols illustrate results obtained in solid full DLD array (see ref 1,140,142,177). The dashed line is the calculation result from streamline-based model.

Table 6.1 Details of the DLD systems that are included in Figure 6.1.

Scale	Type	Design	Particle diameter *d*	Obstacle diameter	Obstacle spacing *l*	Ref
μm	g-DLD	SL, S, S	4.32, 10, 15 and 20	19.5	40	193
μm	g-DLD	FA, S, S	4.32, 10, 15 and 20	17.5	40	140
mm	g-DLD	SL, S, S	1.0~12.3	15.8	7.8~24.2	191
mm	g-DLD	FA, S, S	1.59, 2.38 and 3.16	2	6	2
mm	flow-DLD	FA, S, S	1.59~3.57	1 or 2	5 or 6	1
μm	e-DLD	FA, S, S	4.32, 10 and 15	19	40	142
mm	g-DLD	SL, S, L	1.5~6	7.8	16	194
mm	g-DLD	FA, L, S	1.59 and 2	1.78	6	144

As shown in Figure 6.1, we see that there seems to be two distinct patterns in the critical angle vs. nondimensionalized particle radius plot for flow driven and force driven DLD case. Specifically, for the flow-driven reconfigurable DLD experiments, the streamline-based model predicts the critical angle accurately. Note that for electrical force driven case, since the force is applied on the surface of the particles, it is expected and validated in Figure 6.1 that they will follow the migration pattern in the flow driven DLD cases more closely. In contrast, for gravity driven DLD cases with full macroscale arrays, particle critical angle is observed to be linearly increasing with the nondimensionalized particle radius. Interestingly, for g-DLD systems with deformable component, either drop particle or liquid stationary phase, the relation between critical angle and nondimensionalized particle radius seems to be following the same trend as that in the solid DLD cases. The micro scale g-DLD experiments however, deviate from the general linear trend observed in the macro scale setup. Since there is no flow in the force driven DLD systems, the streamlinebased model, as expected, is not able to predict the critical angle for particles of any given size. For g-DLD systems with only a single line of obstacles as stationary phase,

however, since the gap G is hard to define (in Figure 6.1, G is taken as $l - d$), we do not see a general trend in the critical angle vs. nordimensionalized particle radius plot.

6.2 Conclusions on DLD

We have introduced three extensions on the traditional DLD device in our work, including reconfigurable DLD, 3D-DLD and DLD with anchored-liquid arrays. In all systems, we demonstrated the existence of a *locked mode* for all the different particles considered. In this *locked mode,* corresponding to small forcing angles, the migration angle of the particles remains β=0° until a sudden transition into *zigzag mode* occurs when the forcing angle reaches a critical transition angle. The fact that the transition occurs at increasing forcing angles for larger particles enables particle separation.

In the reconfigurable macromodel setting, in fact, we observed a linear trend for the critical angle as a function of particle size. Although streamline-based model predicts a cubic relation between particle critical angle and its nordimensionalized radius, as shown in Figure 6.1, the predicted values are actually very similar to the experimental values. We then showed that the collision-based model, not only captures the sharp *locked-to-zigzag mode* transitions, but also predicts the migration angles at larger forcing angles.

We then present a simple concept to enhance separation in DLD systems, based on extending the traditionally 2D method into the third dimension by using an array of long cylindrical posts. First, we demonstrated that when projected onto the basal plane of the array, the particles in-plane migration patterns are analogous to those present in the force-driven 2D-DLD case where particle size separation is observed. More importantly, we observed that the particle out-of-plane displacement depends on the in-plane motion, with

the largest displacements for each type of particle observed at its corresponding critical angle. Therefore, the differences in critical angle with particle size not only enable in-plane separation but also lead to different out-of-plane displacements that can be harnessed to enhance the separation ability of DLD systems.

Lastly, we have demonstrated a novel DLD system in which the traditional array of solid pillars is replaced by an array of anchored liquid-bridges. We showed that at low Stokes and capillary numbers the proposed system works similarly to the solid case, enabling excellent separation. In addition, we observed that at larger Stokes numbers particles could be separated based on density. This is a probably a combination of inertia and capillary effects, as we observed significant deformation of the liquid-bridges in this case. This suggests that working at similar capillary numbers at the microscale could enable alternative ways to separate particles beyond differences in size.

Note that, although we did not show any modeling effort in Figure 6.1, the collision-based model is applicable in most force driven and flow driven DLD systems. However, for trials with high Stokes number and Capillary number in liquid-DLD systems, the collision-based model will not be applicable possibly due to particle inertia and the deformation of the obstacles. If the linear trend in the force driven DLD systems is further validated, we can then predict the particle trajectory under any given forcing angle without any preliminary trials. For the flow driven cases however, it has been repeatedly proven that the streamline-based model is applicable and can rather accurately predict the critical angle of particles of any given size. As a result, a combination of both models can serve as an excellent guidance for the design of the stationary phase in a DLD system.

7 Air filtration with single water bridge

7.1 Introduction

The effort to understand particulate matter air pollution can be traced back to as early as the London smog incident, December 1952. Although it has been well established that particulate matter in air will induce adverse health effects, the mechanisms of these effects are still for the most part unclear. Two of the most well studied areas on this topic focus on identifying the effect of particle chemical composition or particle size on the toxicity of particulate pollution. As Harrison *et al.* concludes in their comprehensive review, however, the experimental data reported in the literature provides little support for the assumption that single major or minor component of the particulate matter is responsible for the adverse health effect.[195] In addition, they remained equivocal in terms of the health effect that particle size has on the health of human body due to the sparsity of the data. One of

the key points they mentioned is that although the majority of the research have used particles of diameter within the range from 2.5 to 10 μm, which is typically referred to as PM_{10}, the fine particulate matter with diameter smaller than 2.5 μm, typically referred to as $PM_{2.5}$, is believed to be the main component that contributes to the adverse health effect of particulate matter air pollution. Although conclusively demonstrating the association between $PM_{2.5}$ exposure and various adverse health effects are "real" and "causal" has been proven challenging, numerous pathways have been hypothesized to link the varying degree of exposure to $PM_{2.5}$ to various adverse health effects.[196] Explicitly, it has been hypothesized and extensively studied that long-term or chronic $PM_{2.5}$ exposure could lead to more rapid progression of chronic obtrusive pulmonary disease and that acute $PM_{2.5}$ exposure will exacerbate existing pulmonary conditions.[197,198] There is also evidence that PM-induced pulmonary inflammations can have an effect on vasculature alterations.[199,200] Additionally, PM exposure has been linked to adverse effects in cardiac autonomic function by numerous studies[201–203], and is substantially proven to result in modulated host defenses and immunity.[204,205]

Public awareness of PM exposure has been heightened during recent years due to extensive news reports on air quality problems facing developing countries such as China and India, as shown in Figure 7.1. Alone with the administrative level effort to combat pollution by encouraging the purchase of electrical cars, developing renewable energy resources and building public transport infrastructure, considerable attention has been focused on looking for new materials or mechanisms in filtering particulate matter air pollution in both industrial and consumer levels. The most common air filtration systems use a solid-state material, either in the form of a porous membrane or a fibrous filter. The first type is

typically used for nanometer size particles and its main disadvantage is the energy required to flow through the membrane. The second type is available for a wide range of particle sizes and is the typical filter available commercially for both households as well as some industrial settings. The main disadvantage of the fibrous filters is the limited flow rates at which they can operate efficiently. In addition, a common disadvantage of all solid-state filters is the need to replace them frequently and the creation of waste. Besides, these solid-filter-based technologies are often unable to capture gaseous pollutants such as volatile organic compound (VOC) efficiently.

Figure 7.1 Beijing's Forbidden City as seen on a clear day during 2014 APEC conference, and a polluted day one month earlier by Jeffery Kesler.[206]

Inspired by liquid-DLD, we proposed a new air filtration system utilizing an array of anchored liquid bridges as the filtration medium. To be more specific, we can simply turn the separation system that is proposed in chapter 5 into an air filtration system by subjecting it to a cross directional polluted air flow with an optimized array arrangement. In fact, the idea of utilizing the interaction between solid and gas-liquid interface to achieve air filtration is not an original one. One of the traditional ways to remove particulate matter in industrial process, wet scrubbing, for example, achieves gas cleaning by spraying liquid droplets in the opposite direction of a particle-laden gas flow.[207–210] To better comprehend the capturing mechanism of wet scrubbers, a lot of effort has been put into understanding the single droplet capturing process from a theoretical perspective.[207,211,212] The main disadvantage of wet scrubbing is that the droplets that are dispensed into the air are unorganized and the whole capturing process is uncontrollable. Additionally, it requires a large energy consumption to disperse the water stream into millimeter scale droplets and spray them out with a relatively high velocity. In comparison, by keeping the liquid phase stationary, our proposed method is more cost effective with excellent controllability. Specifically, with some engineering effort, we can achieve dynamic control of the diameter of the water bridges and eventually are able to tune the capturing process in real time. Also, going back to the solid state filters, the cleaning and renewing process of our proposed filtering system is straightforward, as well as economical and environmentally friendly.

In general, during the single particle capturing process, there are three different mechanisms contributing to the gas cleaning performance, which are diffusion, interception, and impaction. Particle diffusion effect, characterized by the Peclet number, is inversely proportional to particle size and is only dominant when the particle size is

extremely small ($d_p \leq 0.05\mu m$). In the case of our work where the smallest particle size used is $\sim 10\mu m$, the diffusion effect can be safely ignored. Interception is relatively independent of flow velocity and it characterizes the phenomenon that particles closely following the streamline can still be captured if they get close enough to the air-water interface. Interception scales with $(\frac{d_p}{D})^2$ where D is the diameter of the droplets,[207] and since the diameter ratio between the particle and liquid bridge is very small, interception is also negligible. The dominant mechanism for particle capturing in our experiments is impaction, also referred to as inertial capture,[212] and it is characterized by the Stokes number. In our experiments, since the array of liquid bridges is stationary, the Stokes number can be written as

$$\mathrm{St} = \frac{\rho_p {d_p}^2 U}{18\mu D} \tag{7.1}$$

where ρ_p is the density of the particle, U is the particle velocity, and μ is the viscosity of air. The Stokes number describes how much the particle trajectory deviates from the streamline, and as a result, the larger the Stokes number is, the easier it is for particles to enter the liquid bridge yielding a better gas cleaning result. Based on this analysis, our preliminary exploration focuses mainly on the interaction between single water bridge and the particle-laden gas flow. In our experiments, we alter the particle size, diameter of the bridge and the velocity of the air flow to study the relation between Stokes number and the capture efficiency of the water bridge.

7.2 Experimental set-up and materials

For experimental exploration of the interaction between a single bridge and particle-laden flow, we use a relatively simple setup as shown in Figure 7.2. We create a single water bridge between two parallel clear acrylic plates with gap size controlled by the spacers put in-between them. The gap size g is equivalent to the height of the water bridge. A particle laden flow is then generated and sent into the two parallel plates with controllable flow rate. The particle trajectory is captured with a high speed camera. Particles used on our experiments are two type of glass particles with $\rho_p = 2.48\ g/cm^3$, d_p~55 um and $\rho_p = 1.1\ g/cm^3$, d_p~10 um respectively. Note that for the smaller size particle experiments, we purposefully remove the anchor (a through hole in the bottom plate) to get a better view of the particle trajectory. The various experimental settings are listed in

Table 7.1

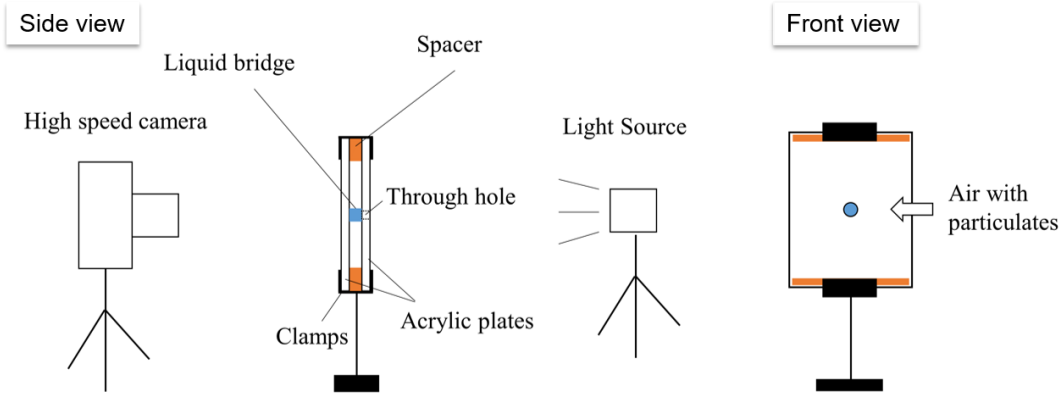

Figure 7.2 Side view and front view of the experimental set-up studying the capturing efficiency of a single water bridge.

Table 7.1 Experimental configurations for all preliminary experiments.

Particle diameter d_p (μm)	Obstacle diameter D (mm)	Gap size g (μm)	Particle velocity range (m/s)	Particle Stokes number range
10	0.5	127	0.5~4	2~12
10	0.67	127	0~6	0~4
10	0.66	127	1~4	1.5~4.5
10	1.34	127	1~18	1~15
10	1.34	127	0~14	0~14
55	2.26	381	0~4.5	0~40

7.3 Problem geometry and particle trajectory types

7.3.1. Problem geometry

To characterize the preliminary experimental results, we define three important concepts which are the incoming offset b_{in}, the capture efficiency η (or collision efficiency), and the attachment efficiency. As shown in Figure 7.3 a), we borrowed the concept from DLD systems and define the incoming offset as the lateral distance between the particle trajectory and the centerline of the liquid bridge. With the consideration of the incoming offset b_{in}, we assume that the position at which particles collide with the liquid bridge will influence the probability of them getting captured. The capture efficiency η is defined as the ratio between the total number of particle that get captured by the water bridge with

respect to the total number of particles that come in within the range $R + r$ (where R is the radius of water bridge, and r is the radius of the particle) from the centerline of the bridge. Not to confuse with the capture efficiency, the attachment efficiency represents the ratio between the number of captured particles staying on the interface with respect to the total number of captured particles. Specifically, as shown in Figure 7.3 b), out of all the captured particles, some of them stayed on the air-water interface for a relatively long time while others enter deep into the water bridge, and the concept of attachment efficiency help characterize this phenomenon.

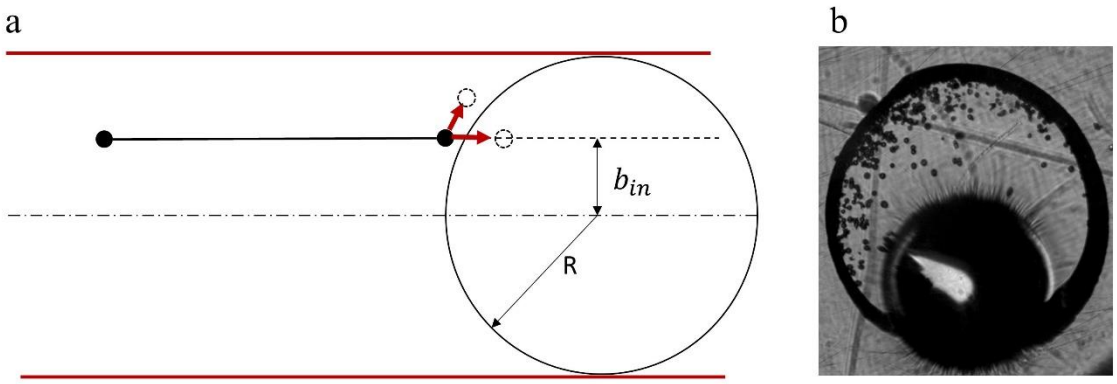

Figure 7.3 a) Schematic picture of particle trajectory and incoming offset. b) Snapshot for experiments with 40 um glass particles and an anchored liquid bridge.

7.3.2. Particle trajectory types

In our experiments, we observe three different types of particle trajectory which are interfacial capture, bulk capture, and trajectories that do not result in particle capture or "no capture". For the " no capture" trajectories, we focus on the particles that get bounced back by the existing particles on the interface and ignore particles that move around the

drop without interacting with the bridge. Explicitly, interfacial capture trajectory and bulk capture trajectory describe the behavior of captured particles with the only difference being whether the particle stays at the interface or enters the drop. Note that the bounced back trajectory defined in our work is fundamentally different from the rebound trajectory defined in previous literatures.[211] Since only hydrophilic glass particles have been used in our preliminary experiments, in theory, rebound would never be observed. Specifically, rebound happens under the action of surface tension on the gas-water interface without the involvement of other particles. In contrast, bounced back trajectory is mainly due to the existence of other particles on the interface. It is a direct result of particles colliding with particles that reside on the interface from previous collisions instead of the interface itself. By definition, the probability of particle traveling in either interfacial capture or bulk capture trajectory determines the overall capture efficiency of a single bridge. And the higher the probability of captured particle travelling in bulk capture trajectory, hence lower attachment efficiency, will also result in a higher overall capture efficiency.

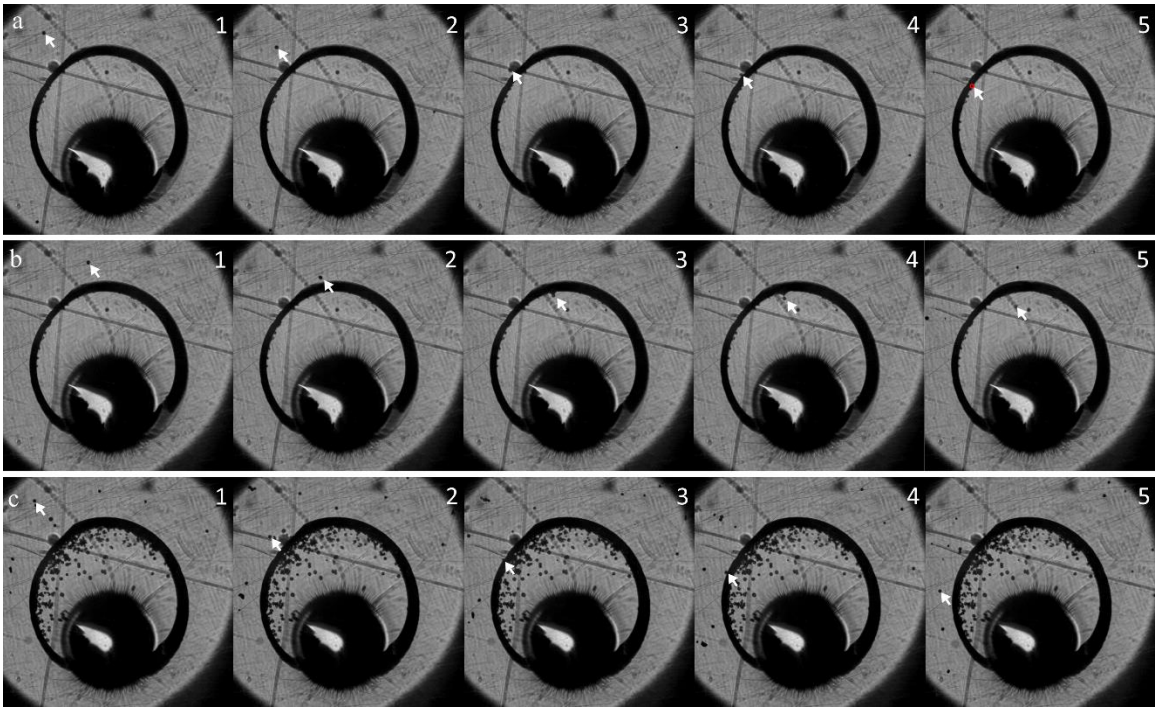

Figure 7.4 a) Particle with oscillation trajectory. Particle enters the liquid bridge and stays on the interface. An observable oscillation of the interface can be noticed. b) Particle with submergence trajectory. Particle eventually enters deep into the bridge. The interface is severely deformed as the particle enters through. c) Particle get bounced by the particles deposited on the interface.

7.4 Results and discussions

Here, we provide the preliminary results on two different types of glass particles under various experimental settings, as listed in Table 7.1. To analyze the experimental results, we manually track particles in each video until the bounced back trajectories are frequently observed. As a result, our analysis mainly focuses on the initial stages of particle capturing where the interface is relatively clean.

With the tracked particle trajectories, we are able to visualize the velocity distribution, calculate the capture efficiency and plot the particle “state of capture” as a function of normalized incoming offset and stokes number, as demonstrated in Figure 7.5 and Figure

7.6. From Figure 7.5b and Figure 7.6b, we notice that the particle velocity in both experiments is almost uniformly distributed within a range of values. To be more specific, for the 55 μm particle experiments, the velocities of the tracked particles fall within the range from 0.5 to 4.5 m/s, and for 10 μm particle experiments, we observe an even larger range in terms of the particle velocity distribution, from 2 m/s to 18 m/s. As a result, the Stokes number corresponding to each tracked particle also varies within a range, $St = 5\sim40$ and 2~15 for 55 μm and 10 μm particles, respectively.

For the capture efficiency curved shown in Figure 7.5c and Figure 7.6c, we can obviously conclude that as the number of captured particles increases, there exists a downward trend for the capture efficiency. However, we argue that a better analysis would include an assessment for the attachment efficiency also. Although unlikely, there might exist a situation where the attachment efficiency is consistently low and correspondingly, the total capture efficiency will be kept at a consistently high level. More importantly, we observe that particles that come into interaction with the water bridge with a smaller b_{in}, meaning that the particle initial trajectory is closer to the centerline of the water bridge, will have a higher probability of getting captured. Consequently, if at the very first few moments of the experiments, only particles with relatively large incoming offset are observed and tracked, then the capture efficiency is likely to start from 0 (Figure 7.5c) In comparison, if the first few tracked particles all are captured particles with relatively smaller incoming offset, the capture efficiency is likely to start from 1 (Figure 7.6c).

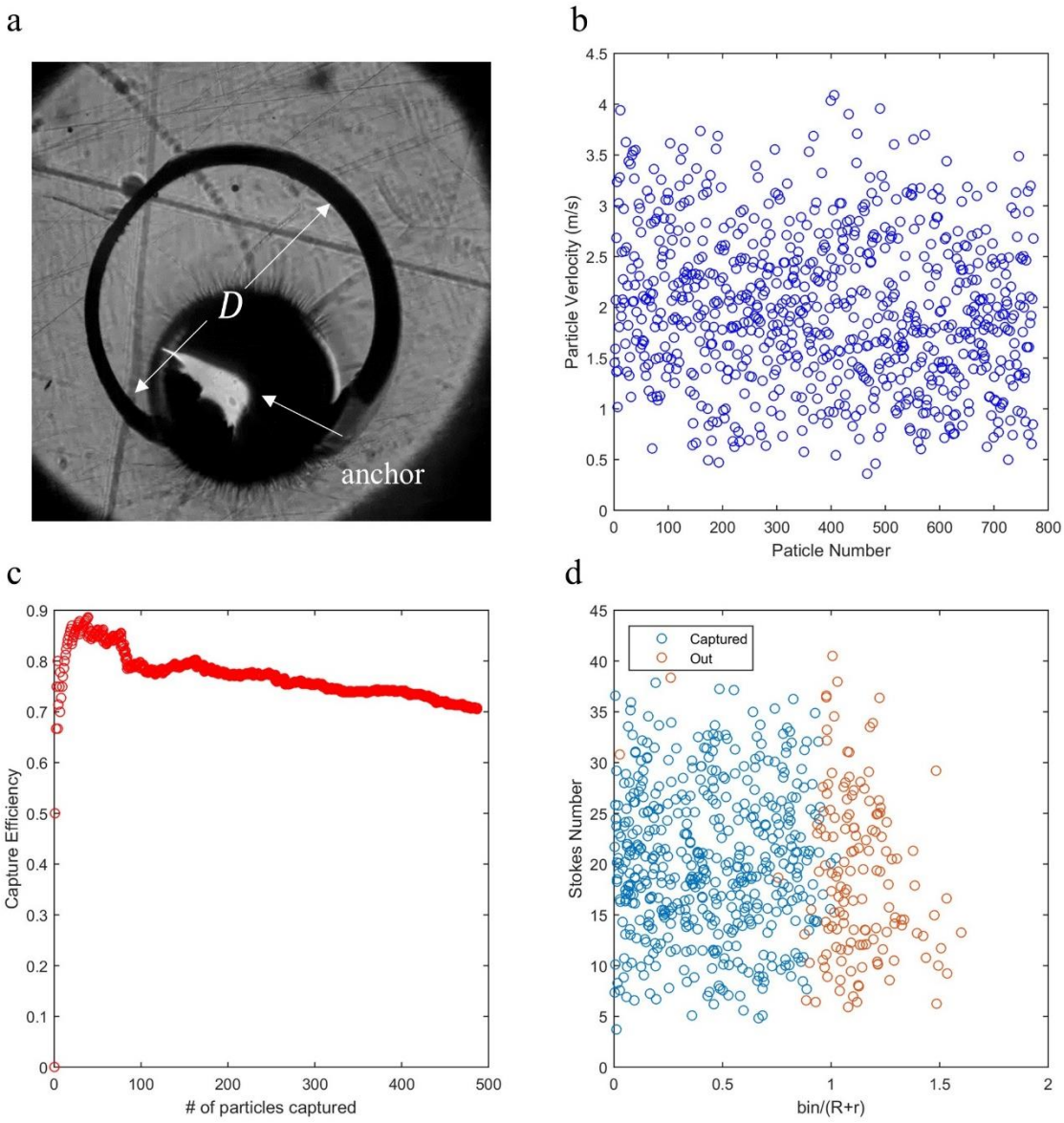

Figure 7.5 Experimental results for d_p~55 μm, $g = 400$ μm, and $D = 3$ mm. a) A snapshot of the experimental settings. b) The velocity distribution for all the particles tracked in the video. c) Capture efficiency as a function of the total number of particles getting captured by the water bridge. d) The particle capture state as a function of normalized incoming offset and particle Stokes number. The blue circles represent the captured particles and the orange circles represent the particles that are not captured by the water bridge as they move around it.

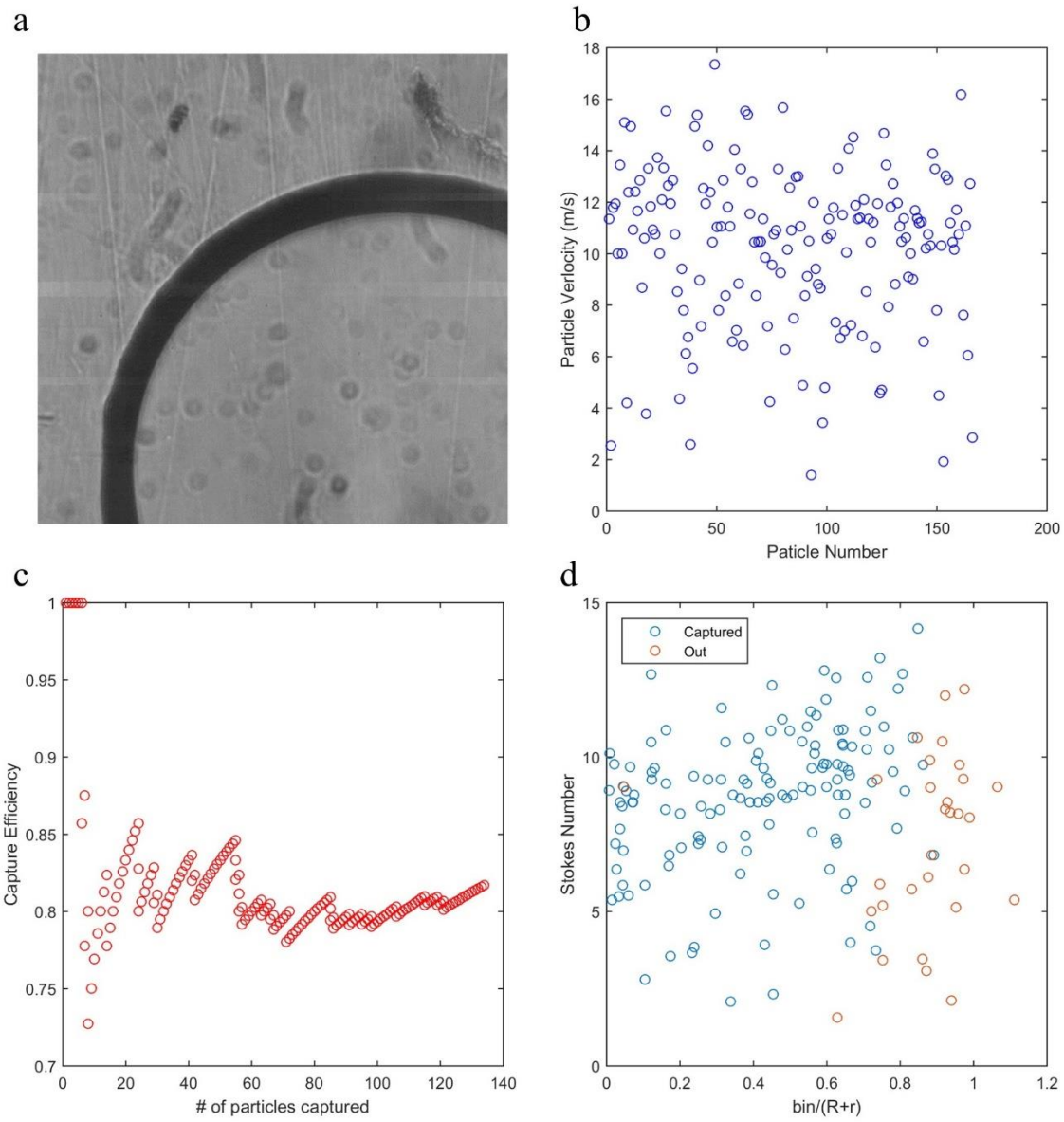

Figure 7.6 Experimental results for d_p~10 μm, $g = 127$ μm, and $D = 1.34$ mm. a) A snapshot of the experimental settings. b) The velocity distribution for all the particles tracked in the video. c) Capture efficiency as a function of the total number of particles getting captured by the water bridge. d) The particle capture state as a function of normalized incoming offset and particle Stokes number. The blue circles represent the captured particles and the orange circles represent the particles that are not captured by the water bridge as they move around it.

In Figure 7.7, we combine the "state of capture" data obtained from various experimental settings into a single plot. To make the experimental data in various settings comparable,

we use the normalized incoming offset $b_{in}/(R+r)$ instead of the real incoming offset to guarantee geometric similarity. Additionally, similar Stokes number guarantees the dynamic similarity of the flow field. And with the satisfaction of both geometric and dynamic similarities, experimental results obtained from different experimental settings can be compared. Notably in Figure 7.7, the boundary between captured and not captured particles seems to follow a universal curve across different experimental settings.

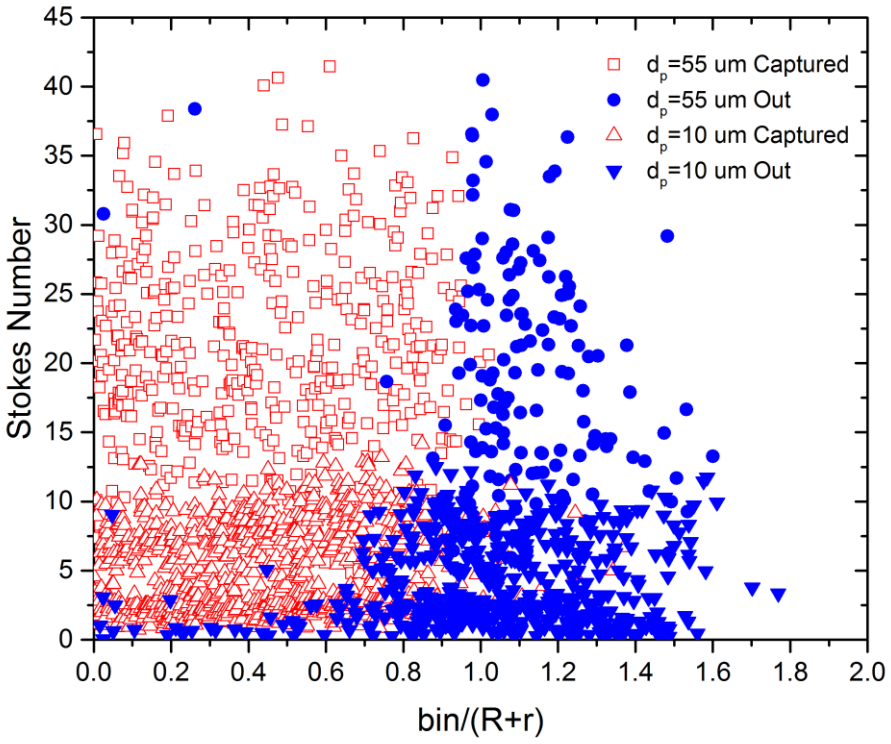

Figure 7.7 Combination of all the experimental results on the particle state of capture as a function of normalized incoming offset and particle Stokes number.

From Figure 7.7 we notice that both incoming offset and Stokes number play an important role in deciding the state of capture for glass particles. To be more specific, we notice that as the normalized incoming offset decreases, if the Stokes number is large enough, particles tend to get captured by the water bridge. In order to show our observation more clearly, we bin the normalized incoming offset, and define the capturing probability as the ratio between the total number of captured particles with respect to the total number of particles in each bin, then plot the capture probability as a function of binned normalized incoming offset as presented in Figure 7.8. We clearly observe that when bin is small enough, the capture probability is very close to 1. Then, as $b_{in}/(R+r)$ increases, the capture probability of the glass particles will sharply transition to 0. We also observe in Figure 7.7 that as the Stokes number increases, more particles tend to get captured regardless of its incoming offset. In particular, when $\mathrm{St} > 15$, almost all the particles that come in with $b_{in}/(R+r) < 1$ will get captured.

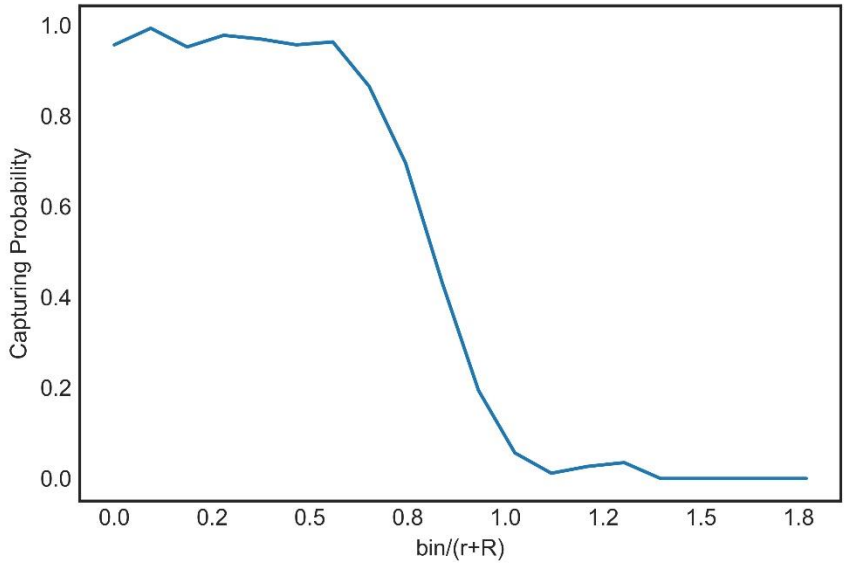

Figure 7.8 Capture probability as a function of binned $b_{in}/(R+r)$

7.5 Looking forward

With the interesting results obtained from the preliminary experiments, we are very excited about the application potential of the proposed system. We also acknowledge that there is considerable amount of research effort needed before the application stage.

First of all, we note that one of the more important particle properties, the hydrophilicity of the particle surface, remains unexplored in our preliminary work. In fact, the particulate matter air pollution is believed to be hydrophobic rather than hydrophilic. As a result, experiments involving particles with different surface chemistry are vital before we can be confident about the particle capturing ability of the proposed system.

In addition, as mentioned in the introduction, $PM_{2.5}$ is generally believed to be the main component for PM induced adverse health effect, and due to the limitation of experimental

equipment, we only focused on particles that are larger than 10 μm in our preliminary exploration. We believe that the proposed system will remain effective for extremely small micro particles such as $PM_{2.5}$, but more advanced equipment and experimental method is needed to provide support to our assumption.

We would also like to point out that using an array of water bridges instead of a single one will undoubtedly increase the capture efficiency of the proposed systems. As a result, a natural step forward would be to explore the optimal array design that can maximize the capture efficiency.

Last by not the least, although particulate matter is our main focus at the moment, we believe that the proposed system is also capable of capturing deformable pollutants or gas pollutant (VOC etc.) or even microorganisms floating in air, which will extend the application potential of the proposed system to realms far beyond the scope of particulate matter filtering.

In conclusion, the problem of extending liquid-DLD into the realm of air pollution filtration is a theoretically rich one. There are numerous directions we can move the research forward on a scientific research level by simply altering various properties of the particles. Also, the application potential of the proposed set-up is endless and awaits to be explored.

Bibliography

1 S. Du and G. Drazer, *J. Micromechanics Microengineering*, 2015, **25**, 114002.
2 S. Du and G. Drazer, *Sci. Rep.*, , DOI:10.1038/srep31428.
3 S. Du, S. Shojaei-Zadeh and G. Drazer, *Soft Matter*, 2017, **13**, 7649–7656.
4 G. M. Whitesides, *Nature*, 2006, **442**, 368–373.
5 F. K. Balagaddé, L. You, C. L. Hansen, F. H. Arnold and S. R. Quake, *Science*, 2005, **309**, 137–140.
6 P. Vulto, S. Podszun, P. Meyer, C. Hermann, A. Manz and G. A. Urban, *Lab. Chip*, 2011, **11**, 1596–1602.
7 C. Liu, J. A. Thompson and H. H. Bau, *Lab. Chip*, 2011, **11**, 1688–1693.
8 J. A. Lounsbury, A. Karlsson, D. C. Miranian, S. M. Cronk, D. A. Nelson, J. Li, D. M. Haverstick, P. Kinnon, D. J. Saul and J. P. Landers, *Lab. Chip*, 2013, **13**, 1384–1393.
9 O. Rahmanian and D. L. DeVoe, *Lab. Chip*, 2013, **13**, 1102–1108.
10 E. Berthier, E. W. K. Young and D. Beebe, *Lab. Chip*, 2012, **12**, 1224–1237.
11 K. Burlage, C. Gerhardy, H. Praefke, M. A. Liauw and W. K. Schomburg, *Chem. Eng. J.*, 2013, **227**, 111–115.
12 C. Renault, X. Li, S. E. Fosdick and R. M. Crooks, *Anal. Chem.*, 2013, **85**, 7976–7979.
13 J. B. You, K.-I. Min, B. Lee, D.-P. Kim and S. G. Im, *Lab. Chip*, 2013, **13**, 1266–1272.
14 C. Chen and T. F. Gerlach, *RSC Adv.*, 2013, **3**, 14066–14072.
15 P. Mazurek, A. E. Daugaard, M. Skolimowski, S. Hvilsted and A. L. Skov, *RSC Adv.*, 2015, **5**, 15379–15386.
16 S. Rose, A. Prevoteau, P. Elzière, D. Hourdet, A. Marcellan and L. Leibler, *Nature*, 2014, **505**, 382–385.
17 F. I. Uba, B. Hu, K. Weerakoon-Ratnayake, N. Oliver-Calixte and S. A. Soper, *Lab. Chip*, 2015, **15**, 1038–1049.
18 A. Konda, J. M. Taylor, M. A. Stoller and S. A. Morin, *Lab. Chip*, 2015, **15**, 2009–2017.
19 J. M. Jackson, M. A. Witek, M. L. Hupert, C. Brady, S. Pullagurla, J. Kamande, R. D. Aufforth, C. J. Tignanelli, R. J. Torphy, J. J. Yeh and S. A. Soper, *Lab. Chip*, 2013, **14**, 106–117.
20 Z. Zhang, X. Feng, F. Xu, X. Hu, P. Li and B.-F. Liu, *Anal. Methods*, 2013, **5**, 4694–4700.
21 T. Wu, H. Suzuki, Y. Su, Z. Tang, L. Zhang and T. Yomo, *Soft Matter*, 2013, **9**, 3473–3477.
22 R. W. Style, Y. Che, S. J. Park, B. M. Weon, J. H. Je, C. Hyland, G. K. German, M. P. Power, L. A. Wilen, J. S. Wettlaufer and E. R. Dufresne, *Proc. Natl. Acad. Sci.*, 2013, **110**, 12541–12544.
23 W. Zhang, D. S. Choi, Y. H. Nguyen, J. Chang and L. Qin, *Sci. Rep.*, 2013, **3**, srep02332.
24 Y.-T. Lu, L. Zhao, Q. Shen, M. A. Garcia, D. Wu, S. Hou, M. Song, X. Xu, W.-H. OuYang, W. W.-L. OuYang, J. Lichterman, Z. Luo, X. Xuan, J. Huang, L. W. K.

Chung, M. Rettig, H.-R. Tseng, C. Shao and E. M. Posadas, *Methods*, 2013, **64**, 144–152.
25 N. G. Batz, J. S. Mellors, J. P. Alarie and J. M. Ramsey, *Anal. Chem.*, 2014, **86**, 3493–3500.
26 M. Kitsara, C. E. Nwankire, L. Walsh, G. Hughes, M. Somers, D. Kurzbuch, X. Zhang, G. G. Donohoe, R. O'Kennedy and J. Ducrée, *Microfluid. Nanofluidics*, 2014, **16**, 691–699.
27 S. Vafaei and D. Wen, *Adv. Colloid Interface Sci.*, , DOI:10.1016/j.cis.2015.07.006.
28 K.-C. Hsu, C.-F. Lee, W.-C. Tseng, Y.-Y. Chao and Y.-L. Huang, *Talanta*, 2014, **128**, 408–413.
29 M. Jang, C. K. Park and N. Y. Lee, *Sens. Actuators B Chem.*, 2014, **193**, 599–607.
30 M. Dirany, L. Dies, F. Restagno, L. L éger, C. Poulard and G. Miquelard-Garnier, *Colloids Surf. Physicochem. Eng. Asp.*, 2015, **468**, 174–183.
31 Y. Chen, W. Pei, R. Tang, S. Chen and H. Chen, *Sens. Actuators Phys.*, 2013, **189**, 143–150.
32 B. Farshchian, S. Park, J. Choi, A. Amirsadeghi, J. Lee and S. Park, *Lab. Chip*, 2012, **12**, 4764–4771.
33 Y. Hosseini, P. Zellner and M. Agah, *J. Microelectromechanical Syst.*, 2013, **22**, 356–362.
34 S. Rekštytė, M. Malinauskas and S. Juodkazis, *Opt. Express*, 2013, **21**, 17028–17041.
35 G. Comina, A. Suska and D. Filippini, *Lab. Chip*, 2014, **14**, 2978–2982.
36 T. Q. Huang, X. Qu, J. Liu and S. Chen, *Biomed. Microdevices*, 2014, **16**, 127–132.
37 W. Lee, D. Kwon, B. Chung, G. Y. Jung, A. Au, A. Folch and S. Jeon, *Anal. Chem.*, 2014, **86**, 6683–6688.
38 F. Yu, M. A. Horowitz and S. R. Quake, *Lab. Chip*, 2013, **13**, 1911–1918.
39 S.-J. Kim, S. Paczesny, S. Takayama and K. Kurabayashi, *Lab. Chip*, 2013, **13**, 2091–2098.
40 P. Novo, F. Volpetti, V. Chu and J. P. Conde, *Lab. Chip*, 2013, **13**, 641–645.
41 G. Wang, H.-P. Ho, Q. Chen, A. K.-L. Yang, H.-C. Kwok, S.-Y. Wu, S.-K. Kong, Y.-W. Kwan and X. Zhang, *Lab. Chip*, 2013, **13**, 3698–3706.
42 T. H. G. Thio, F. Ibrahim, W. Al-Faqheri, J. Moebius, N. S. Khalid, N. Soin, M. K. B. A. Kahar and M. Madou, *Lab. Chip*, 2013, **13**, 3199–3209.
43 S. Begolo, D. V. Zhukov, D. A. Selck, L. Li and R. F. Ismagilov, *Lab. Chip*, 2014, **14**, 4616–4628.
44 M. Gao and L. Gui, *Lab. Chip*, 2014, **14**, 1866–1872.
45 X. Li, P. Zwanenburg and X. Liu, *Lab. Chip*, 2013, **13**, 2609–2614.
46 G. A. Cooksey and J. Atencia, *Lab. Chip*, 2014, **14**, 1665–1668.
47 A. Kazemzadeh, P. Ganesan, F. Ibrahim, M. M. Aeinehvand, L. Kulinsky and M. J. Madou, *Sens. Actuators B Chem.*, 2014, **204**, 149–158.
48 C.-Y. Chen, C.-Y. Chen, C.-Y. Lin and Y.-T. Hu, *Lab. Chip*, 2013, **13**, 2834–2839.
49 E. Choi, K. Kwon, S. J. Lee, D. Kim and J. Park, *Lab. Chip*, 2015, **15**, 1794–1798.
50 D. Ahmed, C. Y. Chan, S.-C. S. Lin, H. S. Muddana, N. Nama, S. J. Benkovic and T. J. Huang, *Lab. Chip*, 2013, **13**, 328–331.
51 R. M. Cooper, D. C. Leslie, K. Domansky, A. Jain, C. Yung, M. Cho, S. Workman, M. Super and D. E. Ingber, *Lab. Chip*, 2013, **14**, 182–188.

52 M. Glynn, D. Kirby, D. Chung, D. J. Kinahan, G. Kijanka and J. Ducrée, *J. Lab. Autom.*, 2014, **19**, 285–296.
53 J. C. Albrecht, A. Kotani, J. S. Lin, S. A. Soper and A. E. Barron, *ELECTROPHORESIS*, 2013, **34**, 590–597.
54 D. P. Manage, D. G. Elliott and C. J. Backhouse, *ELECTROPHORESIS*, 2012, **33**, 3213–3221.
55 J. Huft, C. A. Haynes and C. L. Hansen, *Anal. Chem.*, 2013, **85**, 1797–1802.
56 S. Sukas, W. De Malsche, G. Desmet and H. J. G. E. Gardeniers, *Anal. Chem.*, 2012, **84**, 9996–10004.
57 A. M. Tentori, A. J. Hughes and A. E. Herr, *Anal. Chem.*, 2013, **85**, 4538–4545.
58 T. Le Échéand D. Bourrier, *Lab. Chip*, 2015, **15**, 833–838.
59 T. Zhu, R. Cheng, Y. Liu, J. He and L. Mao, *Microfluid. Nanofluidics*, 2014, **17**, 973–982.
60 Y. Huang and A. J. Mason, *Lab. Chip*, 2013, **13**, 3929–3934.
61 N. Godino, R. Gorkin, K. Bourke and J. Ducrée, *Lab. Chip*, 2012, **12**, 3281–3284.
62 R. A. Saylor, E. A. Reid and S. M. Lunte, *ELECTROPHORESIS*, 2015, **36**, 1912–1919.
63 A. J. Gaudry, M. C. Breadmore and R. M. Guijt, *Electrophoresis*, 2013, **34**, 2980–2987.
64 E. W. M. Kemna, L. I. Segerink, F. Wolbers, I. Vermes and A. van den Berg, *Analyst*, 2013, **138**, 4585–4592.
65 C. Andreou, M. R. Hoonejani, M. R. Barmi, M. Moskovits and C. D. Meinhart, *ACS Nano*, 2013, **7**, 7157–7164.
66 X. Sun, K. Tang, R. D. Smith and R. T. Kelly, *Microfluid. Nanofluidics*, 2013, **15**, 117–126.
67 S. K. Küster, S. R. Fagerer, P. E. Verboket, K. Eyer, K. Jefimovs, R. Zenobi and P. S. Dittrich, *Anal. Chem.*, 2013, **85**, 1285–1289.
68 R. Regmi, A. A. A. Balushi, H. Rigneault, R. Gordon and J. Wenger, *Sci. Rep.*, 2015, **5**, srep15852.
69 T.-A. Meier, E. Poehler, F. Kemper, O. Pabst, H.-G. Jahnke, E. Beckert, A. Robitzki and D. Belder, *Lab. Chip*, 2015, **15**, 2923–2927.
70 W. A. Black, B. B. Stocks, J. S. Mellors, J. R. Engen and J. M. Ramsey, *Anal. Chem.*, 2015, **87**, 6280–6287.
71 V. V. Thacker, K. Bromek, B. Meijer, J. Kotar, B. Sclavi, M. C. Lagomarsino, U. F. Keyser and P. Cicuta, *Integr. Biol.*, 2014, **6**, 184–191.
72 Y. Zhao, X. T. Zhao, D. Y. Chen, Y. N. Luo, M. Jiang, C. Wei, R. Long, W. T. Yue, J. B. Wang and J. Chen, *Biosens. Bioelectron.*, 2014, **57**, 245–253.
73 R. Baudoin, A. Legendre, S. Jacques, J. Cotton, F. Bois and E. Leclerc, *J. Pharm. Sci.*, 2014, **103**, 706–718.
74 T. C. Scanlon, S. M. Dostal and K. E. Griswold, *Biotechnol. Bioeng.*, 2014, **111**, 232–243.
75 J. Reboud, Y. Bourquin, R. Wilson, G. S. Pall, M. Jiwaji, A. R. Pitt, A. Graham, A. P. Waters and J. M. Cooper, *Proc. Natl. Acad. Sci.*, 2012, **109**, 15162–15167.
76 T. D. Rane, H. C. Zec, C. Puleo, A. P. Lee and T.-H. Wang, *Lab. Chip*, 2012, **12**, 3341–3347.
77 S. Petralia, R. Verardo, E. Klaric, S. Cavallaro, E. Alessi and C. Schneider, *Sens. Actuators B Chem.*, 2013, **187**, 99–105.

78 R. Zhang, H.-Q. Gong, X. Zeng, C. Lou and C. Sze, *Anal. Chem.*, 2013, **85**, 1484–1491.
79 C.-H. Chiou, D. Jin Shin, Y. Zhang and T.-H. Wang, *Biosens. Bioelectron.*, 2013, **50**, 91–99.
80 R. C. den Dulk, K. A. Schmidt, G. Sabatté, S. Liébana and M. W. J. Prins, *Lab. Chip*, 2012, **13**, 106–118.
81 D. J. Eastburn, A. Sciambi and A. R. Abate, *PLOS ONE*, 2013, **8**, e62961.
82 M. E. Warkiani, A. K. P. Tay, B. L. Khoo, X. Xiaofeng, J. Han and C. T. Lim, *Lab. Chip*, 2015, **15**, 1101–1109.
83 G. Czilwik, I. Schwarz, M. Keller, S. Wadle, S. Zehnle, F. von Stetten, D. Mark, R. Zengerle and N. Paust, *Lab. Chip*, 2015, **15**, 1084–1091.
84 Q. Zhu, L. Qiu, B. Yu, Y. Xu, Y. Gao, T. Pan, Q. Tian, Q. Song, W. Jin, Q. Jin and Y. Mu, *Lab. Chip*, 2014, **14**, 1176–1185.
85 S. J. Reinholt, A. Behrent, C. Greene, A. Kalfe and A. J. Baeumner, *Anal. Chem.*, 2014, **86**, 849–856.
86 V. Foderà, S. Pagliara, O. Otto, U. F. Keyser and A. M. Donald, *J. Phys. Chem. Lett.*, 2012, **3**, 2803–2807.
87 K. S. Burke, D. Parul, M. J. Reddish and R. B. Dyer, *Lab. Chip*, 2013, **13**, 2912–2921.
88 J. Mok, M. N. Mindrinos, R. W. Davis and M. Javanmard, *Proc. Natl. Acad. Sci.*, 2014, **111**, 2110–2115.
89 L. Wu, G. Guan, H. W. Hou, A. A. S. Bhagat and J. Han, *Anal. Chem.*, 2012, **84**, 9324–9331.
90 W. Zhang, K. Kai, D. S. Choi, T. Iwamoto, Y. H. Nguyen, H. Wong, M. D. Landis, N. T. Ueno, J. Chang and L. Qin, *Proc. Natl. Acad. Sci.*, 2012, **109**, 18707–18712.
91 C. Kim, K. Kreppenhofer, J. Kashef, D. Gradl, D. Herrmann, M. Schneider, R. Ahrens, A. Guber and D. Wedlich, *Lab. Chip*, 2012, **12**, 5186–5194.
92 K.-W. Huang, Y.-C. Wu, J.-A. Lee and P.-Y. Chiou, *Lab. Chip*, 2013, **13**, 3721–3727.
93 J. Zhou, P. V. Giridhar, S. Kasper and I. Papautsky, *Lab. Chip*, 2013, **13**, 1919–1929.
94 S. Hou, L. Zhao, Q. Shen, J. Yu, C. Ng, X. Kong, D. Wu, M. Song, X. Shi, X. Xu, W.-H. OuYang, R. He, X.-Z. Zhao, T. Lee, F. C. Brunicardi, M. A. Garcia, A. Ribas, R. S. Lo and H.-R. Tseng, *Angew. Chem. Int. Ed.*, 2013, **52**, 3379–3383.
95 W. Zhao, C. H. Cui, S. Bose, D. Guo, C. Shen, W. P. Wong, K. Halvorsen, O. C. Farokhzad, G. S. L. Teo, J. A. Phillips, D. M. Dorfman, R. Karnik and J. M. Karp, *Proc. Natl. Acad. Sci.*, 2012, **109**, 19626–19631.
96 X. Su, A. B. Theberge, C. T. January and D. J. Beebe, *Anal. Chem.*, 2013, **85**, 1562–1570.
97 E. Berthier, D. J. Guckenberger, P. Cavnar, A. Huttenlocher, N. P. Keller and D. J. Beebe, *Lab. Chip*, 2013, **13**, 424–431.
98 M. Hamon, S. Jambovane, L. Bradley, A. Khademhosseini and J. W. Hong, *Anal. Chem.*, 2013, **85**, 5249–5254.
99 H. Hwang, Y. Kim, J. Cho, J. Lee, M.-S. Choi and Y.-K. Cho, *Anal. Chem.*, 2013, **85**, 2954–2960.
100 B. D. Piorek, S. J. Lee, M. Moskovits and C. D. Meinhart, *Anal. Chem.*, 2012, **84**, 9700–9705.
101 W.-J. Kim, S. Kim, A. R. Kim and D. J. Yoo, *Ind. Eng. Chem. Res.*, 2013, **52**, 7282–7288.

102 W. Song, H. Fadaei and D. Sinton, *Environ. Sci. Technol.*, 2014, **48**, 3567–3574.
103 A. Golberg, G. Linshiz, I. Kravets, N. Stawski, N. J. Hillson, M. L. Yarmush, R. S. Marks and T. Konry, *PLOS ONE*, 2014, **9**, e86341.
104 G. Korir and M. Prakash, *PLOS ONE*, 2015, **10**, e0115993.
105 A. H. C. Ng, K. Choi, R. P. Luoma, J. M. Robinson and A. R. Wheeler, *Anal. Chem.*, 2012, **84**, 8805–8812.
106 A. E. Kirby and A. R. Wheeler, *Anal. Chem.*, 2013, **85**, 6178–6184.
107 H. Ko, J. Lee, Y. Kim, B. Lee, C.-H. Jung, J.-H. Choi, O.-S. Kwon and K. Shin, *Adv. Mater.*, 2014, **26**, 2335–2340.
108 S. C. C. Shih, P. C. Gach, J. Sustarich, B. A. Simmons, P. D. Adams, S. Singh and A. K. Singh, *Lab. Chip*, 2014, **15**, 225–236.
109 N. M. Lafrenière, J. M. Mudrik, A. H. C. Ng, B. Seale, N. Spooner and A. R. Wheeler, *Anal. Chem.*, 2015, **87**, 3902–3910.
110 Y. Gao, A. W. Y. Lam and W. C. W. Chan, *ACS Appl. Mater. Interfaces*, 2013, **5**, 2853–2860.
111 F. B. Myers, R. H. Henrikson, J. Bone and L. P. Lee, *PLOS ONE*, 2013, **8**, e70266.
112 Z. Zhu, Z. Guan, S. Jia, Z. Lei, S. Lin, H. Zhang, Y. Ma, Z.-Q. Tian and C. J. Yang, *Angew. Chem. Int. Ed.*, 2014, **53**, 12503–12507.
113 R. Nosrati, M. Vollmer, L. Eamer, M. C. S. Gabriel, K. Zeidan, A. Zini and D. Sinton, *Lab. Chip*, 2014, **14**, 1142–1150.
114 S. Wang, S. Tasoglu, P. Z. Chen, M. Chen, R. Akbas, S. Wach, C. I. Ozdemir, U. A. Gurkan, F. F. Giguel, D. R. Kuritzkes and U. Demirci, *Sci. Rep.*, 2014, **4**, srep03796.
115 M. Safavieh, M. U. Ahmed, A. Ng and M. Zourob, *Biosens. Bioelectron.*, 2014, **58**, 101–106.
116 Y. Li, J. Xuan, T. Xia, X. Han, Y. Song, Z. Cao, X. Jiang, Y. Guo, P. Wang and L. Qin, *Anal. Chem.*, 2015, **87**, 3771–3777.
117 P. R. C. Gascoyne and J. Vykoukal, *Electrophoresis*, 2002, **23**, 1973–1983.
118 N. Pamme and A. Manz, *Anal. Chem.*, 2004, **76**, 7250–7256.
119 F. Petersson, L. Åberg, A.-M. Swärd-Nilsson and T. Laurell, *Anal. Chem.*, 2007, **79**, 5117–5123.
120 M. P. MacDonald, G. C. Spalding and K. Dholakia, *Nature*, 2003, **426**, 421–424.
121 A. Jonáš and P. Zemanek, *Electrophoresis*, 2008, **29**, 4813–4851.
122 J. C. Giddings, F. J. Yang and M. N. Myers, *Science*, 1976, **193**, 1244–1245.
123 J. C. Giddings, *Science*, 1993, **260**, 1456–1465.
124 B. Roda, A. Zattoni, P. Reschiglian, M. H. Moon, M. Mirasoli, E. Michelini and A. Roda, *Anal. Chim. Acta*, 2009, **635**, 132–143.
125 M. Baalousha, B. Stolpe and J. R. Lead, *J. Chromatogr. A*, 2011, **1218**, 4078–4103.
126 J. A. Bernate and G. Drazer, *Phys. Rev. Lett.*, 2012, **108**, 214501.
127 J. A. Bernate, C. Liu, L. Lagae, K. Konstantopoulos and G. Drazer, *Lab. Chip*, 2013, **13**, 1086.
128 M. Yamada and M. Seki, *Lab. Chip*, 2005, **5**, 1233–1239.
129 M. Yamada, M. Nakashima and M. Seki, *Anal. Chem.*, 2004, **76**, 5465–5471.
130 M. Luo, F. Sweeney, S. R. Risbud, G. Drazer and J. Frechette, *Appl. Phys. Lett.*, 2011, **99**, 064102.
131 S. R. Risbud, M. Luo, J. Fréchette and G. Drazer, *Phys. Fluids*, 2013, **25**, 062001.
132 S. R. Risbud and G. Drazer, *Microfluid. Nanofluidics*, 2014, **17**, 1003–1009.

133 D. Di Carlo, *Lab. Chip*, 2009, **9**, 3038–3046.
134 T. Kulrattanarak, R. G. M. van der Sman, Y. S. Lubbersen, C. G. P. H. Schroën, H. T. M. Pham, P. M. Sarro and R. M. Boom, *J. Colloid Interface Sci.*, 2011, **354**, 7–14.
135 T. Kulrattanarak, R. G. M. van der Sman, C. G. P. H. Schroën and R. M. Boom, *Microfluid. Nanofluidics*, 2011, **10**, 843–853.
136 M. Balvin, E. Sohn, T. Iracki, G. Drazer and J. Frechette, *Phys. Rev. Lett.*, 2009, **103**, 078301.
137 J. Koplik and G. Drazer, *Phys. Fluids*, 2010, **22**, 052005.
138 S. R. Risbud and G. Drazer, *Phys. Rev. E*, 2014, **90**, 012302.
139 L. R. Huang, E. C. Cox, R. H. Austin and J. C. Sturm, *Science*, 2004, **304**, 987–990.
140 R. Devendra and G. Drazer, *Anal. Chem.*, 2012, **84**, 10621–10627.
141 T. Bowman, J. Frechette and G. Drazer, *Lab. Chip*, 2012, **12**, 2903.
142 S. Hanasoge, R. Devendra, F. J. Diez and G. Drazer, *Microfluid. Nanofluidics*, 2015, **18**, 1195–1200.
143 R. Devendra and G. Drazer, *Microfluid. Nanofluidics*, 2014, **17**, 519–526.
144 M. Jiang, A. D. Mazzeo and G. Drazer, *Microfluid. Nanofluidics*, 2016, **20**, 1–10.
145 J. A. Davis, D. W. Inglis, K. J. Morton, D. A. Lawrence, L. R. Huang, S. Y. Chou, J. C. Sturm and R. H. Austin, *Proc. Natl. Acad. Sci.*, 2006, **103**, 14779–14784.
146 K. K. Zeming, S. Ranjan and Y. Zhang, *Nat. Commun. Lond.*, 2013, **4**, 1625.
147 D. Holmes, G. Whyte, J. Bailey, N. Vergara-Irigaray, A. Ekpenyong, J. Guck and T. Duke, *Interface Focus*, 2014, **4**, 20140011.
148 S. Ranjan, K. Kwek Zeming, R. Jureen, D. Fisher and Y. Zhang, *Lab. Chip*, 2014, **14**, 4250–4262.
149 J. D'Silva, R. H. Austin and J. C. Sturm, *Lab. Chip*, 2015, **15**, 2240–2247.
150 C. I. Civin, T. Ward, A. M. Skelley, K. Gandhi, Z. Peilun Lee, C. R. Dosier, J. L. D'Silva, Y. Chen, M. Kim, J. Moynihan, X. Chen, L. Aurich, S. Gulnik, G. C. Brittain, D. J. Recktenwald, R. H. Austin and J. C. Sturm, *Cytometry A*, 2016, **89**, 1073–1083.
151 K. K. Zeming, T. Salafi, C.-H. Chen and Y. Zhang, *Sci. Rep.*, , DOI:10.1038/srep22934.
152 S. H. Holm, J. P. Beech, M. P. Barrett and J. O. Tegenfeldt, *Anal. Methods*, 2016, **8**, 3291–3300.
153 S. H. Holm, J. P. Beech, M. P. Barrett and J. O. Tegenfeldt, *Lab. Chip*, 2011, **11**, 1326–1332.
154 N. M. Karabacak, P. S. Spuhler, F. Fachin, E. J. Lim, V. Pai, E. Ozkumur, J. M. Martel, N. Kojic, K. Smith, P. Chen, J. Yang, H. Hwang, B. Morgan, J. Trautwein, T. A. Barber, S. L. Stott, S. Maheswaran, R. Kapur, D. A. Haber and M. Toner, *Nat. Protoc.*, 2014, **9**, 694–710.
155 Z. Liu, F. Huang, J. Du, W. Shu, H. Feng, X. Xu and Y. Chen, *Biomicrofluidics*, , DOI:10.1063/1.4774308.
156 S. H. Au, J. Edd, A. E. Stoddard, K. H. K. Wong, F. Fachin, S. Maheswaran, D. A. Haber, S. L. Stott, R. Kapur and M. Toner, *Sci. Rep.*, , DOI:10.1038/s41598-017-01150-3.
157 B. Zhang, J. V. Green, S. K. Murthy and M. Radisic, *PLOS ONE*, 2012, **7**, e37619.
158 T. A. J. Duke and R. H. Austin, *Phys. Rev. Lett.*, 1998, **80**, 1552–1555.
159 C.-F. Chou, O. Bakajin, S. W. P. Turner, T. A. J. Duke, S. S. Chan, E. C. Cox, H. G. Craighead and R. H. Austin, *Proc. Natl. Acad. Sci.*, 1999, **96**, 13762–13765.

160 L. R. Huang, P. Silberzan, J. O. Tegenfeldt, E. C. Cox, J. C. Sturm, R. H. Austin and H. Craighead, *Phys. Rev. Lett.*, 2002, **89**, 178301.
161 N. Kaji, Y. Tezuka, Y. Takamura, M. Ueda, T. Nishimoto, H. Nakanishi, Y. Horiike and Y. Baba, *Anal. Chem.*, 2004, **76**, 15–22.
162 L. R. Huang, J. O. Tegenfeldt, J. J. Kraeft, J. C. Sturm, R. H. Austin and E. C. Cox, *Nat. Biotechnol.*, 2002, **20**, 1048–1051.
163 Y. Chen, E. S. Abrams, T. C. Boles, J. N. Pedersen, H. Flyvbjerg, R. H. Austin and J. C. Sturm, *Phys. Rev. Lett.*, 2015, **114**, 198303.
164 M. Jiang, K. Budzan and G. Drazer, *Microfluid. Nanofluidics*, 2015, **19**, 427–434.
165 H. N. Joensson, M. Uhlén and H. Andersson Svahn, *Lab. Chip*, 2011, **11**, 1305–1310.
166 T. Krüger, D. Holmes and P. V. Coveney, *Biomicrofluidics*, 2014, **8**, 1–15.
167 R. Quek, D. V. Le and K.-H. Chiam, *Phys. Rev. E*, 2011, **83**, 056301.
168 S. Ye, X. Shao, Z. Yu and W. Yu, *J. Fluid Mech.*, 2014, **743**, 60–74.
169 J. P. Beech, S. H. Holm, K. Adolfsson and J. O. Tegenfeldt, *Lab. Chip*, 2012, **12**, 1048–1051.
170 K. Loutherback, K. S. Chou, J. Newman, J. Puchalla, R. H. Austin and J. C. Sturm, *Microfluid. Nanofluidics*, 2010, **9**, 1143–1149.
171 Z. Zhang, E. Henry, G. Gompper and D. A. Fedosov, *J. Chem. Phys.*, 2015, **143**, 243145.
172 J. Wei, H. Song, Z. Shen, Y. He, X. Xu, Y. Zhang and B. N. Li*, *IEEE Trans. NanoBioscience*, 2015, **14**, 660–667.
173 R. Vernekar, T. Krüger, K. Loutherback, K. Morton and D. W. Inglis, *Lab. Chip*, 2017, **17**, 3318–3330.
174 D. W. Inglis, J. A. Davis, R. H. Austin and J. C. Sturm, *Lab. Chip*, 2006, **6**, 655–658.
175 S. R. Risbud and G. Drazer, *J. Fluid Mech.*, 2013, **714**, 213–237.
176 S. R. Risbud and G. Drazer, *Phys. Rev. E*, 2014, **90**, 012302.
177 J. Frechette and G. Drazer, *J. Fluid Mech.*, 2009, **627**, 379–401.
178 N.-S. Cheng, *Ind. Eng. Chem. Res.*, 2008, **47**, 3285–3288.
179 K. Loutherback, J. D'Silva, L. Liu, A. Wu, R. H. Austin and J. C. Sturm, *AIP Adv.*, 2012, **2**, 042107.
180 D. W. Inglis, J. A. Davis, R. H. Austin and J. C. Sturm, *Lab. Chip*, 2006, **6**, 655–658.
181 T. Kulrattanarak, R. G. M. Van der Sman, Y. S. Lubbersen, C. Schroën, H. T. M. Pham, P. M. Sarro and R. M. Boom, *J. Colloid Interface Sci.*, 2011, **354**, 7–14.
182 T. Kulrattanarak, R. G. M. van der Sman, C. Schroën and R. M. Boom, *Microfluid. Nanofluidics*, 2011, **10**, 843–853.
183 S. R. Risbud and G. Drazer, *Phys. Rev. E*, 2014, **90**, 012302.
184 J. Frechette and G. Drazer, *J. Fluid Mech.*, 2009, **627**, 379–401.
185 G. Drazer, J. Koplik, B. Khusid and A. Acrivos, *J. Fluid Mech.*, 2002, **460**, 307–335.
186 J. Herrmann, M. Karweit and G. Drazer, *Phys. Rev. E*, 2009, **79**, 061404.
187 A. Huebner, D. Bratton, G. Whyte, M. Yang, A. J. deMello, C. Abell and F. Hollfelder, *Lab. Chip*, 2009, **9**, 692–698.
188 Y. Bai, X. He, D. Liu, S. N. Patil, D. Bratton, A. Huebner, F. Hollfelder, C. Abell and W. T. S. Huck, *Lab. Chip*, 2010, **10**, 1281–1285.
189 F. Shen, W. Du, J. E. Kreutz, A. Fok and R. F. Ismagilov, *Lab. Chip*, 2010, **10**, 2666–2672.

190 R. J. Jackman, D. C. Duffy, E. Ostuni, N. D. Willmore and G. M. Whitesides, *Anal. Chem.*, 1998, **70**, 2280–2287.
191 T. J. Bowman, G. Drazer and J. Frechette, *Biomicrofluidics*, 2013, **7**, 064111.
192 J. Herrmann, M. Karweit and G. Drazer, *Phys. Rev. E*, 2009, **79**, 061404.
193 R. Devendra and G. Drazer, *Microfluid. Nanofluidics*, 2014, **17**, 519–526.
194 T. Bowman, J. Frechette and G. Drazer, *Lab. Chip*, 2012, **12**, 2903–2908.
195 R. M. Harrison and J. Yin, *Sci. Total Environ.*, 2000, **249**, 85–101.
196 C. A. P. III and D. W. Dockery, *J. Air Waste Manag. Assoc.*, 2006, **56**, 709–742.
197 A. Churg, M. Brauer, M. del Carmen Avila-Casado, T. I. Fortoul and J. L. Wright, *Environ. Health Perspect.*, 2003, **111**, 714–718.
198 S. F. van Eeden, A. Yeung, K. Quinlam and J. C. Hogg, *Proc. Am. Thorac. Soc.*, 2005, **2**, 61–67.
199 R. D. Brook, J. R. Brook, B. Urch, R. Vincent, S. Rajagopalan and F. Silverman, *Circulation*, 2002, **105**, 1534–1536.
200 M. S. O'Neill, A. Veves, A. Zanobetti, J. A. Sarnat, D. R. Gold, P. A. Economides, E. S. Horton and J. Schwartz, *Circulation*, 2005, **111**, 2913–2920.
201 R. D. Brook, S. Rajagopalan, C. A. Pope, J. R. Brook, A. Bhatnagar, A. V. Diez-Roux, F. Holguin, Y. Hong, R. V. Luepker, M. A. Mittleman, A. Peters, D. Siscovick, S. C. Smith, L. Whitsel and J. D. Kaufman, *Circulation*, 2010, **121**, 2331–2378.
202 B. Z. Simkhovich, M. T. Kleinman and R. A. Kloner, *J. Am. Coll. Cardiol.*, 2008, **52**, 719–726.
203 R. D. Brook, B. Franklin, W. Cascio, Y. Hong, G. Howard, M. Lipsett, R. Luepker, M. Mittleman, J. Samet, S. C. Smith, I. Tager and Expert Panel on Population and Prevention Science of the American Heart Association, *Circulation*, 2004, **109**, 2655–2671.
204 P. T. Thomas and J. T. Zelikoff, in *Air Pollution and Health*, eds. S. T. Holgate, J. M. Samet, H. S. Koren and R. L. Maynard, Academic Press, London, 1999, pp. 357–379.
205 J. T. Zelikoff, L. C. Chen, M. D. Cohen, K. Fang, T. Gordon, Y. Li, C. Nadziejko and R. B. Schlesinger, *Inhal. Toxicol.*, 2003, **15**, 131–150.
206 M. Sheehan, *Huffington Post*, 2015.
207 H. T. Kim, C. H. Jung, S. N. Oh and K. W. Lee, *Environ. Eng. Sci.*, 2001, **18**, 125–136.
208 A. Jaworek, W. Balachandran, A. Krupa, J. Kulon and M. Lackowski, *Environ. Sci. Technol.*, 2006, **40**, 6197–6207.
209 C. Carotenuto, F. Di Natale and A. Lancia, *Chem. Eng. J.*, 2010, **165**, 35–45.
210 L. D'Addio, C. Carotenuto, W. Balachandran, A. Lancia and F. Di Natale, *Chem. Eng. Sci.*, 2014, **106**, 222–230.
211 A. Wang, Q. Song and Q. Yao, *Atmos. Environ.*, 2015, **115**, 1–8.
212 A. Wang, Q. Song and Q. Yao, *J. Aerosol Sci.*, 2016, **93**, 1–15.